Electrochemical investigations of redox reactions of uranyl(VI) on magnetite and computational modeling of the UO_2-HfO_2 solid solution

by

Ke Yuan

A dissertation submitted in partial fulfillment
of the requirements for the degree of
Doctor of Philosophy
(Earth and Environmental Sciences)
in the University of Michigan
2015

Doctoral Committee:

Professor Udo Becker, Chair
Professor Joel D. Blum
Professor Mark E. Meyerhoff
Professor David W. Shoesmith, University of Western Ontario
Professor Youxue Zhang

Dedication

To my parents,

Xueqin and Wenping.

Acknowledgements

I would like to thank my advisor Udo Becker, who guides me into this field and provides me the freedom and support to explore every possibility. Thank you for the valuable comments and insightful discussions made by my past and present thesis committee members Joel D. Blum, Rodney C. Ewing, Mark E. Meyerhoff, David W. Shoesmith, and Youxue Zhang.

Thanks for the help from my previous group member Lindsay Shuller on modeling the solid solution, Devon Renock on doing electrochemical experiments, and Jingjie Niu on using the AFM. Thanks for Eugene Ilton from PNNL help on fit the XPS spectra and Mark Antonio from ANL help on electrochemical cell design and on fit the EXAFS data. I appreciate the support from my current group members, starting from my office mate Sandra Taylor who is always ready to answer any questions at any time from me, thoroughly. I thank my first roommate and also our great group member Cameron Lee Tracy who helps me better understand my class materials and research questions through numerous helpful discussions. I thank Ben Gebarski, Sarah Walker, and Zhongrui Li who accompanied me to the Argonne National Lab to complete a series of complicated training and potentially "dangerous" experiments. I enjoy the lunch talks with Evan Killeen and I appreciate the support and encouragement from Will Bender, Krish Arumugam, and Saumitra Saha during our trip to ACS conferences in CA. All the good memories are connected by many presentations during group meetings, discussions in the lab, and lunch talks in front of the dinner table.

I also thank the time and effort Peter J. Cook has devoted in to the sample preparations during the summer time before our trip to Argonne. I thank my Chinese friends Peng Ni, Tao Wen, Yiwei Liu, Xiaofei Pu, Niu Yi and Yu Yi who have organized numerous dinners and activities during the weekends and holidays. Thanks for the support from my parents who share with me their happiness every Friday night during our chat online. I hope the new member YoungJae Kim will have a wonderful time in this group.

Table of Contents

List of Figures

List of Tables

Abstract

Uranium has a unique chemical behavior because of the presence of localized 5f electrons. The redox chemistry of uranium influences its mobility in the aqueous environment. This thesis investigates the redox processes of aqueous uranium (uranyl, $O=U^{6,5+}=O$) in order to understand and predict its behavior in the environment. In addition, the behavior of the UO_2-HfO_2 solid-solution (Hf being a neutron absorber) is modeled to study the conditions under which the mixture forms a solid solution or exsolves, which is essential for its in-reactor performance.

Soluble uranyl(VI) can be reduced on surfaces of Fe(II)-bearing minerals to solid $U(IV)O_2$, resulting in the decrease of its mobility in the environment. However, the previously considered one-step two-electron reduction pathway from U(VI) to U(IV) has been challenged by the presence of stable pentavalent U(V). The experiments here investigate the mechanism of uranium reduction by reducing uranyl(VI) electrochemically on powdered and bulk magnetite electrodes. The number of electrons transferred per redox change is found to be one, which confirms the one-electron reduction from U(VI) to U(V). Nano-size uranium precipitates were found on the surface of magnetite by *in situ* electrochemical AFM. Further spectroscopic evidence (XPS, AES, XANES, and EXAFS) suggests these precipitates are poorly crystallized mixed-valence state U(V) and U(VI) solids, which stabilize U(V) by preventing its disproportionation. In contrast, the catalytic properties of the surface of powdered magnetite facilitates the disproportionation of U(V), which is attributed to the adsorption/desorption kinetics of protons on the particulate magnetite.

In order to better control the power distribution in a nuclear reactor, UO_2, a nuclear fuel material, is mechanically mixed with the neutron absorber HfO_2. The thermodynamic mixing properties of the UO_2-HfO_2 (limited in experimental data) were simulated using DFT and Monte Carlo simulations. The calculated binary forms extensive solid solution at high temperatures across the entire compositional range, with a variety of exsolution phenomena associated with the different HfO_2 polymorphs upon cooling. Close to the UO_2 end member, which is relevant for nuclear fuel fabrication, the isometric uranium-rich solid solutions exsolve as the fuel cools, and there is a tendency to form the monoclinic hafnium-rich phase in the matrix of the isometric, uranium-rich solid solution phase.

Chapter 1 Introduction

Mineral-fluid interfaces serve as active sites for adsorption/desorption, growth/dissolution, redox reactions, and various other geochemical, biological and photochemical processes. These surface reactions influence the mobility of elements, such as toxic heavy metal elements and radionuclides in subsurface environments[1].

The element uranium plays an important role in the nuclear industry[2]. As shown in the diagram of the closed nuclear fuel cycle (Figure 1.1), uranium is mined, processed, and enriched to fabricate nuclear fuel. After burning the fuel in a reactor, the highly radioactive spent nuclear fuel undergoes interim storage to permit the controlled decay of the short-lived radionuclides leading to a decrease in radioactivity. The spent nuclear fuel can be reprocessed to extract fissile elements, such as ^{239}Pu and unburned ^{235}U, to refabricate the nuclear fuel in a closed fuel cycle. For both closed and open fuel cycles (without recovery of ^{239}Pu and ^{235}U from the spent fuel), radioactive waste will eventually be generated from the cycle and will be subjected to long-term storage. Geological disposal has been shown as a promising way for safe storage of the waste in an underground repository[3].

Because of nuclear weapon development in the twentieth century, a significant amount of nuclear waste has been generated[3, 4]. Uranium pollution has become a major issue in the subsurface environment where the uranium was mined and enriched, and where the radioactive waste is stored[2]. The buried waste can leak from the storage containers into nearby aquifers, groundwater and rivers. A substantial number of investigations are concerned with the remediation of the uranium polluted sites[5].

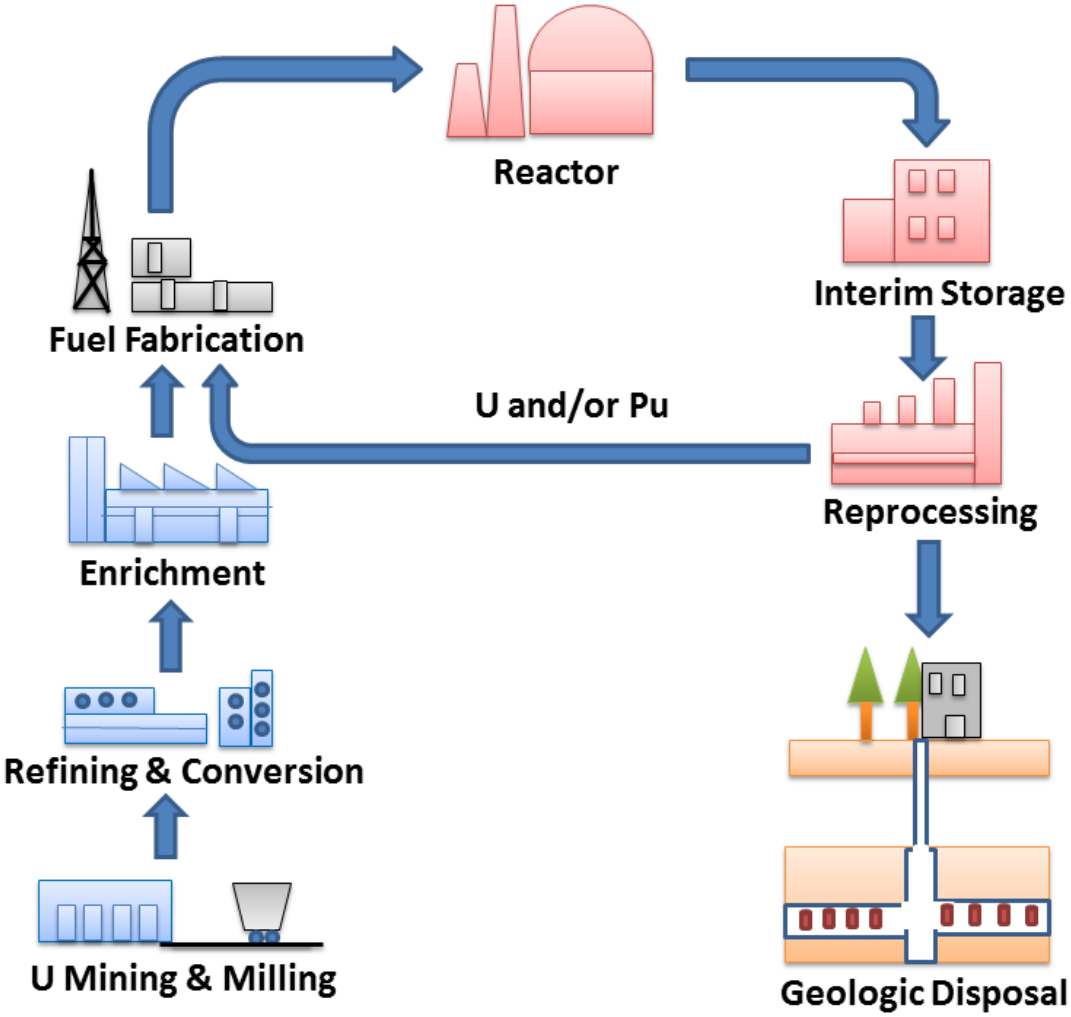

Figure 1.1 The simplified diagram of the closed nuclear fuel cycle[6].

For the commonly used remediation methods, *e.g.*, reactive barrier and bioremediation, the redox chemistry of uranium plays a key role in understanding the mechanisms[1]. There are three important oxidation states of uranium which are 6+, 5+, and 4+. Commonly observed mobile uranium exists in the hexavalent state as a linear molecule, uranyl ($[O=U=O]^{2+}$), and it is subject to complexation with ligands such as H_2O, CO_3^{2-}, SO_4^{2-}, etc. present in the groundwater. Pentavalent uranium also exists in the uranyl structure ($[O=U=O]^{+}$), but knowledge of the environmental behavior of U(V) is limited because of the tendency for U(V) to disproportionate

into U(VI) and U(IV). Tetravalent uranium is found to have a hydration number between 8-9 in acidic pH conditions[6] and forms less soluble phases, such as U(VI) hydroxides and UO_2 solids[7] .

A common remediation technique uses permeable reactive barriers built into the aquifer, where reducing agents remove uranium from the water stream and immobilize it as insoluble uraninite as the groundwater flows through[8, 9]. A second technique uses bioremediation principles where fluids containing certain bacteria are injected to the depth of the contamination. The microbial metabolic processes will then immobilize uranium in the contaminated soils[10-12]. There is, however, another type of method, *in situ* mineralization, which does not require uranium to be reduced. In this case, phosphate-containing fluids are injected into the polluted region and uranium crystallizes as phosphate minerals, which are relatively stable because of their very low solubility[13-16].

In general, for the reductive remediation mechanism, mobile uranium in its hexavalent state needs to be reduced to its tetravalent state by gaining electrons from reducing agents or microbes in order to precipitate out as solids from the groundwater. However, this uranium reduction mechanism is not fully understood. Particularly, increasing evidence in recent studies indicates that U(V) is stable for a certain time spans under specific experimental conditions[17-21].

Historically, electrochemical methods were used to investigate the U(VI) reduction mechanism and U(V) disproportionation kinetics. P. Herasymenko[22] first confirmed the one-electron reduction from U(VI) to U(V) on a mercury electrode in 1928. The studies that followed combined more advanced electrochemical techniques with UV-Vis spectroscopic methods to study U(V) disproportionation reactions, interaction between U(VI) and U(V) (a potential to form U(VI)-U(V) complexes), and redox kinetics of various U(VI) complexes[23-27]. The redox reactions of uranium including the disproportionation of U(V) are summarized in a standard redox potential table in Figure 1.2[28, 29]. However, while all of the above experiments used metallic electrodes, it is well known that the surface properties of the electrode play a significant role in the redox kinetics. Thus, it was a logical research path to borrow the knowledge from electrochemists and simply apply it to an electrode made of mineral materials.

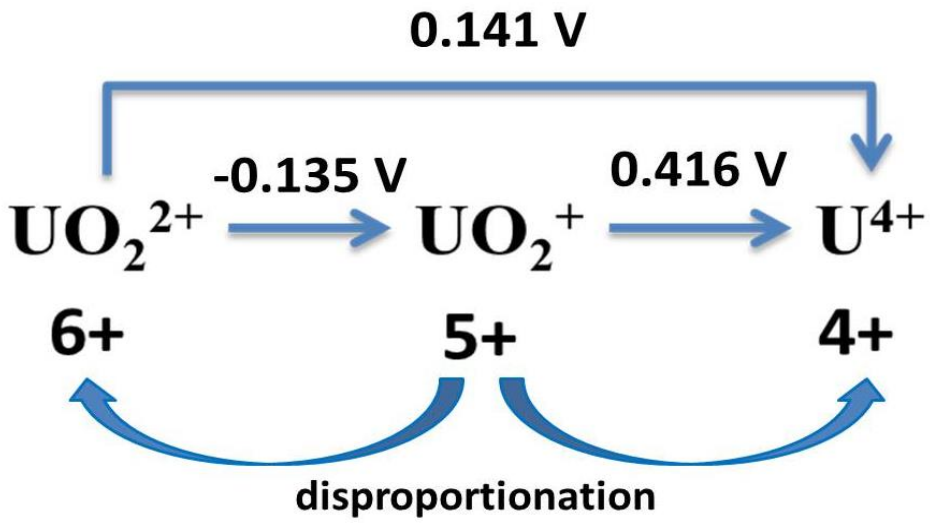

Figure 1.2 Standard redox potential of uranium in 1M $HClO_4$ *vs*. Ag/AgCl (saturated KCl)[21, 22]

Thus, the first research chapter of this thesis focuses on the electrochemistry of U(VI) reduction processes. In order to assign peaks in the voltammograms to specific redox transformation reactions, the concentrations of the reactants and relevant ions from the background electrolyte, and pH were varied to support or refute proposed reactions. An advantage of an electrochemical approach is that the redox potential close to the surface of the mineral electrode can be changed quickly by changing the potential on the electrode, or swept through. In particular, U(VI) redox reactions on both a powder and bulk-crystalline magnetite electrode were investigated and compared.

The second chapter continues the electrochemistry studies on a bulk magnetite electrode due to the simple configurations of this type of electrode. Moreover, a series of *in-situ* and *ex-situ* spectroscopic methods were used to support what was found from the electrochemical experiments. The results from the first two chapters are relevant to the last part of the fuel cycle, which is the geological disposal of the used nuclear fuels. The knowledge of how soluble uranium behaves in groundwater and its interactions with mineral surfaces is important once the containers have corroded (which will eventually occur during long-term disposal). Not just from the geology of the surrounding rock but also from the corrosion of iron, there will be various forms of iron oxide in the near-field environment, such as magnetite.

The third chapter explores another part of the fuel cycle, relevant to the fuel properties in the reactor. The binary containing the nuclear fuel (UO_2) and a neutron absorber (HfO_2) is modeled computationally in order to determine at which temperature the two oxides form a solid solution and where they start to exsolve. The results help us understand the mixing properties of these two components as a function of temperature, which, in turn, influences the thermal conductivity and melting point of the fuel. In addition, the similarity between the UO_2-HfO_2 binary and the UO_2-ZrO_2 binary are discussed.

There are three publications from this thesis work as shown below. The three papers have been revised based on the comments made by the committee members and are the three main research chapters of this thesis. There are two co-authored publications during the study of my PhD program as shown below, as well.

K. Yuan, D. Renock, R.C. Ewing, U. Becker. Uranium reduction on magnetite: Probing for pentavalent uranium using electrochemical methods (2015) *Geochimica et Cosmochimica Acta*. 156 :194-206.

K. Yuan, E.S Ilton, M.R. Antonio, Z. Li, P.J. Cook, U. Becker. Electrochemical and spectroscopic evidence for the one-electron reduction of U(VI) to U(V). *Environmental Science & Technology*. (In press, DOI: 10.1021/acs.est.5b00025)

K. Yuan, R.C. Ewing, U. Becker. Thermodynamic mixing properties of UO_2-HfO_2 solid solution: Density functional theory and Monte Carlo Simulations (2015) *Journal of Nuclear Materials*. 458: 296-303.

D. Renock, M. Mueller, **K. Yuan**, R.C. Ewing, U. Becker (2013) The energetics and kinetics of uranyl reduction on pyrite, hematite, and magnetite surfaces: A powder microelectrode study. *Geochimica et Cosmochimica Acta* 118, 56-71.

S.L. Estes, Y. Arai, U. Becker, S. Fernando, **K. Yuan**, R.C. Ewing, J.M. Zhang, T. Shibata, B.A. Powell (2013) A self-consistent model describing the thermodynamics of Eu(III) adsorption onto hematite. *Geochimica et Cosmochimica Acta* 122, 430-447.

References

1. Ewing, R. C.; Runde, W.; Albrecht-Schmitt, T. E. Environmental impact of the nuclear fuel cycle: Fate of actinides. *MRS Bull*. **2010,** 35, 859-866.

2. International Atomic Energy Agency. Uranium raw material for the nuclear fuel cycle: Exploration, mining, production, supply and demand, economics and environmental issues (IAEA- TECDOC-1739); Vienna, 2009.

3. Ewing, R. C.; The nuclear fuel cycle: A role for mineralogy and geochemistry. *Elements* **2006,** 2, 331-334.

4. Hanford site. http://www.hanford.gov/page.cfm/HanfordCleanup.

5. Multi-Scale Mass Transfer Processes Controlling Natural Attenuation and Engineered Remediation: An IFC Focused on Hanford's 300 Area Uranium Plume. http://www2.lbl.gov/ERSP/field_research/hanford300.html

6. Hennig, C.; Tutschku, J.; Rossberg, A.; Bernhard, G.; Scheinost A.C. Comparative EXAFS investigation of uranium(VI) and -(IV) aquo chloro complexes in solution using a newly developed spectroelectrochemical cell. *Inorg Chem* **2005**, 44, 6655-6661.

7. Neck, V., Kim, J.I. Solubility and hydrolysis of tetravalent actinides. *Radiochimica Acta* **2001, 89**, 1-16.

8. Gu, B.; Liang, L.; Dickey, M. J.; Yin, X.; Dai, S. Reductive precipitation of uranium(VI) by zero-valent iron. *Environ Sci & Technol* **1998,** 32, 3366-3373.

9. Morrison, S. J.; Metzler, D. R.; Carpenter, C. E. Uranium precipitation in a permeable reactive barrier by progressive irreversible dissolution of zerovalent iron. *Environ Sci & Technol* **2001,** 35, 385-390.

10. Istok, J. D.; Senko, J. M.; Krumholz, L. R.; Watson, D.; Bogle, M. A.; Peacock, A.; Chang, Y. J.; White, D. C. In situ bioreduction of technetium and uranium in a nitrate-contaminated aquifer. *Environ Sci & Technol* **2004,** 38, 468-475.

11. Lovley, D. R.; Phillips, E. J. P.; Gorby, Y. A.; Landa, E. R. Microbial reduction of uranium. *Nature* **1991,** 350, 413-416.

12. Wall, J. D.; Krumholz, L. R., Uranium reduction. In Annual Review of Microbiology, 2006; Vol. 60, pp 149-166.

13. Luo, Y.; Hughes, J. M.; Rakovan, J.; Pan, Y. Site preference of U and Th in Cl, F, and Sr apatites. *Am. Mineral*. **2009,** 94, 345-351.

14. Mehta, V. S.; Maillot, F.; Wang, Z.; Catalano, J. G.; Giammar, D. E. Effect of co-solutes on the products and solubility of uranium(VI) precipitated with phosphate. *Chem. Geol*. **2014,** 364, 66-75.

15. Mehta, V. S.; Maillot, F.; Wang, Z.; Catalano, J. G.; Giammar, D. E. Transport of U(VI) through sediments amended with phosphate to induce in situ uranium immobilization. *Water Res.* **2015,** 69, 307-1.

16. Rakovan, J.; Reeder, R. J.; Elzinga, E. J.; Cherniak, D. J.; Tait, C. D.; Morris, D. E. Structural characterization of U(VI) in apatite by X-ray absorption spectroscopy. *Environ Sci & Technol* **2002,** 36, 3114-3117.

17. Renshaw, J. C.; Butchins, L. J. C.; Livens, F. R.; May, I.; Charnock, J. M.; Lloyd, J. R. Bioreduction of uranium: Environmental implications of a pentavalent intermediate. *Environ. Sci. Technol.***2005,** *39*, 5657-5660.

18. Ilton, E. S.; Haiduc, A.; Cahill, C. L.; Felmy, A. R. Mica surfaces stabilize pentavalent uranium. *Inorg. Chem.* **2005,** *44*, 2986-2988.

19. Ilton, E. S.; Boily, J. F.; Buck, E. C.; Skomurski, F. N.; Rosso, K. M.; Cahill, C. L.; Bargar, J. R.; Felmy, A. R. Influence of dynamical conditions on the reduction of U(VI) at the magnetite-solution interface. *Environ. Sci. Technol.* **2010,** *44*, 170-176.

20. Ilton, E. S.; Pacheco, J. S. L.; Bargar, J. R.; Shi, Z.; Liu, J.; Kovarik, L.; Engelhard, M. H.; Felmy, A. R. Reduction of U(VI) Incorporated in the Structure of Hematite. *Environ. Sci. Technol.* **2012,** *46*, 9428-9436.

21. Massey, M. S.; Lezama-Pacheco, J. S.; Jones, M. E.; Ilton, E. S.; Cerrato, J. M.; Bargar, J. R.; Fendorf, S. Competing retention pathways of uranium upon reaction with Fe(II). *Geochim. Cosmochim. Acta*. **2014,** *142*, 166-185

22. Herasymenko, P.; Electroreduction of uranyl salts by means of the mercury dropping cathode. *Trans. Faraday Soc.* **1928,** 24, 0272-0278.

23. Harris, W. E.; Kolthoff, I. M.; The polarography of uranium. 1. Reduction in moderately acid solutions-polarographic determination of uranium. *J. Am. Chem. Soc*. **1945,** 67, 1484-1490.

24. Harris, W. E.; Kolthoff, I. M.; The polarography of uranium. 3. Polargoraphy in very weakly acid, neutral or basic solution. *J. Am. Chem. Soc*. **1947,** 69, 446-451.

25. Kern, D. M. H.; Orlemann, E. F.; The potential of the uranium(V), uranium(VI) couple and the kinetics of uranium(V) disproportionation in perchlorate media. *J. Am. Chem. Soc*. **1949,** 71, 2102-2106.

26. Kolthoff, I. M.; Harris, W. E.; The polarography of uranium. 2. Polarography in strongly acid solution. *J. Am. Chem. Soc*. **1946,** 68, 1175-1179.

27. Newton, T. W.; Baker, F. B.; A Uranium(V)-Uranium(VI) Complex and Its Effect on the Uranium (V) Disproportionation Rate. *Inorg. Chem*. **1965,** 4, 1166-1170.

28. A.J. Bard, R. P., and J. Jordan, Standard Potentials in Aqueous Solutions. Marcel Dekker: New York, 1985.

29. Morris, D. E.; Redox energetics and kinetics of uranyl coordination complexes in aqueous solution. *Inorg. Chem*. **2002,** 41, 3542-3547.

Chapter 2 Uranium reduction on magnetite: Probing for pentavalent uranium using electrochemistry methods

Abstract

Pentavalent uranium is generally treated as an unstable intermediate when the uranyl ion, $U(VI)O_2^{2+}$, is reduced to U^{4+}. However, mineral surfaces have been shown to stabilize pentavalent uranium, thus hindering further reduction (Ilton et al., 2005, 2010). The subject of this study is to identify the kinetic pathways that lead to $U(V)O_2^{+}$ being a metastable species. Electrochemical methods provide an *in situ* approach for the investigation of the intermediate reaction of $U(V)O_2^{+}$ on the surfaces of magnetite. Redox reactions of uranyl ions on particulate (~3 μm) and bulk magnetite surfaces were investigated using cyclic voltammetry and potential step chronoamperometry using cavity microelectrodes and bulk (planar) mineral electrodes. The estimated redox potentials are consistent with the standard redox potential of UO_2^{2+}/UO_2^{+}, indicating UO_2^{2+} is first reduced to UO_2^{+} on the surfaces of both powder and bulk magnetite. The one-electron reduction of UO_2^{2+} to UO_2^{+} was further confirmed by directly measuring the number of electrons transferred during the reduction process on the bulk magnetite electrode. Based on the charge conservation analysis and the positive correlation between the pH and the peak current for the UO_2^{+} transformation to UO_2^{2+}, the peak corresponding to the oxidation of U^{4+} to UO_2^{2+} was assigned in the voltammograms of particulate magnetite. The presence of U^{4+} indicates that the disproportionation of UO_2^{+} ($2\ U(V) \leftrightarrow U(IV) + U(VI)$) is occurring on the surface of particulate magnetite within the timeframe of the experiment. The lack of a peak for U^{4+} in voltammograms for bulk magnetite suggests that the rate of the UO_2^{+} disproportionation reaction is slower on bulk magnetite than that on particulate magnetite. The catalytic property of particulate magnetite surfaces on the disproportionation reaction is explained by its ability to adsorb and desorb protons, which could facilitate the proton-coupled disproportionation reaction of UO_2^{+}. This increased catalytic activity and related adsorption and desorption kinetics of

protons may be related to the increased number of under-coordinated surface sites near step edges on the magnetite powder.

Introduction

Hexavalent uranium exists as the soluble uranyl ion (UO_2^{2+}) in aqueous environments but can be reduced to soluble $U(V)O_2^{+}$ and to relatively insoluble U(IV) species. The change in oxidation state has a significant influence on the solubility of uranium, and therefore, the mobility of uranium in the environment. Magnetite (Fe_3O_4) is a common naturally-occurring iron oxide, and it is also found as a corrosion product of iron under anoxic conditions, such as in zero-valent iron permeable reactive barriers used for the remediation of uranium contaminated ground water and in steel canisters used for the nuclear waste storage (Cornell and Schwertmann, 1996; Gu et al., 1998; Morrison et al., 2001; Dodge et al., 2002; Rovira et al., 2007; Dickinson and Scott, 2010). Numerous studies have identified the retention of uranium through heterogeneous reduction of UO_2^{2+} to U(IV) on the surface of magnetite (e.g., Scott et al., 2005; Gorski and Scherer, 2009; Gorski et al., 2010; Gorski and Scherer, 2010;). Solid U(IV) species formed on magnetite surfaces have been ascribed to the reduction of UO_2^{2+} by transferring electrons from Fe(II) in the magnetite or by other electron donors in solution. In the latter case, the shuttling of electrons between reducing agents and adsorbed UO_2^{2+} is facilitated by the highly conductive surface of magnetite (Becker et al., 2001; Missana et al., 2003; Rosso and Becker, 2003; Renock and Becker, 2010; Gorski et al., 2012; Latta et al., 2012; Singer et al., 2012a; Singer et al., 2012b). The two-electron reduction of UO_2^{2+} to U^{4+} is more energetically favored than the one-electron reduction of UO_2^{2+} to UO_2^{+} based on standard reduction potentials (*i.e.*, $E^0_{U(VI)/U(IV)}$ = 0.070 V, $E^0_{U(VI)/U(V)}$ = −0.135 V, all potentials in this manuscript are with respect to the Ag/AgCl, saturated KCl, 0.197 V *vs.* NHE) (Morris, 2002; Konings et al., 2006). However, direct reduction from UO_2^{2+} to U^{4+} is kinetically hindered due to the significant change between the structures of the reactant and the product, where the UO_2^{2+} exists as the stable linear uranyl molecule with the short U=O bond (Burns, 1999). The more facile pathway to produce U^{4+} is one in which UO_2^{2+} is first reduced to UO_2^{+}, followed by the formation of U^{4+} through the rapid disproportionation of two UO_2^{+} ions (Eq. (1-3)) (Kern and Orlemann, 1949; Steele and Taylor, 2007).

$$2UO_2^{+} + 2H^{+} \rightarrow UO_2^{2+} + U(OH)_2^{2+} \quad (1)$$

$$U(OH)_2^{2+} + H_2O \rightarrow U(OH)_3^{+} + H^{+} \quad (2)$$

$$2UO_2^{+} + H^{+} + H_2O \rightarrow UO_2^{2+} + U(OH)_3^{+} \quad (3)$$

The UO_2^+ disproportionation reaction starts with the formation of a UO_2^+ dimer through cation-cation interactions, followed by a coupled reaction involving both electron transfer and protonation of the axial oxygen of the donor UO_2^+ ion (Eq. (1)) (Steele and Taylor, 2007; Fortier and Hayton, 2010). Eq (2) considers the dominant species of U^{4+} under acidic conditions to be $U(OH)_3^+$ (hydrolysis step) (Neck et al., 2001). The overall reaction is given by Eq (3). The measured rate constant for UO_2^+ disproportionation is 3.4×10^2 $M^{-1}\cdot s^{-1}$ in acidic perchlorate solution (Ekstrom, 1974). Thus, UO_2^+ is generally treated as an unstable intermediate species. However, the presence of stabilized UO_2^+ has been identified in abiotic and biological reduction experiments, in corrosion studies of UO_2, in the mineral wyartite ($CaU^{5+}(UO_2)_2O_4(CO_3)(OH)\cdot 7H_2O$) and in synthetic actinide compounds, suggesting that the UO_2^+ ion is stabilized under specific conditions (Burns and Finch, 1999; Goldik et al., 2004; Sunder et al., 2004; Ilton et al., 2005; Renshaw et al., 2005; Broczkowski et al., 2007; Graves et al., 2008; Graves et al., 2009; Ilton et al., 2010; Heming He, 2012; Ilton et al., 2012; Razdan et al., 2012). Possible reasons for the stabilization of U(V) are sorption to mineral surfaces, incorporation into the mineral structure and formation of a uranate-type coordination environment for UO_2^+, and the slow rate of protonation during the coupled electron transfer-protonation reaction in Eq. (1) (Ilton et al., 2005; Skomurski et al., 2011; Ilton et al., 2012; Wander and Shuford, 2012). The presence of the stabilized pentavalent uranium is of great importance to the fate of uranium in the environment. If uranium can form solid phases in the pentavalent state, this will lead to a new type of remediation pathway that is based on a reduction and precipitation mechanism, thus reducing the mobility of uranium in the environment (Belai et al., 2008).

In previous studies, uranium oxidation states on mineral surfaces were characterized under various environmental conditions using *ex situ* methods, such as X-ray photoelectron spectroscopy (XPS), and *in situ* methods (*e.g.*, X-ray absorption near edge spectroscopy, XANES) (Sturchio et al., 1998; Reeder et al., 2001; Rakovan et al., 2002; Elzinga et al., 2004; Antonio and Soderholm, 2006; Komlos et al., 2008; Luo et al., 2009; Schindler et al., 2009; Ilton and Bagus, 2011; He et al., 2012; Singer et al., 2012a; Wang et al., 2013). While such approaches allow for the determination of the structure and chemical state, it is difficult to control the redox potential during the experiment precisely. The advantage of using

electrochemical methods is that redox conditions close to the electrode-liquid interface can be controlled by the applied potential. Such electrochemical methods have been used to study environmental surface reactions by employing electrodes made of metallic or semiconducting materials (Castro, et al., 1996; Scherer et al., 1997; Nurmi et al., 2005; Nurmi and Tratnyek, 2008; Latta et al., 2012; Renock et al., 2013). The disadvantage of using electrochemical methods is that if there are coupled reactions at the open circuit potential (such as Fe(II) to Fe(III) coupled with U(VI) to U(V) or U(V) to U(IV)), the application of a voltage would disturb the coupled kinetic balance. In electrochemical experiments, the rate of the redox reaction(s) of uranium species can be driven by the applied potential across the electrode-liquid interface. The flow of electrons in and out of the electrode surface is recorded as current and the mechanisms of redox reactions can then be extracted based on the current-potential relationship. Renock et al. (2013) first identified redox peaks of the UO_2^{2+}/UO_2^{+} couple on semiconducting mineral powders. Such electrochemical studies require high conductivity between mineral particles in the packed bed as well as between particles and the underlying working electrode (*i.e.* Pt wire, the current collector). Thus, in this study, the stability and magnitude of the current signal in cyclic voltammograms of the cavity microelectrode was enhanced by mixing a conductivity enhancer, graphite, into the magnetite particles. Moreover, not only voltammograms of the surface of particulate magnetite but also those of bulk magnetite were investigated, in which the known surface area of the bulk mineral electrode allows determination of the number of electrons transferred in the reduction of UO_2^{2+}. Furthermore, the particle size has been shown to control the density of the defect sites on the magnetite surface, and the surface defect density of nano and micro-particulate magnetite is likely to be higher than that of bulk magnetite (Sun et al., 1998; Peng et al., 2008; Petitto et al. 2010). We hypothesize that differences in defect density on the surface of magnetite may lead to different redox mechanisms (kinetic pathways) for the uranium reduction process. The objective of this study is to identify and compare the kinetic pathways for UO_2^{2+} reduction on the surfaces of particulate and bulk magnetite using electrochemical methods. Possible mechanisms regarding the $U(V)O_2^{+}$ being a metastable species will be discussed based on the electrochemical results.

Materials and Methods

Magnetite powder cavity microelectrode

The cavity microelectrode contains a Pt wire, sealed inside a glass tube, which has been etched in *aqua regia* to create the cavity. The diameter of the cylindrical cavity is determined by the diameter of the Pt wire, and the depth of the cavity is controlled by the etching time. The temperature of the *aqua regia* solution is controlled between 70-80 ℃. The electrode was repeatedly checked using optical microscopy every 20-30 min until the desired depth (~30 μm) was obtained. Details on preparing the cavity microelectrode are described elsewhere (Cha et al., 1994; Cachet-Vivier et al., 2001; Athouel et al., 2012; Renock et al., 2013). Magnetite was obtained from Mineville, New York (Ward's Science, USA), and crystals with the lowest number of visible inclusions were selected for energy dispersive X-ray analysis (EDS) using a SEM (Philips XL30). Subsequently, magnetite crystals without evident impurity elements on the EDS spectrum were selected for the experiments. Magnetite powder was obtained by grinding the magnetite crystals using an agate mortar and pestle under atmospheric conditions immediately prior to the experiment. In order to improve the conductivity between magnetite grains, magnetite was mixed with graphite powder (10 wt.%), the latter being ground from a graphite rod used for conductive coating of SEM samples, using mortar and pestle. SiO_2 powder, which is used in the mixed powder containing SiO_2 and graphite for testing the current contribution from graphite, is ground from a SiO_2 crystal in the mortar. Both magnetite and SiO_2 powder had a similar average grain size of 3 μm from SEM image analysis. The experiments found that a few seconds of sonication in deionized (DI) water can remove most of the powder packed inside the cavity. After each experiment, three types of solution were used to clean the electrode, that is, DI water, 0.01M HNO_3, and ethanol. The electrode was sonicated first in DI water to remove the magnetite particles and then in 0.01M HNO_3 solution and then in DI water again to remove nitric acid and finally in ethanol. Each sonication step in respect solutions lasts about 10s. The electrode was then dried in air before packing with new powder.

Bulk magnetite electrode

The magnetite samples from Mineville N.Y. have octahedral parting from which the (111) surface can be obtained. The samples were polished down to the thickness of 1.5 mm using 6 μm, 3 μm and 1 μm diamond sand papers, successively. The polishing work was under atmospheric conditions on dry sand papers, and then the magnetite samples were sonicated in deionized water, acetone and ethanol. Cu wire was then connected to one side of the magnetite crystal using silver paste and sealed in epoxy, such that only one side of the polished surface was exposed to the solution for reaction. The same bulk magnetite electrode was used for all electrochemical experiments. Fresh surfaces were obtained by polishing and cleaning methods described above immediately before the experiment. The geometric area of the magnetite electrode was 0.13 cm^2.

Electrochemistry experiments

A computer-controlled potentiostat (Princeton Applied Research Model 263A using *PowerSuite* software) was used to control the voltage applied to the magnetite working electrode with respect to the Ag/AgCl (saturated KCl) reference electrode, as well as to measure the current that passed between the working electrode and a Pt counter electrode. The working electrode was either the cavity microelectrode (powder magnetite) or the bulk electrode (*i.e.* magnetite (111) surface). Cyclic voltammetry experiments were started from the open circuit potential and scanned first to more positive potentials at a scan rate of 50 mV/s until the switching potential was reached (unless otherwise stated). The potential scan was repeated for 10 to 20 cycles.

The potential step chronoamperometry method provides an approach to directly calculate the number of electrons transferred in the redox reaction. In this method, instead of ramping the potential, the voltage was held at a constant value and the current was measured as a function of time. A voltage of −1.0 V was applied to the bulk magnetite electrode, which is 0.865 V less than the standard redox potential of the UO_2^{2+}/ UO_2^{+} couple (E^0 = −0.135 V). Being significantly below the standard reduction potential minimizes the energy barrier for the electron transfer process, and the reduction kinetics of UO_2^{2+} is mainly controlled by diffusion, that is, the current is determined by how fast the UO_2^{2+} can be transported to the electrode surface through diffusion.

The relationship between the current and the time for such a reaction is described by the Cottrell equation (Bard and Faulkner, 2001):

$$I(t) = \frac{nFAD_0^{1/2}C_0}{\pi^{1/2}t^{1/2}} \quad (4)$$

where I is the current in A, n is the number of electrons transferred per redox change (*i.e.*, if the oxidation state changes by 1, n is 1), F is the Faraday constant 96485.3365 $C \cdot mol^{-1}$, A is the reactive surface area in cm^2, D_0 is the diffusion coefficient of uranyl in sulfate solution (4.0×10^{-6} cm^2/s) (Awakura et al., 1987), C_0 is the initial concentration of UO_2^{2+} ions in $mol \cdot cm^{-3}$ and t is the time in s.

A solution containing 0.1 M ferrocyanide, which was used to test the effectiveness of the cavity microelectrode, was prepared by dissolving $K_4Fe(CN)_6$ (Acros Organics) in deionized water. Uranyl nitrate hexahydrate crystals [$UO_2(NO_3)_2 \cdot 6H_2O$] (International Bio-Analytical Industries, Inc.) were dissolved in the deionized water to prepare the uranyl nitrate stock solution. Uranyl solutions of different concentrations used in experiments were then prepared by adding certain amounts of uranyl nitrate stock solution into 0.1 M Na_2SO_4 (Fisher Scientific) as the background electrolyte. The Fe(II) solution was prepared by dissolving $Fe_2SO_4 \cdot 7H_2O$ (Acros Organics) in deionized water (degassed by Ar). The pH of the solution was adjusted using 0.1 M solutions of either H_2SO_4 or NaOH and measured using the Orion 111A pH meter. All solutions were degassed with Ar for at least 30 min prior to experiments. All voltammograms plot negative current for the cathodic scan and positive current for the anodic scan.

Results and discussion

Testing the cavity microelectrode using the ferro/ferricyanide redox couple

Although cavity microelectrodes have been used for studying the reactivity of a variety of powders, it is possible that direct reactions (*i.e.*, without the involvement of the mineral surface) between the Pt wire, which acts as a current collector at the base of the cavity, and redox-active species in solution can occur (Athouel et al., 2012). In addition, poor conductivity of powder materials can result in low current signal, making it difficult to identify the redox peak from the

background current. By reproducing the reversible one-electron reaction of the $Fe(CN)_6^{4-}$/ $Fe(CN)_6^{3-}$ couple (E^0 = 0.363V *vs.* Ag/AgCl in 0.1M HCl) (Bard and Faulkner, 2001), the effectiveness of the cavity microelectrode was evaluated. Significant enhancement of the current signal was observed by adding 10 wt.% graphite powder into the magnetite. The graphite acts as a conductivity enhancer by decreasing inter-particle resistance. The faradaic currents from the ferro/ferricyanide redox reactions on graphite alone are relatively small as compared with those for magnetite and graphite (Fig. 2.1a). Voltammograms of magnetite and magnetite mixed with graphite powder show higher background current than the other two voltammograms, which is a combination of contributions from charging/discharging the electric double layer and the space charge layer of the semiconducting magnetite. The enhanced peak-current signal (Fig. 2.1a, voltammogram of magnetite + graphite) above the background capacitive current is 2.2 times higher than the sum of the two voltammograms of magnetite and SiO_2 + graphite together (Fig. 2.1a, SiO_2 powder with the similar grain size of the magnetite powder is served as a non-conductive media to replace the volume of magnetite). This result indicates that the graphite itself is not the dominant reactive surface. Instead, graphite provides a highly conductive medium that can conduct electrons first from one grain to another and subsequently to the current collector (Pt wire) efficiently (Fig. 2.1b). The peak separation is a direct indication of the reversibility of a redox reaction. In a reversible redox reaction, the kinetics is controlled by diffusion rather than charge transfer on the metallic electrode or the charge depletion/accumulation in the space charge layer of the semiconducting electrode. In this reversible case, the theoretical peak separation is 59 mV for a single electron transfer process (Bard and Faulkner, 2001). The peak separation on the voltammogram of the ferro/ferricyanide redox couple measured by the cavity microelectrode loaded with mixed magnetite and graphite powder (Fig. 2.1a, voltammogram of magnetite + graphite) increases from 68 mV in the first scan cycle to 161 mV in the 20^{th} cycle. The peak separation is 115 mV on the metallic Pt electrode (Fig. 2.1a, empty cavity), indicating that magnetite has a minor influence on the reversibility of the redox behavior. The reason for the increased peak separation with the number of the scan cycles on the voltammogram of magnetite + graphite is still not clear. By measuring the peak current value in the last scan cycle, the surface area of the mixed magnetite with graphite powder inside the cavity was estimated to be 3600 μm^2 according to the equation for the reversible one-electron redox couple between ferro/ferricyanide as compared with the geometric

area of the top surface of the Pt wire, which is only 1963 μm^2 as calculated from the cavity diameter (Bard and Faulkner, 2001). Similar tests in uranium solution were done (see section 3.2), and the conductivity between magnetite grains was also improved by adding graphite powder.

The I-E reproducibility of the cavity microelectrode was assessed by measuring the voltammogram of ferro/ferricyanide on magnetite + graphite for 10 freshly prepared electrodes. The uncertainty of the peak current value was found to be ± 0.02 μA (for absolute peak heights typically ranging from 0.5 to 1.0 μA). Details regarding the reproducibility tests are described in the appendix.

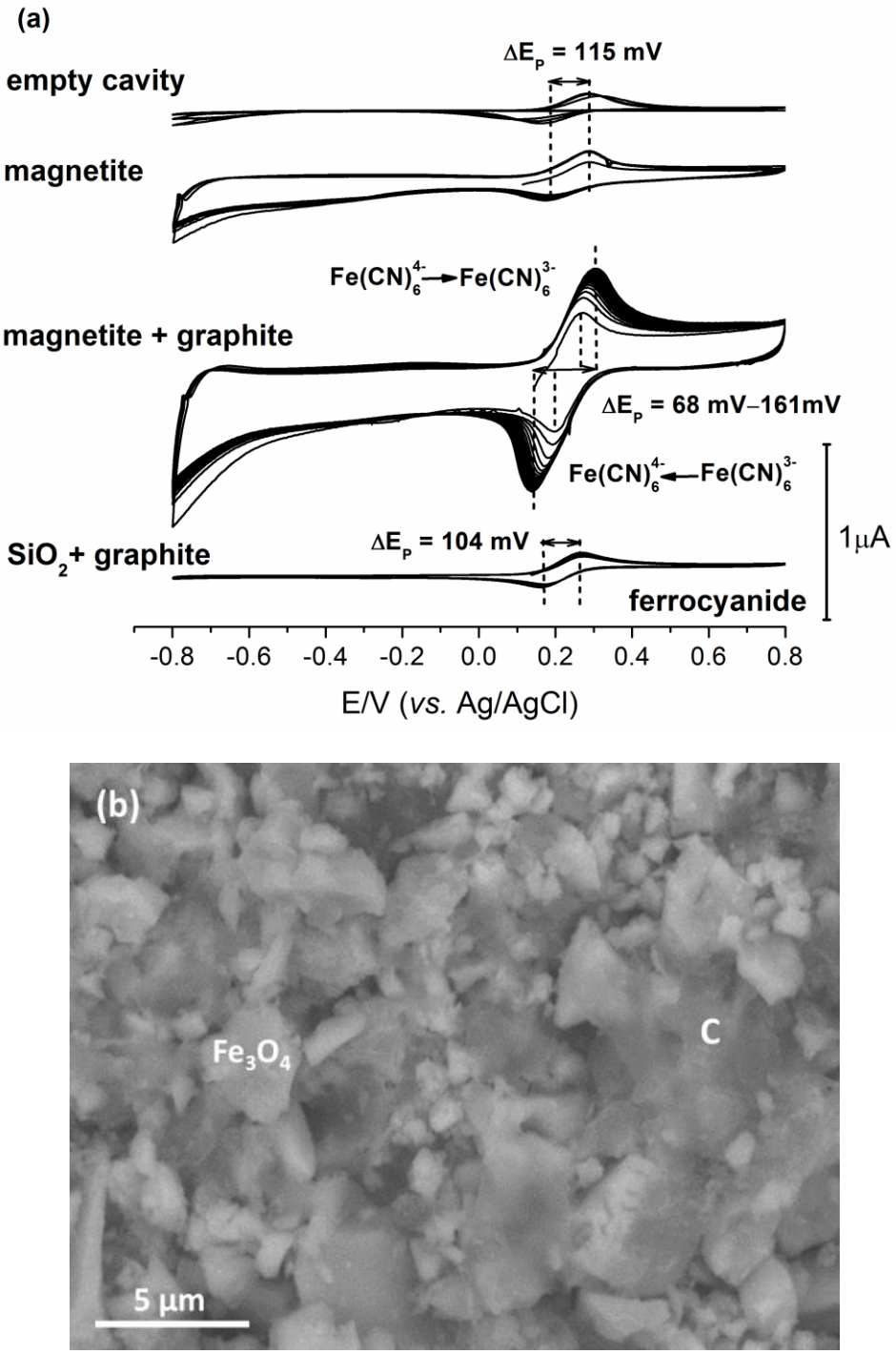

Figure 2.1. (a) Cyclic voltammograms of the empty cavity, magnetite powder, magnetite powder mixed with 10 wt.% graphite, and the SiO_2 powder mixed with 10 wt.% graphite using the cavity microelectrode (freshly-packed) in 0.01M ferrocyanide solution. Scan rate is 50 mV/s and repeated for 20 cycles. (b) Backscattered electron image of the magnetite powder mixed with 10 wt.% graphite. Light granular particles are magnetite and dark flakes are graphite.

Redox reactions of the magnetite powder in background electrolyte

Cyclic voltammograms of cavity microelectrodes in 0.1 M Na_2SO_4 solution exhibit the highest current signal in the electrode packed with mixed magnetite and graphite powder (Fig. 2.2a, magnetite + graphite). The current measured during cyclic voltammetry of semiconducting materials results from the capacitive currents (*i.e.*, currents resulting from charging/discharging of the electric double layer and space charge layer of magnetite) and from redox reactions on the electrode surface (*i.e.*, faradaic currents). Faradaic currents include reactions of the electrode material and reactions between the electrode and dissolved species in the electrolyte (Wu et al., 2003). White et al. (1994) assigned the two half-cell reactions on magnetite to the cathodic dissolution of magnetite (Eq. (5)) and the oxidation of magnetite to maghemite (Eq. (6)), respectively.

cathodic: $$[Fe^{2+}Fe_2^{3+}]O_4(\text{magnetite}) + 8H^+ + 2e^- \rightarrow 3Fe^{2+} + 4H_2O \quad (5)$$

anodic: $$3[Fe^{2+}Fe_2^{3+}]O_4(\text{magnetite}) \rightarrow 4[Fe_2^{3+}]O_3(\text{maghemite}) + Fe^{2+} + 2e^- \quad (6)$$

The cathodic current (*i.e.*, currents associated with the cathodic dissolution of magnetite) increase continuously when the potential is scanned negatively (*i.e.*, cathodic), which is in contrast to the relatively flat anodic current curve (Fig. 2.2a, magnetite + graphite). The flat anodic current is attributed to the formation of maghemite, a relatively unreactive passivation layer that prevents further oxidation of the surface (White et al., 1994). In addition, we found new voltammetric peaks in the present study.

Magnetite cyclic voltammetry shows two coupled redox peaks (identified as C1/A1 and C2/A2 in Fig. 2.2a) on top of the background current, which becomes more pronounced when the pH of the solution is lowered (Fig. 2.2b). Cyclic voltammograms using the graphite powder and the empty cavity microelectrode were also collected, and the absence of these two redox peaks (C1/A1 and C2/A2) on graphite and Pt indicates the redox reactions were specific to magnetite (Fig. 2.2a, SiO_2 + graphite and empty cavity). For the C1/A1 couple, the anodic peak current A1 is 3.8 times higher than that of C1, indicating differences in the kinetics of the reduction and the oxidation process as well as the irreversibility of the reaction due to a non-Nernstian peak separation of 226 mV. In order to find the redox couple corresponding to the C1/A1 peaks, a series of voltammograms were collected in solutions with different

concentrations of Fe^{2+} and SO_4^{2-}. Peak currents for the C1/A1 couple increase with an increase in free Fe^{2+} concentration (Fig. 2.2a, inserted graph), but not SO_4^{2-} (data not shown), suggesting that the C1/A1 couple is related to the redox reaction of the free Fe^{2+}/Fe^{3+} in the solution on the surface of magnetite. Although the midpoint potential ($E_{1/2} = (E_{A1}+E_{C1})/2$) can be distorted by irreversible peak behavior, it is used as a first approximation for the formal redox potential of the C1/A1 couple. The midpoint potential of the C1/A1 couple is approximately 0.31 V (Eq. (5)). This formal potential does not represent the equilibrium potential of a magnetite surface, but is specific for the redox reaction of free Fe^{2+} from solution on a magnetite surface. To our knowledge, this midpoint potential does not match exactly with known redox reactions of free ions of Fe^{2+}/Fe^{3+} (0.574V *vs.* Ag/AgCl). Fe^{2+} can be released into solution from the magnetite electrode during the cathodic scan and then oxidized back to Fe^{3+} corresponding to the peak A1. The peak current of the C1/A1 redox couple decreases with increasing the pH of the solution, and the peak position of A1 shifts to the left from 0.41 V to 0.35 V when the pH is increased from 3.44 to 4.50 (Fig. 2.2b). This obeys the pH-dependent Nernst relation ($E = E^0 - 0.0592$ pH, at 25 ℃) (Bard and Faulkner, 2001), indicating a proton-coupled redox reaction. With the consideration of the acidic pH condition that constrains the dominant Fe^{3+} species to be $Fe(OH)^{2+}$ (based on speciation calculations by *Visual MINTEQ*), the proposed reaction for the C1/A1 redox couple can be written as:

$$Fe(OH)^{2+} + H^+ + e^- \leftrightarrow Fe^{2+} + H_2O \qquad E_{1/2}\,(C1/A1) = 0.31\ V\ vs.\ Ag/AgCl \quad (7)$$

The redox couple C2/A2 exhibits peaks separated by 83 mV from each other, suggesting close to reversible behavior. The peak current decreases with the increase of the solution pH and is independent of the concentration changes of Fe^{2+} and SO_4^{2-} in solution; thus, it was assigned to H^+ adsorption/desorption reactions as:

$$OH \equiv \text{magnetite} + H^+ + e^- \leftrightarrow H_2O \equiv \text{magnetite} \quad E_{1/2}(C2/A2) = -0.20\ V\ vs.\ Ag/AgCl \quad (8)$$

which has also been identified on voltammograms of other conductive oxides, such as IrO_2 and SnO_2 (Locatelli et al., 2011).

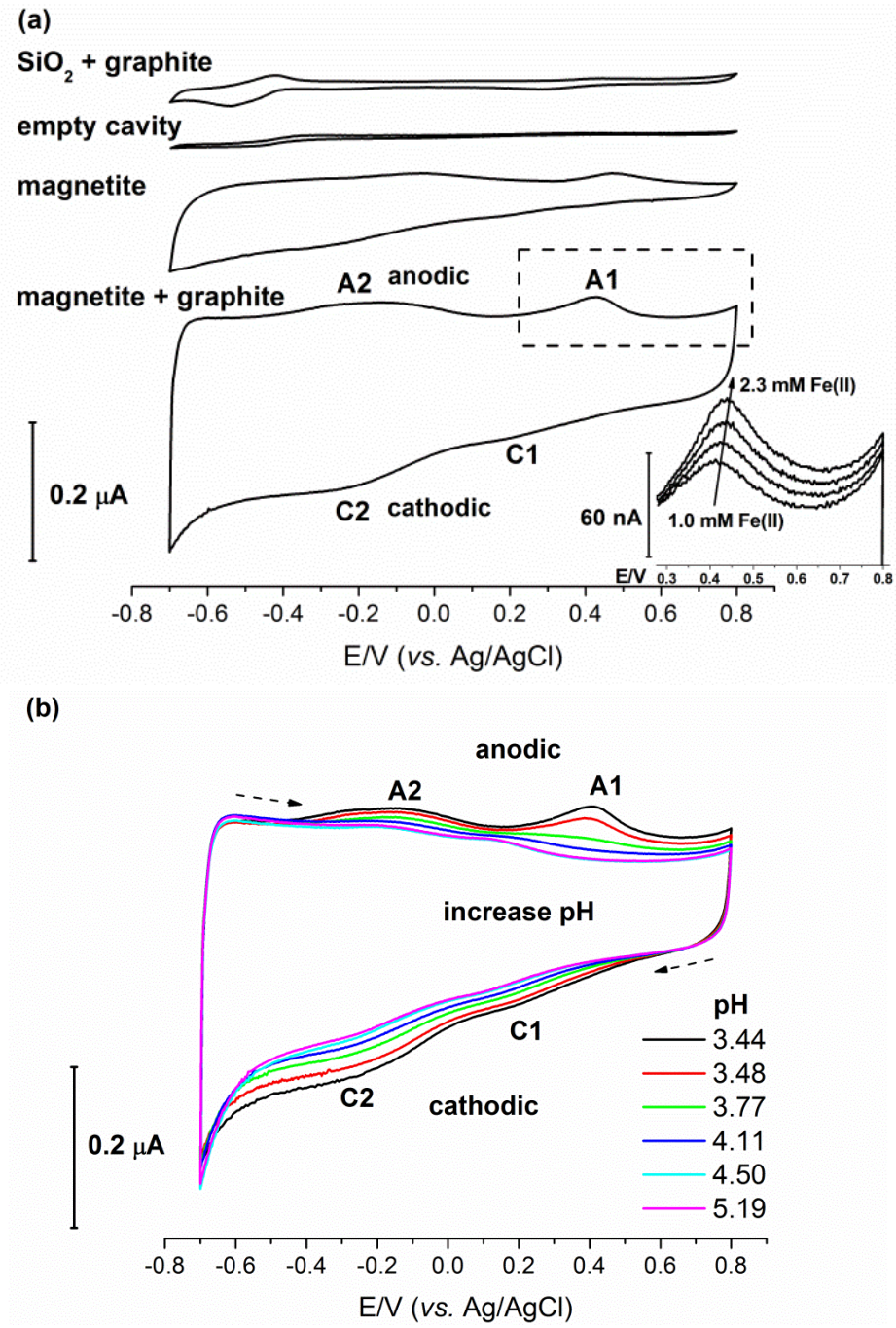

Figure 2.2. (a) Cyclic voltammograms of the newly-packed cavity microelectrode loaded with SiO_2 mixed with 10 wt.% graphite, empty cavity, magnetite powder and magnetite powder mixed with 10 wt.% graphite, respectively, in a 0.1 M Na_2SO_4 solution of pH = 3.4. (b) Voltammograms (measured on the same electrode) of the magnetite + graphite electrode scanned in 0.1 M Na_2SO_4 solution in a pH range from 3.44 to 5.19. The inserted voltammogram in (a) shows the square region of the peak A1, where the peak current increased as the Fe(II) concentration increased from 1.0 mM to 2.3 mM. Dashed arrows in (b) show the scan direction.

The scan rate is 50 mV/s and repeated from 15 cycles. The voltammograms of the last cycle in each measurement are showed above.

Double anodic peaks and the UO_2^+ disproportionation on magnetite powder

Additional currents appear (see C3/A3 in Fig. 2.3a) when uranium is added to the background electrolyte. Current in C3 shows the flat current feature instead of a peak current. This may cause by its microelectrode property, that is, not all the powder in the cavity is conducting electrons but they are separated into individual grains which are similar to a microarray electrode. The peak current of C3 and A3 (i_{pC3}, i_{pA3}) both show a positive linear correlation with the UO_2^{2+} concentration (Fig. 2.3b), indicating that the C3/A3 couple is related to UO_2^{2+} redox reactions on magnetite. The cathodic and anodic peak current on the voltammogram of magnetite in the ferrocyanide solution (Fig. 2.1a, magnetite) have similar absolute values with a peak separation of 115 mV, indicative of a quasi-reversible one-electron reaction. In contrast, the anodic peak current i_{pa3} (A3) in the UO_2^{2+} solution (Fig. 2.3a, b) is more than two times higher than the cathodic i_{pc3} (C3) and the peak separation is as large as 176 mV. The large differences between the shape of the cathodic and anodic peaks observed in the UO_2^{2+} solution can be caused either by significant differences in the kinetics between the reduction and the oxidation half reactions of the uranyl or can be the result of coupled homogeneous reactions (*e.g.*, UO_2^+ disproportionation). The calculated midpoint potential (–0.085 V) of the C3/A3 peak on the powder magnetite is close to the redox potential of UO_2^{2+}/UO_2^+ ($E_{U(VI)/U(V)}$ = –0.135 V, 0.05 V in difference) in comparison with 0.070 V for the UO_2^{2+}/U^{4+} redox couple (0.155 V in difference). In addition to the primary peak C3/A3 caused by the UO_2^{2+}/UO_2^+ couple, the peak A4 at 0.438 V also increases with increasing the UO_2^{2+} concentration. A similar peak (A4) at 0.45 V was identified on the cyclic voltammogram of hematite powder in the UO_2^{2+} solution (Renock et al., 2013). In order to find redox reactions corresponding to the peak A4, the charge transferred under the cathodic and anodic peaks on the voltammograms in Fig. 2.3a was calculated based on Eq. (9):

$$\boldsymbol{Q = \int_{E1}^{E2} \frac{I}{v}\, dE} \qquad (9)$$

Q is the charge in coulombs (C), *E1* and *E2* are the two potentials, which define the scan range in V, *I* is the current in A and *v* is the scan rate in V/s. All integrated charges of the cathodic (C3) and anodic (A3 + A4) half cycle on voltammograms in Fig. 2.3a had similar values (Fig. 2.3c) as a function of the UO_2^{2+} concentration. The similar amount of charge transferred in the single cathodic peak and double anodic peaks obeys the conservation of charge, indicating the conservation of the amount of uranium species reduced and oxidized in a complete redox cycle. Therefore, the increasing current at A4 has to be part of the uranyl redox reaction and is most likely caused by the oxidation of the disproportionation product U^{4+} (Eq. (1)) back to UO_2^{2+} (the pH dependent study in the next section also proves that the disproportionation reaction occurred during the experiment). If the reduced UO_2^{+} was stable in solution, it would be oxidized back to UO_2^{2+} in the reverse anodic scan, and the charge flow under the primary redox peaks (C3/A3) would have a similar value and no additional peak (A4) would be found in the voltammogram. However, the UO_2^{+} generated in the reduction step is not stable, and part of the UO_2^{+} disproportionate into UO_2^{2+} and U^{4+} (Eq. (1)). The extra UO_2^{2+} flux would be generated continuously towards the electrode surface through UO_2^{+} disproportionation, which may also explain the steady-state cathodic current observed in C3 (Fig. 2.3a). Note, U^{4+} is not oxidized to UO_2^{+} first and then to UO_2^{2+}, because if it was, a two-step oxidation reaction ($U^{4+} \rightarrow UO_2^{+} \rightarrow UO_2^{2+}$) resulting in two anodic peaks of similar peak current would be observed instead of the single peak (A4, $U^{4+} \rightarrow UO_2^{2+}$) found here.

Particularly, the position of peak A4 (U^{4+}/UO_2^{2+}) is very close to the potential of the peak A1, which was previously assigned to the oxidation of Fe^{2+} to Fe^{3+}, and the reason for such a similar peak position is still not clear. Experimental studies have found close redox potentials between the Fe(II)/Fe(III)-containing (hydr)oxides and the U(VI)/U(IV) redox couples under common groundwater conditions (Ginder-Vogel, et al, 2006). In addition, similar peak positions on the voltammogram also indicate that the two species (U^{4+} and Fe^{2+}) require a similar potential to extract electrons from their highest occupied molecular orbital (HOMO) to the conduction band of magnetite in order to be oxidized. Thus, it is possible that U^{4+} and Fe^{2+} species have very similar U 5*f* and Fe 3*d* energy levels, resulting in the same peak potential on the voltammograms. It is also possible that the oxidation of Fe(II) and U(IV) are coupled redox reactions resulting in similar peak positions.

Current contributions from the UO_2^{2+} redox reactions on graphite powder, Pt wire electrode, magnetite powder and the powder containing magnetite mixed with graphite were analyzed (Fig. 2.3d). Adding graphite into the magnetite powder enhanced the current signal from redox reactions with uranium (Fig. 2.3d, magnetite + graphite). In particular, the voltammogram of the graphite powder (Fig. 2.3d, SiO_2 + graphite) has a similar peak pattern as compared with the voltammogram of magnetite + graphite (primary redox peaks (C3/A3) and the side peak (A4)), indicating that the UO_2^{+} can also disproportionate on the graphite powder. However, the current from graphite alone is 4.5 times lower for the primary redox peaks (A3) and is 2.5 times lower for the side peak (A4) as compared to the current on the voltammogram of magnetite + graphite, indicating that the current contribution from UO_2^{2+} redox reactions is mainly from the reaction on magnetite.

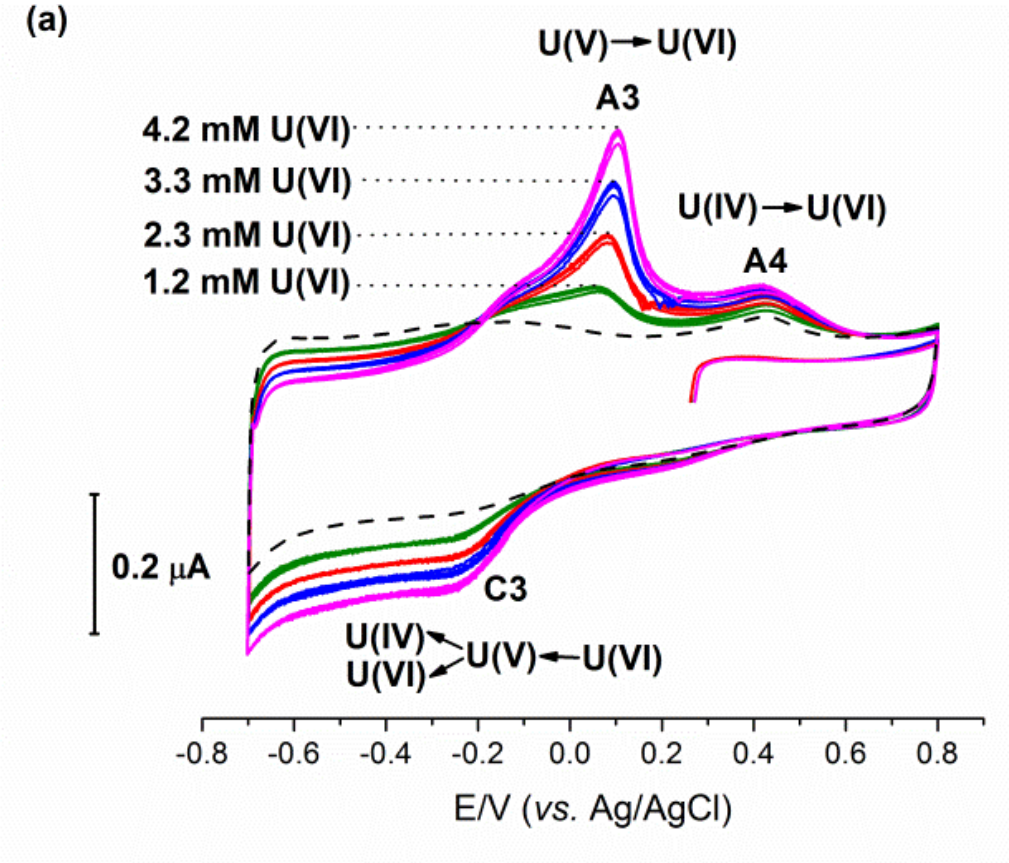

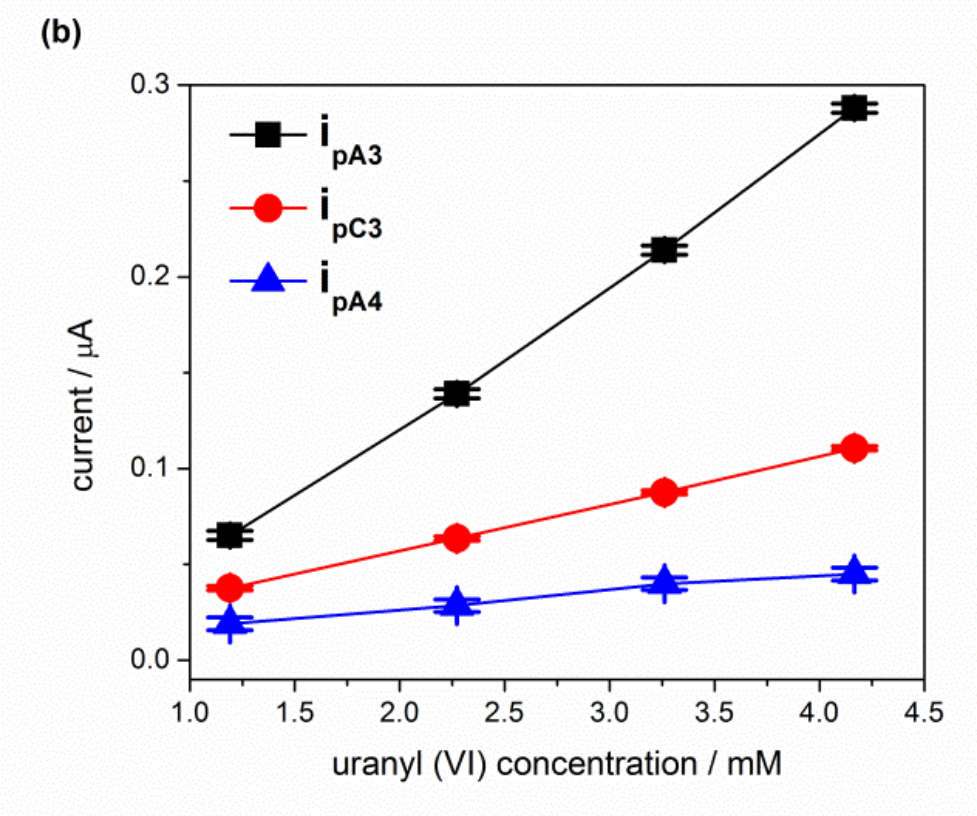
(b)
0.3
0.2
0.1
0.0
current / μA
i pA3
i pC3
i pA4
1.0
1.5
2.0
2.5
3.0
3.5
4.0
4.5
uranyl (VI) concentration / mM

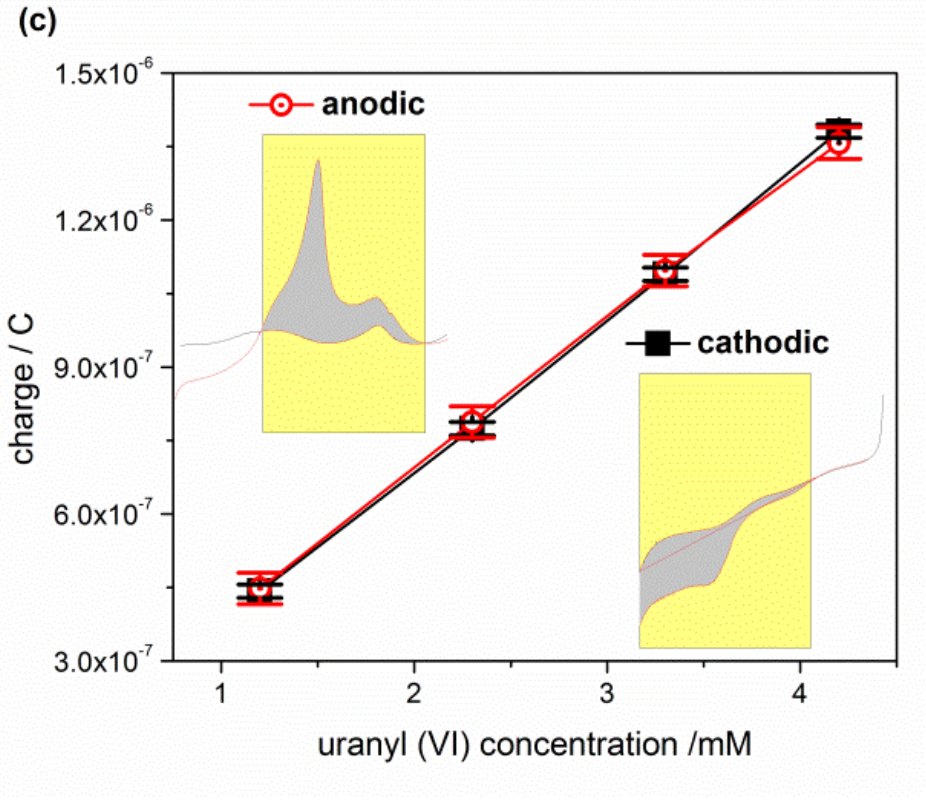
(c)
1.5x10-6
1.2x10-6
9.0x10-7
6.0x10-7
3.0x10-7
charge / C
anodic
cathodic
1
2
3
4
uranyl (VI) concentration /mM

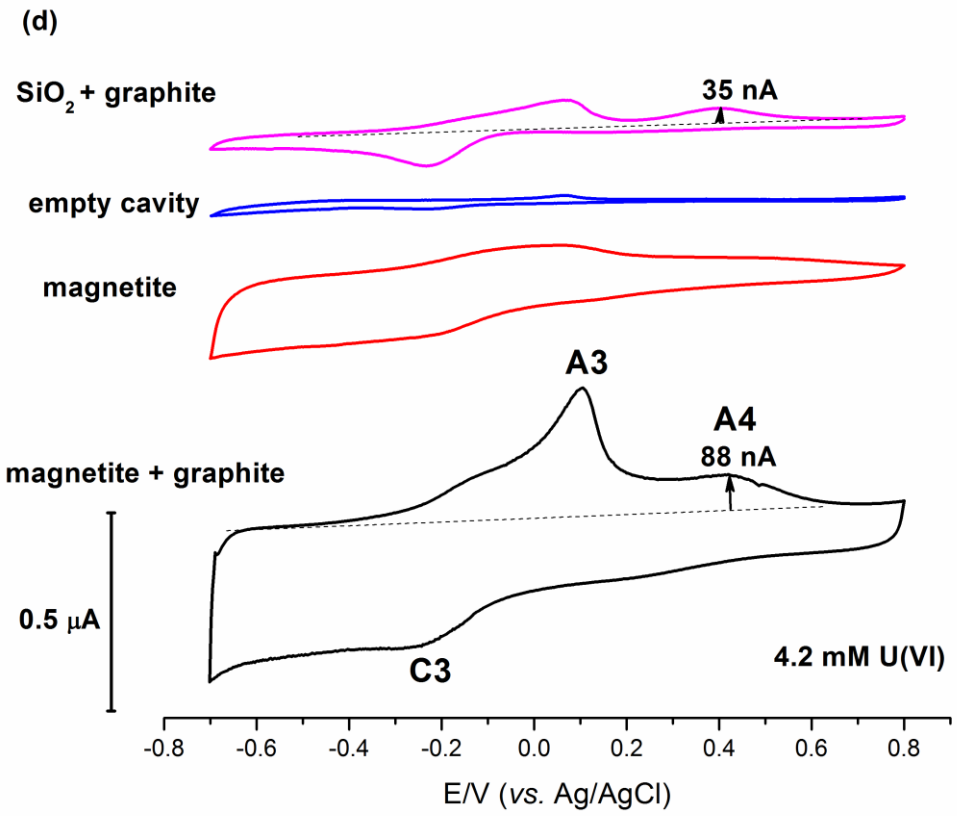

Figure 2.3. (a) Cyclic voltammograms of the cavity microelectrode loaded with the mixed powder containing magnetite and 10 wt.% graphite in UO_2^{2+} solutions of concentrations from 1.2 mM to 4.2 Mm. All the 10 cycles of voltammograms in each of the four solutions with different UO_2^{2+} concentration were showed, and different cycles in each concentration all overlapped with each other. (b) Linear relationship between the peak current and the UO_2^{2+} concentration. (c) Cathodic and anodic charge plot as a function of UO_2^{2+} concentration showed liner relationship and inserted graphs showed an example of charge integration in the 4.2 mM UO_2^{2+} solution. Peak current values (b) and integrated charges (c) were all referred to the voltammogram in 0.1M Na_2SO_4 as background current (Fig. 2.3.a, dashed line). The pH of the solution is 3.3 with the scan rate of 50 mV/s and 10 scan cycles each measurement. Error bars represent the standard deviation calculated from the data in 10 cycles. (d) Cyclic voltammograms of the cavity microelectrode loaded with SiO_2 mixed with 10 wt.% graphite, empty cavity, magnetite powder and magnetite powder mixed with 10 wt.% graphite, respectively, in a 4.2 mM UO_2^{2+} solution of pH = 3.3. The scans were repeated from 15 cycles on freshly-packed electrodes and only the voltammograms of the last cycle in each measurement are showed.

Proton-facilitated UO_2^+ disproportionation

The reduction of UO_2^{2+} to UO_2^+ and the subsequent UO_2^+ disproportionation on the magnetite powder can also be confirmed by studying the anodic half reaction in solutions of different pH. The voltammetric peak A3 exhibited two different trends when the pH was increased. In the first trend, the height of the peak A3 (Fig. 2.4a) ascribed to the oxidation of UO_2^+ to UO_2^{2+} increased when pH was increased from 3.36 to 3.88 (Fig. 2.4a, process 1). Since the UO_2^+ disproportionation involves H^+ (Eq. (1)), decreasing the H^+ concentration by increasing pH suppresses the consumption rate of UO_2^+ through disproportionation, such that more UO_2^+ would be saved in the reverse anodic scan, which explains the increasing peak current of A3 (Fig. 2.4a, process 1, A3 is due to UO_2^+ to UO_2^{2+}) with the increase of pH. This current-pH relationship verifies that the redox reactions of C3/A3 were not the two-electron reaction between the UO_2^{2+}/U^{4+} couple. If the cathodic peak C3 resulted from the reduction of UO_2^{2+} to U^{4+}, then the anodic peak A3 would be caused by the oxidation of U^{4+} to UO_2^{2+}. Decreasing the H^+ concentration by increasing the pH, less U^{4+} is generated during the reduction because this reaction involves the participation of H^+ (Eq. (10)). Therefore, a decrease in the A3 peak current, which would be caused by oxidation of U^{4+} to UO_2^{2+}, instead of the observed increase, would be found in the voltammogram.

$$UO_2^{2+} + 4H^+ + 2e^- \leftrightarrow U^{4+} + 2H_2O \quad (10)$$

With the continued increase of the pH from 4.40 to 4.81, the peak height of A3 starts to decrease quickly (Fig. 2.4a, process 2). The increase in pH from 4.40 to 4.81 influences the concentration of the dominant species, $UO_2SO_{4(aq)}$ in solution according to thermodynamic calculations using the *Visual MINTEQ* software, where the total amount of soluble uranium species starts to decrease at pH 4.0 (Fig. 2.4b). Thus, the decrease in the amount of the redox-active species is likely to occur in process 2 shown in Fig. 2.4a, which results in the decrease of peak current A3. In addition, peak A4 decreases continuously with the increase of pH, which is due to the decrease of the amount of U^{4+} generated by disproportionation at higher pH. This is consistent with the previous assignment of peak A4 to the oxdidation of U^{4+} to UO_2^{2+}.

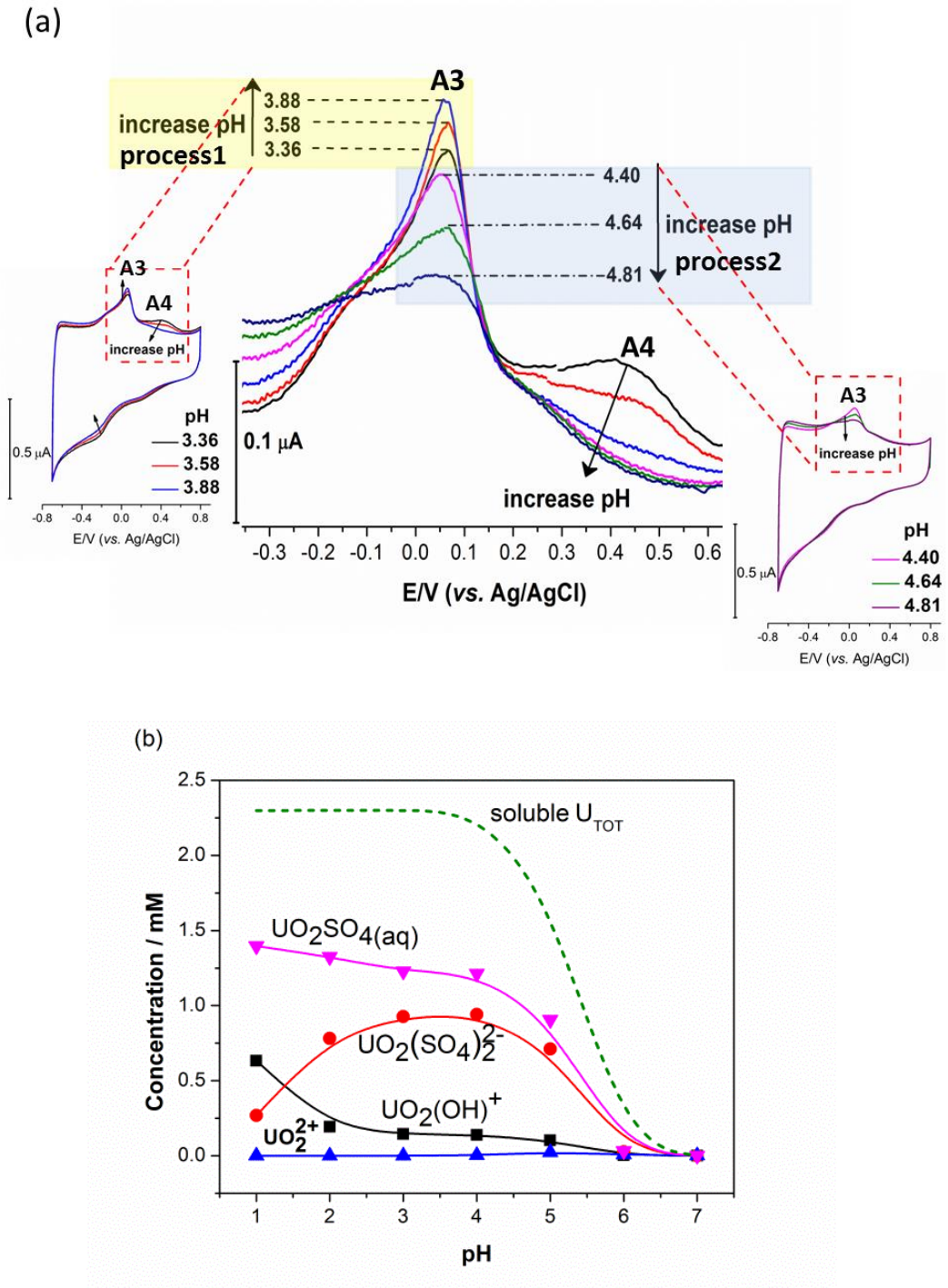

Figure 2.4. (a) Cyclic voltammograms of uranyl redox reactions at different pH from 3.36 to 4.81 using a cavity microelectrode loaded with magnetite mixed with 10 wt.% graphite. Arrows point to the direction where pH was increasing. The UO_2^{2+} concentration is 2.3 mM, and the background solution is 0.1M Na_2SO_4. The scan rate is 50 mV/s. (b) The concentration of aqueous uranium species changed as a function of pH, obtained by *Visual MINTEQ*. The dashed line represents the total amount of soluble uranium species in the solution.

Stabilized UO_2^+ on the surface of the bulk magnetite electrode

On the bulk magnetite electrode, cathodic and anodic peaks related to uranyl redox reactions have a more similar peak shape and similar peak current heights when compared to voltammograms of the magnetite powder. The shape of the voltammogram on the bulk magnetite electrode gradually stabilized with increasing the number of scan cycles (Fig. 2.5a), which was not observed on the voltammogram of the powder magnetite (Fig. 2.3a). The cathodic charge density dropped quickly in the first two cycles and approached the stable state in the following scan. On the contrary, the anodic charge density increased with scan cycle and gradually approached the charge density of the cathodic scan (Fig. 2.5b). Thus, the ratio of the cathodic and the anodic charge decreased from 2.8 to 1.2 within 12 cycles (Fig. 2.5b, inserted graph). Comparing with the cathodic current in the background solution (Fig. 2.5a, dashed line), the tail of the cathodic current density of the last cycle in UO_2^{2+} solution was about 2.1 $\mu A/cm^2$ less than the current density in the background solution. This is likely due to a decrease in reactive surface area, which may be caused by adsorption of uranium species to the surface of the electrode.

The reason for the faster disproportionation of UO_2^+ on the powder magnetite (presence of the side peak A4 caused by the U^{4+} oxidation) than that on the bulk magnetite electrode (absence of the side peak A4) is still not clear. However, when the bulk electrode was applied at a constant potential of –0.6 V for 5 min before the cyclic scan, the first cycle of the voltammogram showed a broad oxidation peak. The new weak peak at 0.17 V was identified only in the first cycle (Fig. 2.5c. new peak indicated by the arrow), suggesting a long period of polarization before the scan generated other species, which is very likely to be related to U^{4+}. The voltammogram in the second cycle returned back to the baseline current, similar to the redox reaction of UO_2^{2+}/ UO_2^+ found in Fig. 2.5a. Therefore, it is very likely that the UO_2^+ disproportionation reaction can also occur on the bulk magnetite electrode, but at a much slower rate than on the surface of the powder magnetite.

The inner-sphere UO_2^+ disproportionation mechanism has been proposed by Steele and Taylor (2007) by first forming the UO_2^+ dimer through cation-cation interactions, that is, the oxo-O from one of the O=U(V)=O needs to bond with the uranium atom from another UO_2^+ in order to form the "T" shape configuration, which is then followed by proton-coupled electron transfer at the donor UO_2^+ ion (Nocton et al., 2008; Fortier and Hayton, 2010; Mougel et al., 2010). Thus,

the fast disproportionation rate found on the powder magnetite surface could result from the powder surface being able to either promote the U(V) dimer formation or facilitate the electron transfer from the donor UO_2^+ to the acceptor UO_2^+. Bulk and powder magnetite have different surface structures, resulting in different defect densities. Petitto et al. (2010) identified two types of oxygen-terminated bulk magnetite (111) surfaces under hydrated conditions in neutral pH. Protonation of the surface O atoms is expected and the redox-active Fe^{2+}/Fe^{3+} cations were under the hydrated surface layers. Surfaces of the magnetite particles have a higher density of Fe and O defect sites compared to the bulk magnetite surface. Numerous studies, especially studies on magnetite nanoparticles, have showed increased catalytic properties with decrease in grain size (Sun et al., 1998, Peng et al., 2008). One notable difference between the powder and bulk magnetite electrode is that the surface of powder magnetite shows higher reactivity, indicated by the protonation/deprotonation reaction (Fig. 2.2a, peak C2/A2) in the background solution, as compared to the relatively smooth voltammogram of the bulk magnetite electrode in the same electrolyte (Fig. 2.5a, dashed line). The UO_2^+ disproportionation is a proton-coupled electron transfer reaction. Thus, it is possible that the active protonation/deprotonation sites on the surface of the powder magnetite provide the area with higher surface coverage of sorbed protons compare to the bulk surface, which facilities the UO_2^+ disproportionation (Fig. 2.5d).

In addition, because of the amount of powder (~ μg) that can be loaded to the powder microelectrode is constrained by the size of the cavity, the surface area of the bulk electrode (1.3×10^7 μm^2) is larger than that of the powder microelectrode (~ 4.0×10^3 μm^2). The difference in surface area results in the greater currents observed in the voltammograms of the bulk magnetite electrode. Thus, more UO_2^+ can be generated in the reduction (cathodic scan) by using the bulk magnetite electrode. Although, the rate of the UO_2^+ disproportionation should increase with increasing its concentration, it is possible that if a solubility limit is reached for a U(V)-containing phase, then the UO_2^+ disproportionation will be inhibited. However, the exact mechanism of how the surface of the magnetite powder facilitates UO_2^+ disproportionation and whether there is a formation of stable U(V)-containing phase on the bulk magnetite still need further investigations.

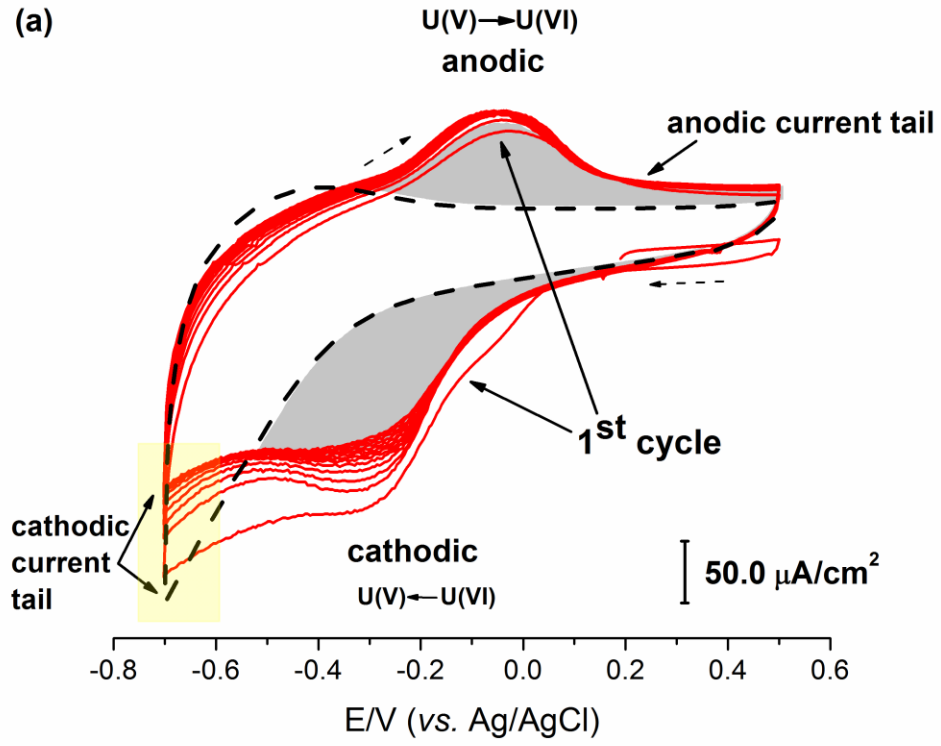
(a)
U(V)→U(VI)
anodic
anodic current tail
1st cycle
cathodic
current
tail
cathodic
U(V)←U(VI)
50.0 μA/cm2
-0.8
-0.6
-0.4
-0.2
0.0
0.2
0.4
0.6
E/V (vs. Ag/AgCl)

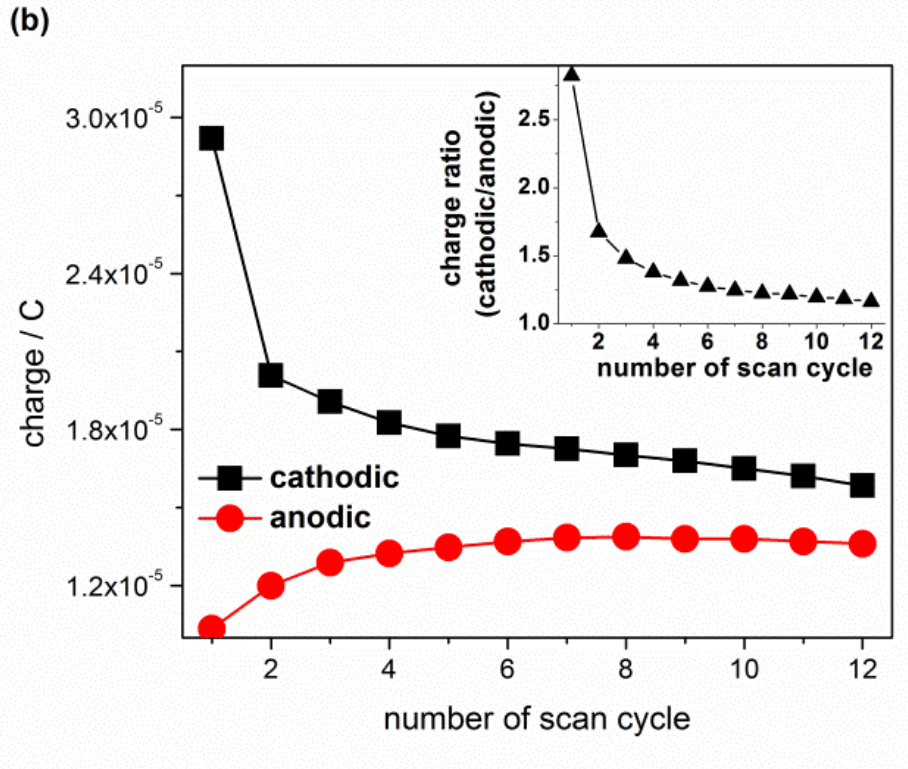
(b)
3.0x10-5
2.4x10-5
1.8x10-5
1.2x10-5
charge / C
cathodic
anodic
2
4
6
8
10
12
number of scan cycle
charge ratio
(cathodic/anodic)
2.5
2.0
1.5
1.0
2
4
6
8
10
12
number of scan cycle

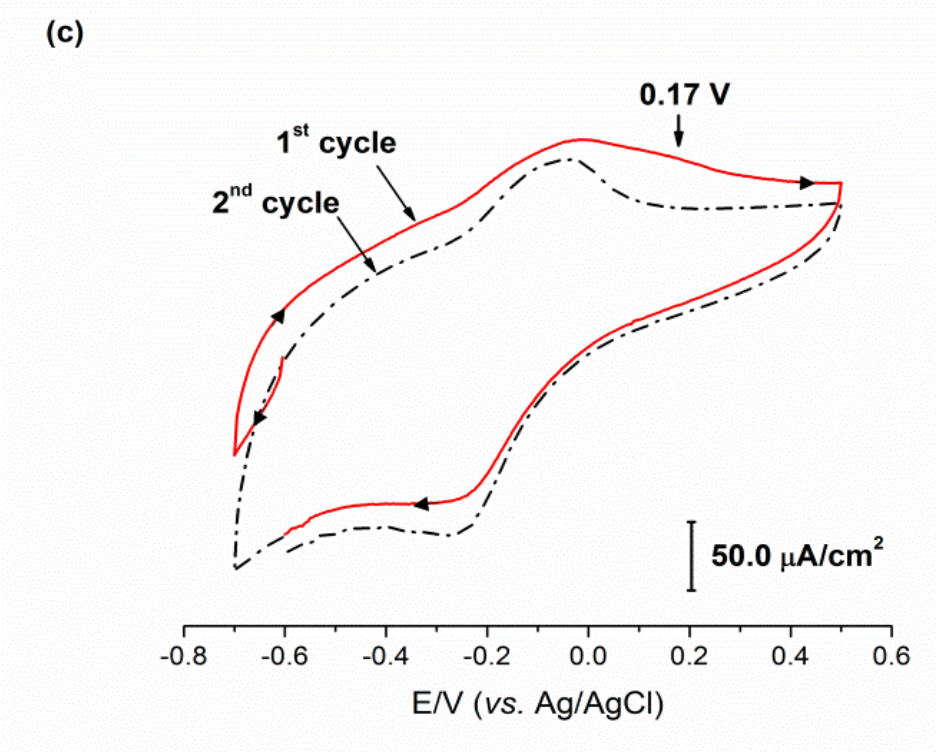
(c)
0.17 V
1st cycle
2nd cycle
50.0 μA/cm2
-0.8
-0.6
-0.4
-0.2
0.0
0.2
0.4
0.6
E/V (vs. Ag/AgCl)

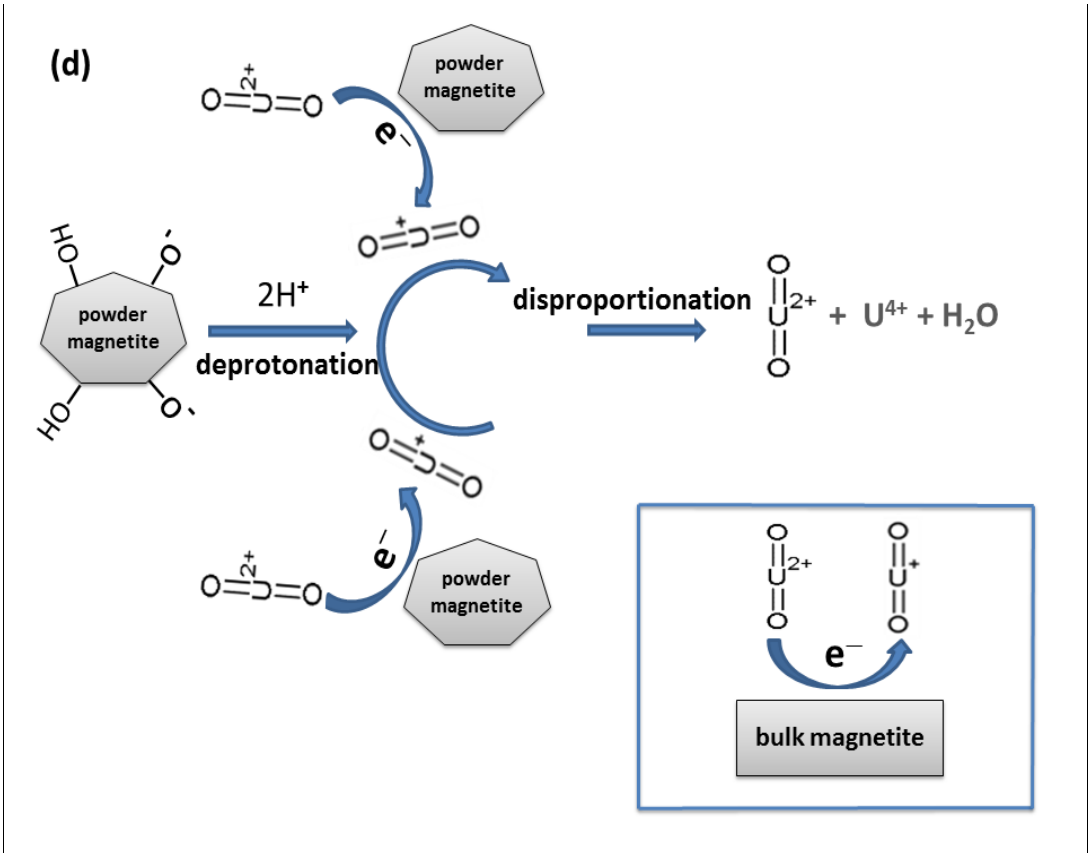
(d)
powder magnetite
e⁻
2H+
deprotonation
disproportionation
+ U4+ + H2O
powder magnetite
e⁻
powder magnetite
e⁻
bulk magnetite

Figure 2.5. (a) Cyclic voltammogram of uranyl redox reactions on the bulk magnetite electrode, and the dashed line in (a) is the voltammogram in a background solution containing 0.1M Na_2SO_4 of pH 3.5. The arrows in (a) point to the first scan cycle and grey regions highlight the integrated areas which were used to calculate the charge density of the last cycle. The cathodic and the anodic charge density changed as a function of the number of scan cycles (b). The inserted graph in (b) shows the charge ratio (ratio = cathodic charge / anodic charge) as a function of the scan cycle. The voltammogram of the bulk magnetite polarized at –0.6 V for 5 min before the cyclic voltammetric experiments (c). The solid line in (c) is the 1st cycle and the dashed line is the 2nd cycle. The diagram (d) shows the reduction of UO_2^{2+} to UO_2^{+} and subsequent disproportionation on the powder magnetite and the reduction of UO_2^{2+} to UO_2^{+} on the bulk magnetite. The pH of the UO_2^{2+} solution is 3.2 and the UO_2^{2+} concentration is 1.2 mM. The surface area of the electrode is 0.13 cm^2 and the scan rate is 50 mV/s.

Fitting the one-electron reduction of UO_2^{2+} on the bulk magnetite electrode

The bulk magnetite electrode was polarized at –1.0 V (*vs.* Ag/AgCl) for 20 s in background solutions and UO_2^{2+} containing solutions, respectively. The magnitude of the cathodic current decreased exponentially in both solutions with the increase of time (Fig. 2.6a). The current in the background electrolyte was mainly from charging the double layer and space charge layer of the magnetite and the potential H_2O reduction reaction. The current in the UO_2^{2+} solution is the combination of both reactions on the magnetite in background electrolyte and reactions of the UO_2^{2+} reduction. Thus, larger current magnitude was found for the voltammogram in the UO_2^{2+} solution than that in the background solution. By subtracting the current in the background solution from the current in the UO_2^{2+} solution, the current contribution from the UO_2^{2+} reduction alone can be extracted (Fig. 2.6a, inserted graph). Based on Eq. (4), the number of electrons *n* can be fitted to the slope of the data plotted in Fig. 2.6b. The data point at t = 1 s was not fitted because it is off the line of the other data in the range from 2 s to 10 s (if the data at 1 s was involved in the fitting, the slope is 1.0 and the R^2 is 0.97). The reason for the deviation of the data point at one second could be caused by the non-steady state at the very beginning of the experiments. After 10 s, the diffusion profile and the concentration gradient of UO_2^{2+} close to the electrode surface started to be interrupted by the solution convection, which is indicated by the alignment of the data point at 8 μA (Fig. 2.6b). The diffusion current after 10 s no longer obeys the ideal diffusion process described by the Cottrell equation (Eq. (4)); thus, data collected after 10 s was not used in the fitting. The number of electrons transferred was finally fitted to yield a value of 1.2, which is corresponds to the one-electron reduction of UO_2^{2+} to UO_2^{+}. Particularly,

even at −1.0 V, the reduction pathway of UO_2^{2+} still follows the one-electron reduction to UO_2^{+} rather than the two-electron reduction to U^{4+}. In comparison, the two-electron reduction mechanism of transferring electrons from Fe(II) to UO_2^{2+} was proposed by Boyanov et al. (2007). When the dominant Fe(II) species is monomeric Fe(II) at pH 7.5, which can only donate one electron, the reduction of UO_2^{2+} to U(IV) was not found. But rapid reduction to U(IV) was found when the pH was increased to 8.4, where Fe(II) oligomerized to $Fe(OH)_2$-like species with the possibility to donate two electrons. However, electrons here were provided by the potentiostat instead of limited by the type of Fe(II) species in the solution. Considering the acidic pH in this work is different from the basic conditions where $Fe(OH)_2$-like species donate two-electrons to U(VI), pH may be an important factor on determining the number of electrons transferred in the U(VI) reaction. In general, the fitting result, which is measured by another independent method, confirms that the UO_2^{2+} reduction on magnetite produces pentavalent uranium in current experimental conditions, at least as an intermediate state.

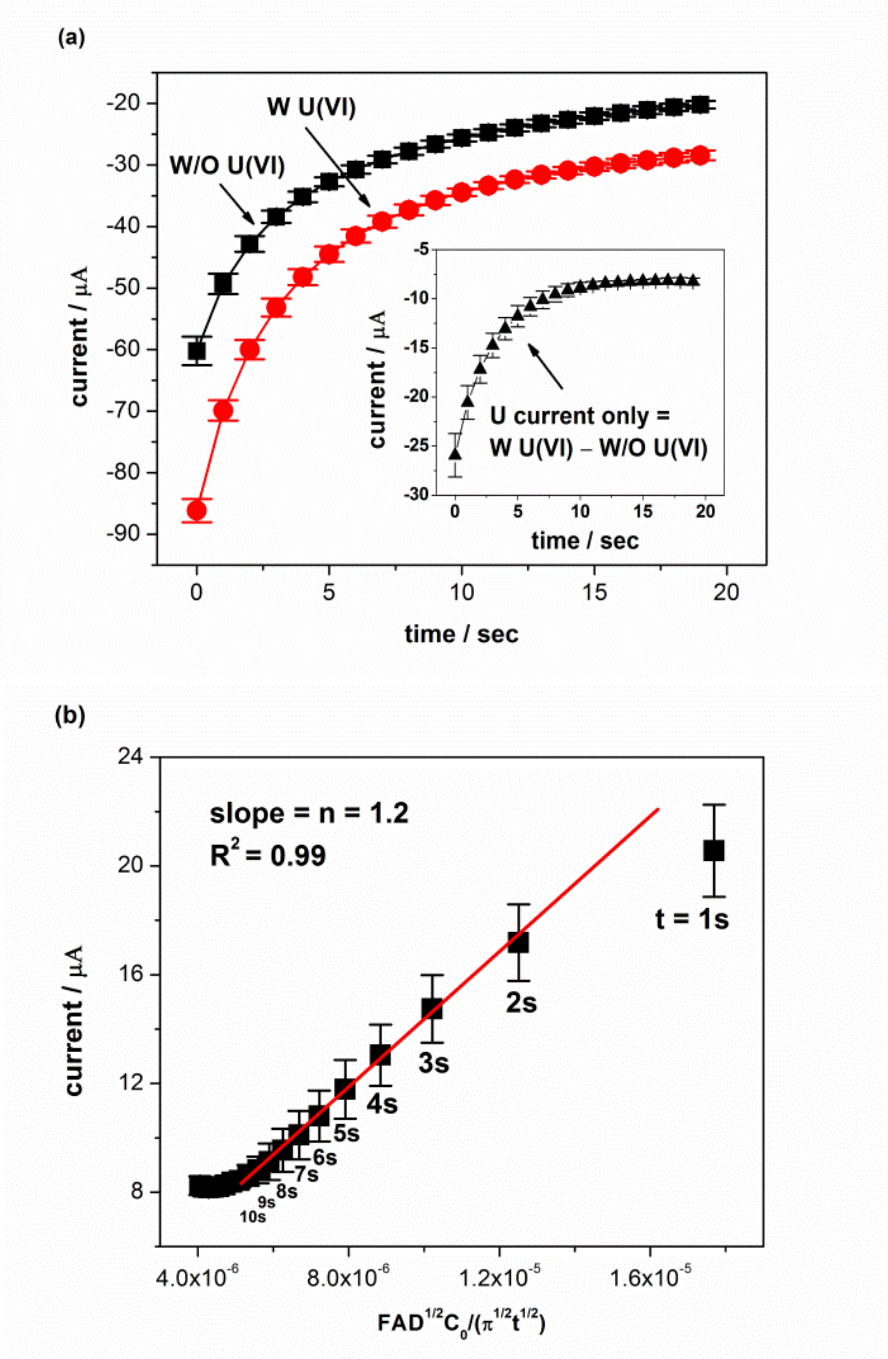

Figure 2.6. Potential step chronoamperometry results of the bulk magnetite electrode in solution with (W U(VI)) and without (W/O U(VI)) UO_2^{2+} (a) and the current contribution from the UO_2^{2+} reduction obtained by substracting the current in solutions without U(VI) from the current with U(VI) (a, inserted graph). Fitting of the number of electron transferred during the uranium reduction according to the Eq. (2) (b), where data points from 2 s to 10 s were used for fitting. The error bar represent the standard deviation from five separate measurements. The uranyl concentration is 1.2 mM with the background electrolyte of 0.1M Na_2SO_4 at pH=3.2, and the applied voltage is –1.0 V *vs*. Ag/AgCl.

Summary and conclusions

Redox reactions of uranyl ions on the surface of powdered and bulk magnetite in the aqueous solutions were investigated using electrochemical methods. Significant enhancement of the current signal from uranium redox reactions was observed by adding graphite powder into the magnetite powder. On the voltammgrams of the powder magnetite, the cathodic peak at –0.26 V *vs.* Ag/AgCl was assigned to the reduction of UO_2^{2+} to UO_2^{+} coupled with UO_2^{+} disproportionation. The first anodic peak at 0.09 V *vs.* Ag/AgCl was ascribed to the oxidation of UO_2^{+} to UO_2^{2+}. The other disproportionation product, U^{4+}, was oxidized back to UO_2^{2+} at 0.42 V *vs.* Ag/AgCl. These peak assignments are consistent with the conservation of charge within a complete scan cycle. These assignments were further confirmed by studying the relation between the peak height and the pH of the UO_2^{2+} solution by taking advantage of the proton-coupled electron transfer property of the UO_2^{+} disproportionation reaction. In contrast to the voltammograms of magnetite powder, one pair of peaks due to the redox reactions of UO_2^{2+}/UO_2^{+} were found on the voltammogram of the bulk magnetite electrode. The cathodic and anodic charge density gradually approached similar values and a charge ratio of 1.2. The absence of a U^{4+} oxidation peak indicated the presence of stabilized UO_2^{+}. The one-electron reduction of UO_2^{2+} on the bulk magnetite surface was further examined by the direct calculation of the number of electrons involved in the UO_2^{2+} reduction by fitting the potential step data to the Cottrell equation. The fast disproportionation of the UO_2^{+} found on the surface of powder magnetite is tentatively attributed to the catalytic sites which can adsorb and desorb protons. Electrochemical methods provide an approach to identify the reduction product within minutes of the reaction occurring. The short time scale permits investigations of intermediate oxidation states, such as the metastable UO_2^{+} species generated during the uranium reduction process. Ongoing experiments are focusing on the relation between the applied potential and the oxidation states of uranium deposited on the magnetite electrode using electrochemical-AFM, XPS, AES, and X-ray absorption spectroscopy.

Acknowledgement

This work is supported by the U.S. Office of Science, Basic Energy Sciences, Grant #DE-FG02-06ER15783. The authors acknowledge the valuable comments made by David Shoesmith (Department of Chemistry, University of Western Ontario) and Mark Meyerhoff (Department of Chemistry, University of Michigan).

References

Antonio M.R., Soderholm L. (2006) X-ray absorption spectroscopy of the actinides. In *The chemistry of the actinide and transactinide elements* (eds. Morss, L.R., Edelstein, N.M., Fuger, J.). Springer, Netherlands. pp. 3086-3198.

Athouel, L., Arcidiacono, P., Ramirez-Castro, C., Crosnier, O., Hamel, C., Dandeville, Y., Guillemet, P., Scudeller, Y., Guay, D., Belanger, D., Brousse, T. (2012) Investigation of cavity microelectrode technique for electrochemical study with manganese dioxides. *Electrochim. Acta* **86**, 268-276.

Awakura, Y., Sato, K., Majima, H., Hirono, S. (1987) The measurement of the diffusion-coefficient of U(VI) in aqueous uranyl sulfate-solutions. *Metall Trans B* **18**, 19-23.

Bard, A.J., Faulkner, L.R. (2001) Electrochemical methods*: Fundamentals and applications*. Second edition ed. John Wiley & Sons, Inc., Hoboken. pp. 753-756, 161-163, 810, 228-232, 36-37.

Becker, U., Rosso, K.M., Hochella, M.F. (2001) The proximity effect on semiconducting mineral surfaces: A new aspect of mineral surface reactivity and surface complexation theory? *Geochim. Cosmochim. Acta* **65**, 2641-2649.

Belai, N., Frisch, M., Ilton, E.S., Ravel, B., Cahill, C.L. (2008) Pentavalent uranium oxide via reduction of UO_2^{2+} under hydrothermal reaction conditions. *Inorg Chem* **47**, 10135-10140.

Boyanov, M.I., O'Loughlin, E.J., Roden, E.E., Fein, J.B., Kemner, K.M. (2007) Adsorption of Fe(II) and U(VI) to carboxyl-functionalized microspheres: The influence of speciation on uranyl reduction studied by titration and XAFS. *Geochim. Cosmochim. Acta* **71**, 1898-1912.

Broczkowski, M.E., Noel, J.J., Shoesmith, D.W. (2007) The influence of temperature on the anodic oxidation/dissolution of uranium dioxide. *Electrochim. Acta* **52**, 7386-7395.

Burns, P.C. (1999) The Crystal Chemistry of Uranium. In *Uranium: Mineralogy, geochemistry and the environment*. (eds. Burns, P.C. and Finch, R) The Mineralogical Society of America. Washington, DC. PP. 23-32.

Burns, P.C., Finch, R.J. (1999) Wyartite: Crystallographic evidence for the first pentavalent-uranium mineral. *Am. Mineral* **84**, 1456-1460.

Cachet-Vivier, C., Vivier, V., Cha, C.S., Nedelec, J.Y., Yu, L.T. (2001) Electrochemistry of powder material studied by means of the cavity microelectrode (CME). *Electrochim. Acta* **47**, 181-189.

Castro, P.A., Vago, E.R., Calvo, E.J. (1996) Surface electrochemical transformations on spinel iron oxide electrodes in aqueous solutions. *J. Chem. Soc.-Faraday Trans*. **92**, 3371-3379

Cha, C.S., Li, C.M., Yang, H.X., Liu, P.F. (1994) Powder microelectrodes. *J. Electroanal. Chem.* **368**, 47-54.

Cornell, R.M., Schwertmann, U. (1996) *The iron oxides: Structure, properties, reactions, occurrence and uses.* Wiley-VCH, Weinheim. PP. 28-30.

Dickinson, M., Scott, T.B. (2010) The application of zero-valent iron nanoparticles for the remediation of a uranium-contaminated waste effluent. *J. Hazard Mater* **178**, 171-179.

Dodge, C.J., Francis, A.J., Gillow, J.B., Halada, G.P., Eng, C., Clayton, C.R. (2002) Association of uranium with iron oxides typically formed on corroding steel surfaces. *Environ. Sci. Technol*. **36**, 3504-3511.

Ekstrom, A. (1974) Kinetics and mechanism of disproportionation of uranium(V). *Inorg. Chem.* **13**, 2237-2241.

Elzinga, E.J., Tait, C.D., Reeder, R.J., Rector, K.D., Donohoe, R.J., Morris, D.E. (2004) Spectroscopic investigation of U(VI) sorption at the calcite-water interface. *Geochim. Cosmochim. Acta* **68**, 2437-2448.

Fortier, S., Hayton, T.W. (2010) Oxo ligand functionalization in the uranyl ion (UO_2^{2+}). *Coord. Chem. Rev*. **254**, 197-214.

Goldik, J.S., Nesbitt, H.W., Noel, J.J., Shoesmith, D.W. (2004) Surface electrochemistry of UO_2 in dilute alkaline hydrogen peroxide solutions. *Electrochim. Acta* **49**, 1699-1709.

Gorski, C.A., Handler, R.M., Beard, B.L., Pasakarnis, T., Johnson, C.M., Scherer, M.M. (2012) Fe atom exchange between aqueous Fe^{2+} and magnetite. *Environ. Sci. Technol*.**46**, 12399-12407.

Gorski, C.A., Nurmi, J.T., Tratnyek, P.G., Hofstetter, T.B., Scherer, M.M. (2010) Redox behavior of magnetite: Implications for contaminant reduction. *Environ. Sci. Technol*.**44**, 55-60.

Gorski, C.A., Scherer, M.M. (2009) Influence of magnetite stoichiometry on Fe^{II} uptake and nitrobenzene reduction. *Environ. Sci. Technol*.**43**, 3675-3680.

Gorski, C.A., Scherer, M.M. (2010) Determination of nanoparticulate magnetite stoichiometry by Mössbauer spectroscopy, acidic dissolution, and powder X-ray diffraction: A critical review. *Am. Mineral* **95**, 1017-1026.

Graves, C.R., Scott, B.L., Morris, D.E., Kiplinger, J.L. (2009) Selenate and tellurate complexes of pentavalent uranium. *Chem. Commun.* 776-778.

Graves, C.R., Vaughn, A.E., Schelter, E.J., Scott, B.L., Thompson, J.D., Morris, D.E., Kiplinger, J.L. (2008) Probing the chemistry, electronic structure and redox energetics in organometallic pentavalent uranium complexes. *Inorg. Chem.* **47**, 11879-11891.

Gu, B., Liang, L., Dickey, M.J., Yin, X., Dai, S. (1998) Reductive precipitation of uranium(VI) by zero-valent iron. *Environ. Sci. Technol*.**32**, 3366-3373.

Heming He, M.B., Kevin O'Neil, Derrick Ofori, Oleg Semenikhin, David Shoesmith (2012) Corrosion of nuclear fuel (UO_2) inside a failed nuclear waste container (NWMO TR-2012-09). Western University, Toronto, Canada. pp. 29-32.

Ilton, E.S., Bagus, P.S. (2011) XPS determination of uranium oxidation states. *Surf. Interface Anal* **43**, 1549-1560.

Ilton, E.S., Boily, J.F., Buck, E.C., Skomurski, F.N., Rosso, K.M., Cahill, C.L., Bargar, J.R., Felmy, A.R. (2010) Influence of dynamical conditions on the reduction of U^{VI} at the magnetite-solution interface. *Environ. Sci. Technol*.**44**, 170-176.

Ilton, E.S., Haiduc, A., Cahill, C.L., Felmy, A.R. (2005) Mica surfaces stabilize pentavalent uranium. *Inorg. Chem.***44**, 2986-2988.

Ilton, E.S., Pacheco, J.S.L., Bargar, J.R., Shi, Z., Liu, J., Kovarik, L., Engelhard, M.H., Felmy, A.R. (2012) Reduction of U(VI) incorporated in the structure of hematite. *Environ. Sci. Technol.***46**, 9428-9436.

Kern, D.M.H., Orlemann, E.F. (1949) The potential of the uranium(V), uranium(VI) couple and the kinetics of uranium(V) disproportionation in perchlorate media. *J. Am. Chem. Soc* **71**, 2102-2106.

Komlos, J., Mishra, B., Lanzirotti, A., Myneni, S.C.B., Jaffe, P.R. (2008) Real-time speciation of uranium during active bioremediation and U(IV) reoxidation. *J. Environ. Eng-ASCE* **134**, 78-86.

Konings, R.J.M., Morss, L.R., Fuger, J. (2006) Termodynamic properties of actinides and actinide compounds. In *The chemistry of the actinide and transactinide elements* (eds. Morss, L.R., Edelstein, N.M., Fuger, J.). Springer, Netherlands. pp. 2127-2131.

Latta, D.E., Gorski, C.A., Boyanov, M.I., O'Loughlin, E.J., Kemner, K.M., Scherer, M.M. (2012) Influence of magnetite stoichiometry on U(VI) reduction. *Environ. Sci. Technol.***46**, 778-786.

Liger, E., Charlet, L., Van Cappellen, P. (1999) Surface catalysis of uranium(VI) reduction by iron(II). *Geochim. Cosmochim. Acta* **63**, 2939-2955.

Locatelli, C., Minguzzi, A., Vertova, A., Cava, P., Rondinini, S. (2011) Quantitative studies on electrode material properties by means of the cavity microelectrode. *Anal. Chem.* **83**, 2819-2823.

Luo, Y., Hughes, J.M., Rakovan, J., Pan, Y.M. (2009) Site preference of U and Th in Cl, F, and Sr apatites. *Am. Mineral* **94**, 345-351.

Missana, T., Maffiotte, U., Garcia-Gutierrez, M. (2003) Surface reactions kinetics between nanocrystalline magnetite and uranyl. *J. Colloid Interface Sci.***261**, 154-160.

Morris, D.E. (2002) Redox energetics and kinetics of uranyl coordination complexes in aqueous solution. *Inorg. Chem.* **41**, 3542-3547.

Morrison, S.J., Metzler, D.R., Carpenter, C.E. (2001) Uranium precipitation in a permeable reactive barrier by progressive irreversible dissolution of zerovalent iron. *Environ. Sci. Technol.***35**, 385-390.

Mougel, V., Biswas, B., Pecaut, J., Mazzanti, M. (2010) New insights into the acid mediated disproportionation of pentavalent uranyl. *Chem. Commun*. **46**, 8648-8650.

Neck, V., Kim, J.I. (2001) Solubility and hydrolysis of tetravalent actinides. *Radiochimica Acta.* **89**, 1-16.

Nocton, G., Horeglad, P., Pecaut, J., Mazzanti, M. (2008) Polynuclear cation-cation complexes of pentavalent uranyl: Relating stability and magnetic properties to structure. *J. Am. Chem. Soc*. **130**, 16633-16645.

Nurmi, J.T., Tratnyek, P.G. (2008) Electrochemical studies of packed iron powder electrodes: Effects of common constituents of natural waters on corrosion potential. *Corros. Sci*.**50**, 144-154.

Nurmi, J.T., Tratnyek, P.G., Sarathy, V., Baer, D.R., Amonette, J.E., Pecher, K., Wang, C.M., Linehan, J.C., Matson, D.W., Penn, R.L., Driessen, M.D. (2005) Characterization and properties of metallic iron nanoparticles: Spectroscopy, electrochemistry, and kinetics. *Environ. Sci. Technol.***39**, 1221-1230.

Peng, F.F., Zhang, Y., Gu, N. (2008) Size-dependent peroxidase-like catalytic activity of Fe_3O_4 nanoparticles. *Chin. Chem. Lett.* **19**, 730-733.

Petitto, S.C., Tanwar, K.S., Ghose, S.K., Eng, P.J., Trainor, T.P. (2010) Surface structure of magnetite (111) under hydrated conditions by crystal truncation rod diffraction. *Surf. Sci*. **604**, 1082-1093.

Rakovan, J., Reeder, R.J., Elzinga, E.J., Cherniak, D.J., Tait, C.D., Morris, D.E. (2002) Structural characterization of U(VI) in apatite by X-ray absorption spectroscopy. *Environ. Sci. Technol.***36**, 3114-3117.

Razdan, M., Hall, D.S., Keech, P.G., Shoesmith, D.W. (2012) Electrochemical reduction of hydrogen peroxide on simfuel (UO_2) in acidic pH conditions. *Electrochim. Acta* **83**, 410-419.

Reeder, R.J., Nugent, M., Tait, C.D., Morris, D.E., Heald, S.M., Beck, K.M., Hess, W.P., Lanzirotti, A. (2001) Coprecipitation of uranium(VI) with calcite: XAFS, micro-XAS, and luminescence characterization. *Geochim. Cosmochim. Acta* **65**, 3491-3503.

Renock, D., Becker, U. (2010) A first principles study of the oxidation energetics and kinetics of realgar. *Geochim. Cosmochim. Acta* **74**, 4266-4284.

Renock, D., Mueller, M., Yuan, K., Ewing, R.C., Becker, U. (2013) The energetics and kinetics of uranyl reduction on pyrite, hematite, and magnetite surfaces: A powder microelectrode study. *Geochim. Cosmochim. Acta* **118**, 56-71.

Renshaw, J.C., Butchins, L.J.C., Livens, F.R., May, I., Charnock, J.M., Lloyd, J.R. (2005) Bioreduction of uranium: Environmental implications of a pentavalent intermediate. *Environ. Sci. Technol.***39**, 5657-5660.

Rosso, K.M., Becker, U. (2003) Proximity effects on semiconducting mineral surfaces II: Distance dependence of indirect interactions. *Geochim. Cosmochim. Acta* **67**, 941-953.

Rovira, M., El Aamrani, S., Duro, L., Gimenez, J., de Pablo, J., Bruno, J. (2007) Interaction of uranium with *in situ* anoxically generated magnetite on steel. *J. Hazard Mater* **147**, 726-731.

Scherer, M.M., Westall, J.C., ZiomekMoroz, M., Tratnyek, P.G. (1997) Kinetics of carbon tetrachloride reduction at an oxide-free iron electrode. *Environ. Sci. Technol.* **31**, 2385-2391.

Schindler, M., Hawthorne, F.C., Freund, M.S., Burns, P.C. (2009) XPS spectra of uranyl minerals and synthetic uranyl compounds. I: The U 4f spectrum. *Geochim. Cosmochim. Acta* **73**, 2471-2487.

Scott, T.B., Allen, G.C., Heard, P.J., Randell, M.G. (2005) Reduction of U(VI) to U(IV) on the surface of magnetite. *Geochim. Cosmochim. Acta* **69**, 5639-5646.

Singer, D.M., Chatman, S.M., Ilton, E.S., Rosso, K.M., Banfield, J.F., Waychunas, G.A. (2012a) Identification of simultaneous U(VI) sorption complexes and U(IV) nanoprecipitates on the magnetite (111) surface. *Environ. Sci. Technol.* **46**, 3811-3820.

Singer, D.M., Chatman, S.M., Ilton, E.S., Rosso, K.M., Banfield, J.F., Waychunas, G.A. (2012b) U(VI) sorption and reduction kinetics on the magnetite (111) surface. *Environ. Sci. Technol.* **46**, 3821-3830.

Skomurski, F.N., Ilton, E.S., Engelhard, M.H., Arey, B.W., Rosso, K.M. (2011) Heterogeneous reduction of U^{6+} by structural Fe^{2+} from theory and experiment. *Geochim. Cosmochim.* Acta **75**, 7277-7290.

Steele, H., Taylor, R.J. (2007) A theoretical study of the inner-sphere disproportionation reaction mechanism of the pentavalent actinyl ions. *Inorg. Chem.* **46**, 6311-6318.

Sturchio, N.C., Antonio, M.R., Soderholm, L., Sutton, S.R., Brannon, J.C. (1998) Tetravalent uranium in calcite. *Science* **281**, 971-973.

Sun, Z.X., Su, F.W., Forsling, W., Samskog, P.O. (1998) Surface characteristics of magnetite in aqueous suspension. *J. Colloid Interface Sci.* **197**, 151-159.

Sunder, S., Miller, N.H., Shoesmith, D.W. (2004) Corrosion of uranium dioxide in hydrogen peroxide solutions. *Corros. Sci.* **46**, 1095-1111.

Wander, M.C.F., Shuford, K.L. (2012) A theoretical study of the qualitative reaction mechanism for the homogeneous disproportionation of pentavalent uranyl ions. *Geochim. Cosmochim. Acta* **84**, 177-185.

Wang, Z.M., Lee, S.W., Catalano, J.G., Lezama-Pacheco, J.S., Bargar, J.R., Tebo, B.M., Giammar, D.E. (2013) Adsorption of uranium(VI) to manganese oxides: X-ray absorption spectroscopy and surface complexation modeling. *Environ. Sci. Technol.* **47**, 850-858.

White, A.F., Peterson, M.L., Hochella, M.F. (1994) Electrochemistry and dissolution kinetics of magnetite and ilmenite. *Geochim. Cosmochim. Acta*. **58**, 1859-1875

Wu, N.L., Wang, S.Y., Han, C.Y., Wu, D.S., Shiue, L.R. (2003) Electrochemical capacitor of magnetite in aqueous electrolytes. *J. Power Sources* **113**, 173-178.

Appendix A

Supporting Information

A set of experiments was performed to test the reproducibility of the peak position and peak current of the cavity microelectrode. This hypothesis was assessed by measuring the voltammograms of ferro/ferricyanide couple on magnetite + graphite for freshly prepared electrodes. A series of voltammograms (Fig S2.1 and Fig S2.2) were obtained in a solution containing 0.01 M ferrocyanide using the same microcavity electrode used for data collection in the manuscript. The electrode was packed with a magnetite + graphite mixture at a ratio of 10 wt.%.

Figure SI1 shows the CV data for a newly-packed electrode scanned for 20 cycles (bottom curve), and then the same electrode was continuously scanned for another three times and each time with 10 cycles (electrode was not removed from the solution). The first 20 cycles show a widening of the Fe(II)/Fe(III) peak separation as well as an increase in peak current. The peak position and height in the CV stabilizes after about 15-20 cycles.

In order to test the reproducibility over different samples, Figure S2.2 overlays all experimental data for the 10 newly-prepared electrodes. During each run, the CV data were measured for the newly-prepared electrode for 20 cycles (left panel) and then the same electrodes were scanned for another 10 cycles to measure equilibrium conditions (right panel). Both peak separations and amplitudes on each newly-made electrode stabilized after 15-20 scans. One possible explanation for the increase of the Fe(II)/Fe(III) peak currents is that the packed electrode requires a brief “break-in” period before the electrochemical surface area is fully accessed by the solution. Another possible explanation could be due to progressive removal of passivation layers formed on the surface of the graphite and magnetite particles. Note diminishing reduction (negative) currents at potentials more negative than -0.4 V with increasing number of cycles.

From the voltammograms in Fig S2.2, the peak values of the last scan in each experiment are listed in Table S2.1 along with the calculated uncertainty in the measurement. The standard deviation of the peak current values is estimated to be ±0.020 μA. The peak separations are listed in Table S2.2 with the calculated uncertainty of ± 5.5 mV.

In summary, this type of electrode shows reproducible data after a break-in period of 15-20 cycles, which could be resulted from removing of the oxidized layer on the surface of magnetite.

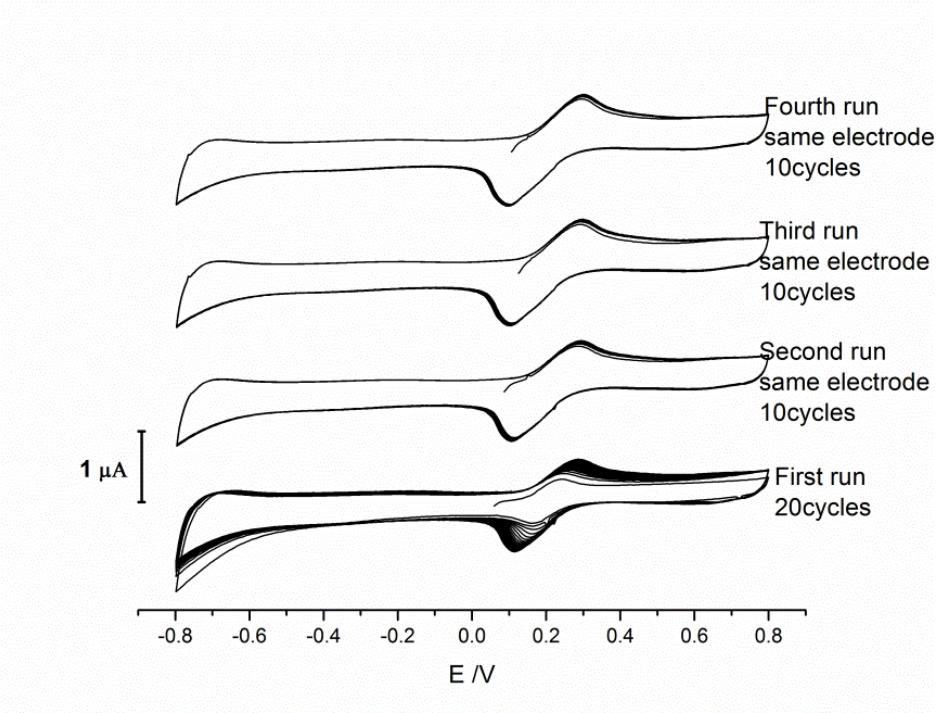

Figure S 2.1 Reproducible test in ferrocyanide solution using magnetite + graphite electrode, the test was run on a freshly made electrode for 20 cycles and then run on the same electrode for 3 times and each time with 10 cycles.

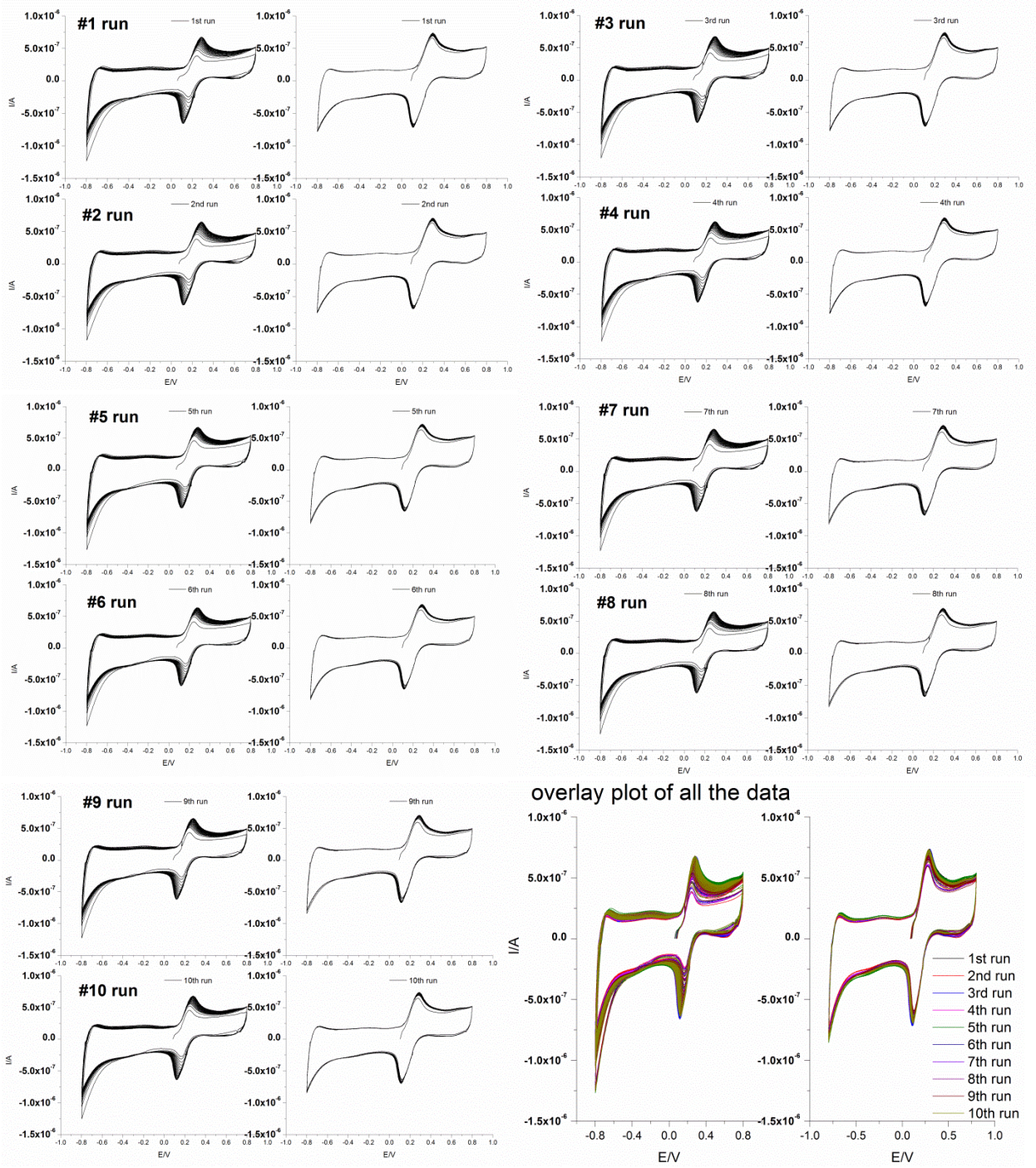

Figure S 2.2 Reproducible test (10 runs) in ferrocyanide solution using magnetite + graphite electrode. Each test was run on a freshly made electrode for 20 cycles (left panel) and then run on the same electrode for another 10 cycles (right panel). The last plot showed the overlay of all the 10 runs on the same graph. All the plots have the same current scales.

Table S 2.1 Peak current values from Fig SI2 and the standard deviation of the peak current values, all the peak current values are read from the last cycle in each run.

		Freshly prepared electrode 20 cycle run	Same electrode 10 cycle run	
electrode #	Ipc/μA	Ipa/μA	Ipc/μA	Ipa/μA
1	-0.640	0.675	-0.677	0.731
2	-0.618	0.650	-0.681	0.701
3	-0.657	0.676	-0.707	0.737
4	-0.600	0.629	-0.683	0.683
5	-0.609	0.672	-0.659	0.728
6	-0.600	0.637	-0.653	0.690
7	-0.625	0.653	-0.618	0.712
8	-0.616	0.644	-0.672	0.698
9	-0.622	0.625	-0.672	0.698
10	-0.642	0.681	-0.699	0.736
STD	0.0177	0.0196	0.0237	0.0191
Average STD		0.020 μA		

Table S 2.2 Peak separations obtained from Fig SI2. The separations of the first cycle and the last cycle were listed in each type of tests.

	Freshly prepared electrode 20 cycle run		Same electrode 10 cycle run	
electrode #	1^{st} cycle/mV	20^{th} cycle/mV	1^{st} cycle/mV	10^{th} cycle/mV
1	77.9	168.9	168.8	188.1
2	77.8	162.1	170.6	180.3
3	71.5	162.5	167.4	186.7
4	71.5	162.0	164.1	176.9
5	77.1	160.7	157.9	176.9
6	80.5	157.8	148.2	174.0
7	83.7	164.2	157.9	177.3
8	77.2	160.9	141.4	170.3
9	77.1	160.7	141.2	173.7
10	77.3	157.7	151.6	177.4
STD	3.4	3.0	10.4	5.3
Average STD	5.5 mV			

Chapter 3 Electrochemical and spectroscopic evidence on the one-electron reduction of U(VI) to U(V) on magnetite

Abstract

Reduction of U(VI) to U(IV) on mineral surfaces is often considered a one-step two-electron process. However, stabilized U(V), with no evidence of U(IV), found in recent studies indicates U(VI) can undergo a one-electron reduction to U(V) without further progression to U(IV). Here we investigate mechanisms of uranium reduction by reducing U(VI) electrochemically on a magnetite electrode at pH 3.4. Cyclic voltammetry confirms the one-electron reduction of U(VI) to U(V). Formation of nano-size uranium precipitates on the magnetite surface at reducing potentials and dissolution of the solids at oxidizing potentials is observed by *in situ* electrochemical-AFM. XPS analyses of the magnetite electrodes polarized in uranium solutions at voltages from -0.1 to -0.9 V ($E^0_{U(VI)/U(V)}$ = -0.135V *vs.* Ag/AgCl) show the presence of only U(V) and U(VI). The sample with the highest U(V) to U(VI) ratio determined by XPS was prepared at -0.7 V, where the longest average U–O_{axial} distance of 2.05 ± 0.01 Å was evident in the same sample revealed by the EXAFS analysis. The results demonstrate that the electrochemical reduction of U(VI) on magnetite only yields U(V), even at a potential of -0.9 V, which favors the one-electron reduction mechanism. U(V) does not disproportionate but is stabilized on magnetite through precipitation of mixed-valence state U(V)/U(VI) solids.

Introduction

Extensive investigations on uranium reduction by minerals and bacteria are motivated by environmental concerns of immobilizing uranium generated from nuclear weapons production and from its relevance to the geological disposal of nuclear wastes in the subsurface environment[1-7]. Remediation of uranium-contaminated environments often relies on the reduction of the soluble uranyl ion ($U(VI)O_2^{2+}$) to sparingly soluble U(IV) by gaining two electrons[8-10]. However, recent studies have identified the U(V) intermediate associated with iron oxides[11-15], micas[16], and bacterial respiration[17]. In some cases, U(V) appears to be long lived and relatively stable[12, 16, 13, 14]. Thus, in these systems, further reduction of U(V), either through another one-electron reduction to U(IV) or through disproportionation of UO_2^+ ($2U(V) \rightarrow U(VI) + U(IV)$), becomes the rate-limiting step in the overall process of uranium reduction.

The well-known one-electron reduction of $U(VI)O_2^{2+}$ to $U(V)O_2^+$ was first observed using electrochemistry methods on a dropping mercury electrode[18]. This one-electron reduction was further confirmed on the surfaces of metallic electrodes in numerous electrochemistry experiments[19-23]. Apparently, surface properties have significant influences on the redox kinetics. Recently, we investigated the reduction of uranium on the surfaces of the electrodes made of semiconducting iron sulfide and Fe(II,III)-oxide minerals in order to verify if the one-electron reduction observed on metallic electrodes can be observed on mineral electrodes as well[24]. The results were consistent with reduction to U(V) followed in some cases by disproportionation[24, 25]. However, spectroscopic methods were not applied. Magnetite (Fe_3O_4) is a ubiquitous Fe(II/III)-bearing mineral in natural environments and is the corrosion product of iron under anoxic conditions relevant to subsurface waste disposal environments[26]. Reduction of UO_2^{2+} to U(IV) and U(V) has been identified on the surface of magnetite and in secondary precipitates where

structural Fe(II) functioned as the reductant[27, 4, 6, 7, 10, 28, 15]. The objective of this study is to examine whether the one-electron reduction of UO_2^{2+} can occur on the surface of magnetite using electrochemical and spectroscopic/microscopic techniques, where the redox potential close to the magnetite surface-liquid interface is controlled by the applied voltage.

Materials and Methods

Electrochemistry and electrochemical-AFM

A computer-controlled potentiostat (Princeton Applied Research Model 263A) was used to apply voltages to the magnetite working electrode with respect to a Ag/AgCl (saturated KCl) reference electrode (the reference for all potentials reported in this manuscript), as well as to measure the current that passed between the working electrode and a Pt counter electrode. The working electrode is made of a natural magnetite sample (Mineville N.Y.). Details regarding the fabrication of the magnetite electrode can be found in reference[25] and in the supporting information (SI, Figure S3.1). Cyclic voltammetry experiments were started from the open circuit potential (OCP) and scanned first to more positive potentials until the switching potential was reached. The potential scan was repeated for multiple cycles, until stable voltammograms were obtained. Solutions were degassed with Ar for at least 30 min prior to the cyclic voltammetry experiments. All voltammograms plot negative current for the cathodic scan and positive current for the anodic scan.

In situ electrochemical-AFM imaging was conducted in the Peak Force Tapping mode (Bruker ScanAsyst) using the in-house-constructed electrochemical cell (SI, Figure S3.2). AFM probes (ScanAsyst-Fluid+, Bruker) consisted of silicon nitride cantilevers (resonant frequency: 120-180 kHz; spring constant: 0.7 N/m) with integrated silicon tips (height: 2.5-8.0 μm, radius: 2nm). A series of constant potentials were applied to the magnetite working electrode for 30 s

and the images at certain potentials were captured afterwards. The imaging started at OCP (~0.1 V) with the magnetite electrode being consecutively polarized to more negative potentials with images captures every 0.05 V (2 min capture time per image) up to the switching potential of -0.7 V. For the reverse anodic scan, images were captured every 0.1 V from -0.7 V to 0.5 V with starting and finishing at the OCP of 0.1 V. The solutions used for the electrochemical-AFM were Ar-degassed for 1 h before the experiments. The whole electrochemical-AFM cell was placed inside the vibration isolation enclosure of the AFM system (flushed continuously with Ar gas).

UO_2^{2+} solutions (0.5 and 1 mM) were prepared by dissolving uranyl nitrate hexahydrate crystals [$UO_2(NO_3)_2 \cdot 6H_2O$] (International Bio-Analytical Industries, Inc.) into a 0.1 M NaCl solution (Fisher Scientific), which served as the background electrolyte. The pH of the solutions was adjusted to 3.4 by 0.1 M HCl as measured using an Orion 111A pH meter.

X-ray photoelectron spectroscopy

The samples used for XPS analysis were prepared by imposing certain potentials on the magnetite electrode for 3 min in a 1 mM UO_2^{2+} solution with 0.1 M NaCl as the background electrolyte at pH = 3.4. After electrochemical deposition, the electrode was rinsed with Ar degassed DI water of the same pH and then dried in an Ar atmosphere prior to storage inside a glove bag (95% N_2 + 5% H_2). The samples were then sealed in polyethylene bags using an Impulse poly bag sealer (ULINE) inside the glove bag and transferred for XPS analysis. Spectra of U 4f, Fe 2p, and C 1s were measured using the Kratos Axis Ultra XPS equipped with a monochromatic Al-Kα source and charge compensation system. A pass energy of 40 eV with sweep steps of 0.05 eV were applied. Spectra from 20 sweeps were averaged and the energy scale calibrated to the adventitious C1s line at 284.8 eV. Peak fitting was done using the CasaXPS software package.

Auger electron spectroscopy

Auger electron spectra were measured using a PHI 680 with a double-pass cylindrical analyzer under a pressure of 5×10^{-9} Torr. The surface of the sample was sputtered using an Ar^+ beam to remove adventitious carbon. The 3 μA beam current was used for sputtering uranium-deposited magnetite samples for 30~60 s in order to prevent damage to the uranium species on top of the surface; however, the pure UO_2 and Fe_3O_4 standards were sputtered for 10 min. AES spectra were acquired from a scanning area of 200 μm × 200 μm by averaging 10 scans using a 10 kV and 10 nA beam with an energy step of 0.2 eV over the kinetic energy region of 10~800 eV. The derivative spectra were obtained using MultiPak.

X-ray absorption spectroscopy

The samples used for XAS analysis were prepared, stored, and transferred using similar methods as for the XPS samples described above, except a longer polarization time of 10 min was used for uranium deposition due to the lower surface sensitivity of XAS compared to XPS. The samples were further sealed using Kapton film in addition to the polyethylene bags. U L_3-edge X-ray absorption spectra were recorded in fluorescence mode at beamline 12-BM-B equipped with a 13-element Ge detector and Si [111] monochromator at the Advanced Photon Source, Argonne National Laboratory. The incident X-ray energy was calibrated with a Zr foil standard (inflection point energy of 17998.0 eV). XANES and EXAFS data were measured with step sizes of 0.5 eV and 0.05 $Å^{-1}$, respectively. Spectra from multiple scans (3~8) on each sample were aligned and averaged in Athena[29]. EXAFS data were fitted using Artemis[29] with the theoretical functions of FEFF 6.0 [30] (see SI for fitting methods).

Results and Discussion

Cyclic voltammetry

The magnetite electrode was first scanned at various scan rates (0.05 to 1 V/s) in 0.1 M NaCl electrolyte in order to obtain the background current in solutions without uranium. The magnitude of the current increased with scan rate (Figure 3.1a). The shapes of the voltammograms indicate the characteristic capacitance behavior of a semiconductor, in which the observed current was mainly attributed to the charge and discharge of the space-charge layer.[31, 32]

In the uranium solution, extra redox peaks were identified (Figure 3.1b; also see SI, Figure S3.3a, Table S3.1 for OPCs). The anodic peaks were found on top of the flat anodic background current, whereas the cathodic peaks were distorted and embedded inside the tilted cathodic background current (Figure 3.1a, b). Through integration of the area under the voltammetric curve in Figure 3.1a with the corresponding background current as the baseline from Figure 3.1b, the total amount of charge transferred due to the uranium redox reactions can be calculated (charge integration methods, see SI, Figure S3.3c, d). Charges transferred during the cathodic and the anodic scans have similar values for a given scan rate (SI, Figure S3.3b) indicating the reduced uranium species in the cathodic scan are all preserved and oxidized back to the initial hexavalent state in the reverse anodic scan. This further confirms that the heterogeneous reduction of U(VI) on the surface of the magnetite electrode is not coupled to U(V) disproportionation, in which case less charge would be found under the anodic peak caused by oxidation of U(V) back to U(VI) (see Chapter 2, page 22).

The change in the peak shape with scan rate reflects the kinetics of the redox reactions on the electrode surface[33]. When the scan rate is increased from 0.05 to 1 V/s, the cathodic and anodic peak positions move to lower and higher voltages, respectively, accompanied by the increase of

the corresponding peak currents. A linear relation was identified between the cathodic/anodic peak current values and the square root of scan rates (Figure 3.1c), indicating a diffusion-controlled reaction described by the Randles-Sevcik equation[33]

$$i_{pc} = (2.69 \times 10^5) n^{3/2} A D_0^{1/2} C_0^* v^{1/2} \quad (1)$$

where i_{pc} is the forward peak current (the cathodic peak current in this case), n the number of electrons transferred per redox change, A the surface area of the electrode, D_0 the diffusion coefficient of uranyl (6.2×10^{-6} cm^2/s)[19], C_0^* the initial concentration of UO_2^{2+} (1 mM), and v the scan rate. The number of electrons transferred per redox change was fitted based using equation (1) and the results (SI, Figure S3.4) show that n equals 1.0, consistent with the one-electron reduction of UO_2^{2+} to UO_2^+ on the magnetite surface.

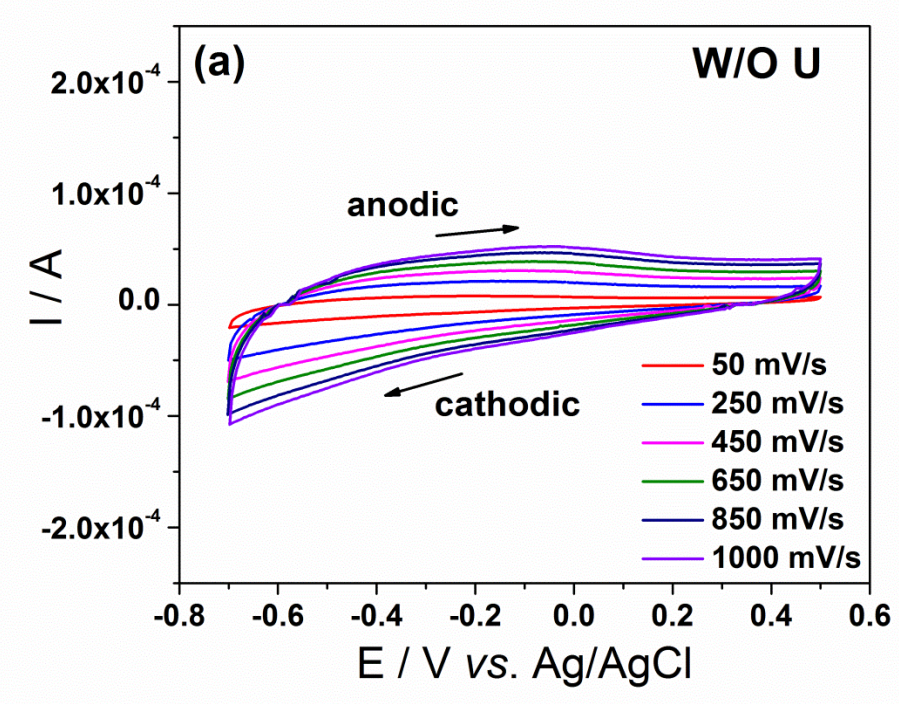

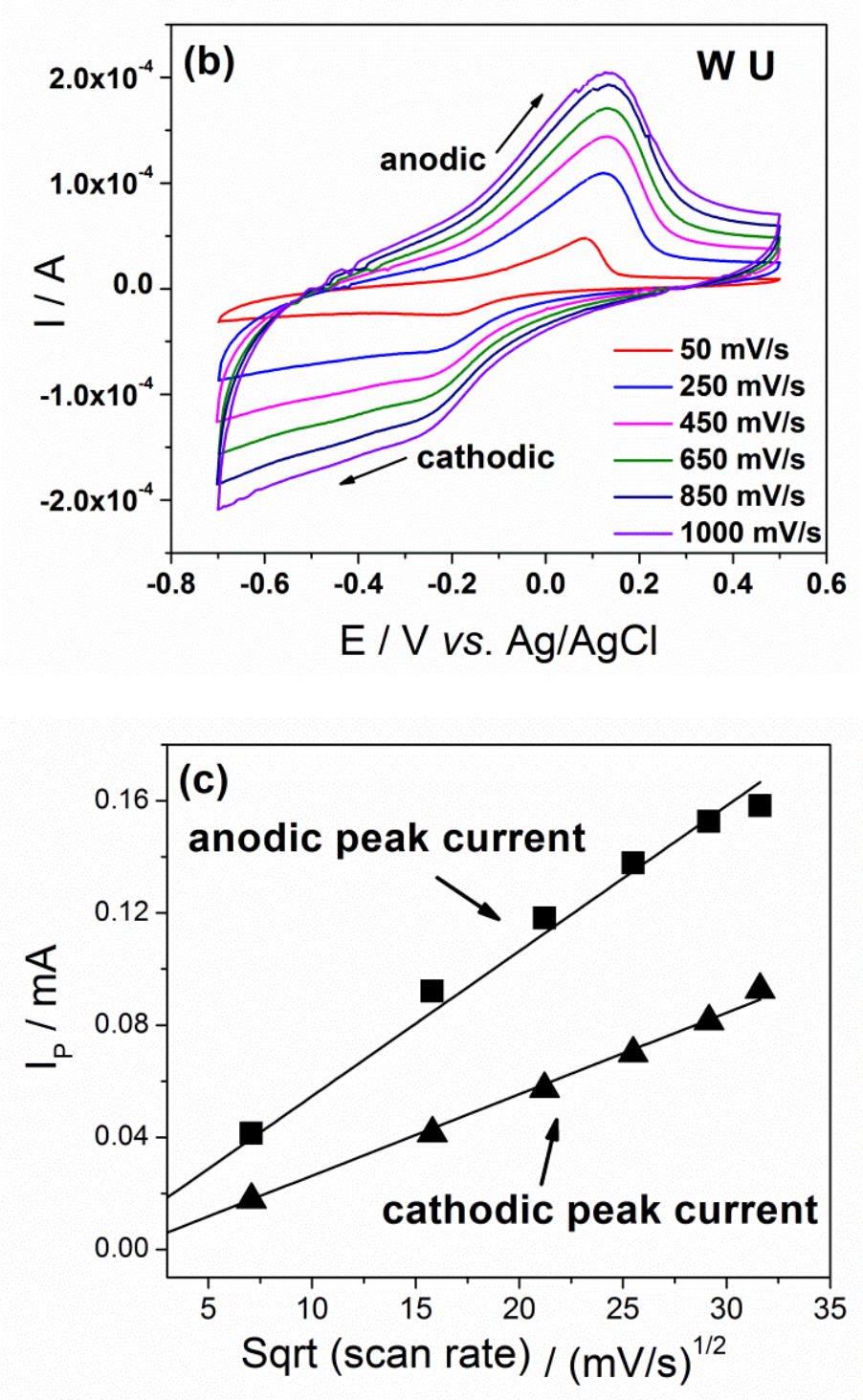

Figure 3.1. Cyclic voltammograms of magnetite electrode scanned from 50 mV/s to 1000 mV/s (a) in the background electrolyte containing 0.1 M NaCl (without U) and (b) in 1 mM UO_2^{2+} (with U), both solutions are in pH = 3.4. The arrows in (a) and (b) show the scan directions. (c) The linear relation between the cathodic and the anodic peak current values and the square root of the scan rates.

Electrochemical-AFM

The changes of the surface morphology, reflecting the surface conditions of the magnetite electrode in the cyclic voltammetry experiments, were recorded using *in situ* Electrochemical-AFM as a function of applied potentials. The AFM image of the (111) parting surface of magnetite in air shows an atomically rough (Ra = 1.76 nm) surface. Precipitation-like features were identified on the surface (SI, Figure S3.5), which is likely caused by the oxidation of the surface during electrode fabrication. Precipitation and dissolution phenomena were observed on the surface of magnetite showing a significant dependence on the applied potential (SI, movie link). Four snapshots of the peak force error images at 0.11 V (initial equilibrium potential), -0.45 V (cathodic scan, when a sharp increase in the amount of precipitates was found in the images), -0.7 V (cathodic scan end potential), and 0.5 V (anodic scan end potential) are shown (Figure 3.2a). Distinct precipitation was identified at potentials below -0.45 V (Figure 3.2a, b). The precipitates found at the most negative potential of -0.7 V have diameters ranging from 101 to 868 nm (mean of 208 nm), with an average height of 28 nm and an average nuclei population density (number of islands per area) of 3.4 μm^{-2}. The growth/dissolution rates of the precipitates in the cathodic/anodic scans were estimated by comparing the depth profiles on the height sensor images (measuring height changes across the dashed line positioned in Figure 3.2a, -0.7 V image). The growth rate was 7.8 nm/min at -0.45 V and the fastest growth rate was 42 nm/min at -0.6 V. The dissolution rate adopted a relative stable value around 20 nm/min from 0.1 V to 0.5 V in the anodic scan. Similarly, by comparing the morphology change (counting the number of precipitates) on the peak force error images, the nuclei population density of the precipitates was plotted as a function of potential (Figure 3.2c). The nuclei population density shows a sharp increase starting from -0.45 V and reaching a maximum of 2.28 μm^{-2} at -0.6 V

during the reverse anodic scan. For the rest of the anodic scan, nuclei population density fluctuates around 1.3 μm^{-2}. The precipitation at negative potentials explains the increased charge density with the decrease of the scan rate found in Figure S3.3b. Decreasing the scan rate provides increasing time to accumulate more uranium species on the surface of the magnetite electrode, resulting in an increase in the amount of charges transferred at low scan rates. Various spectroscopic methods (XPS, AES, XAS) were used to characterize the nature of the uranium precipitates found in the EC-AFM experiments.

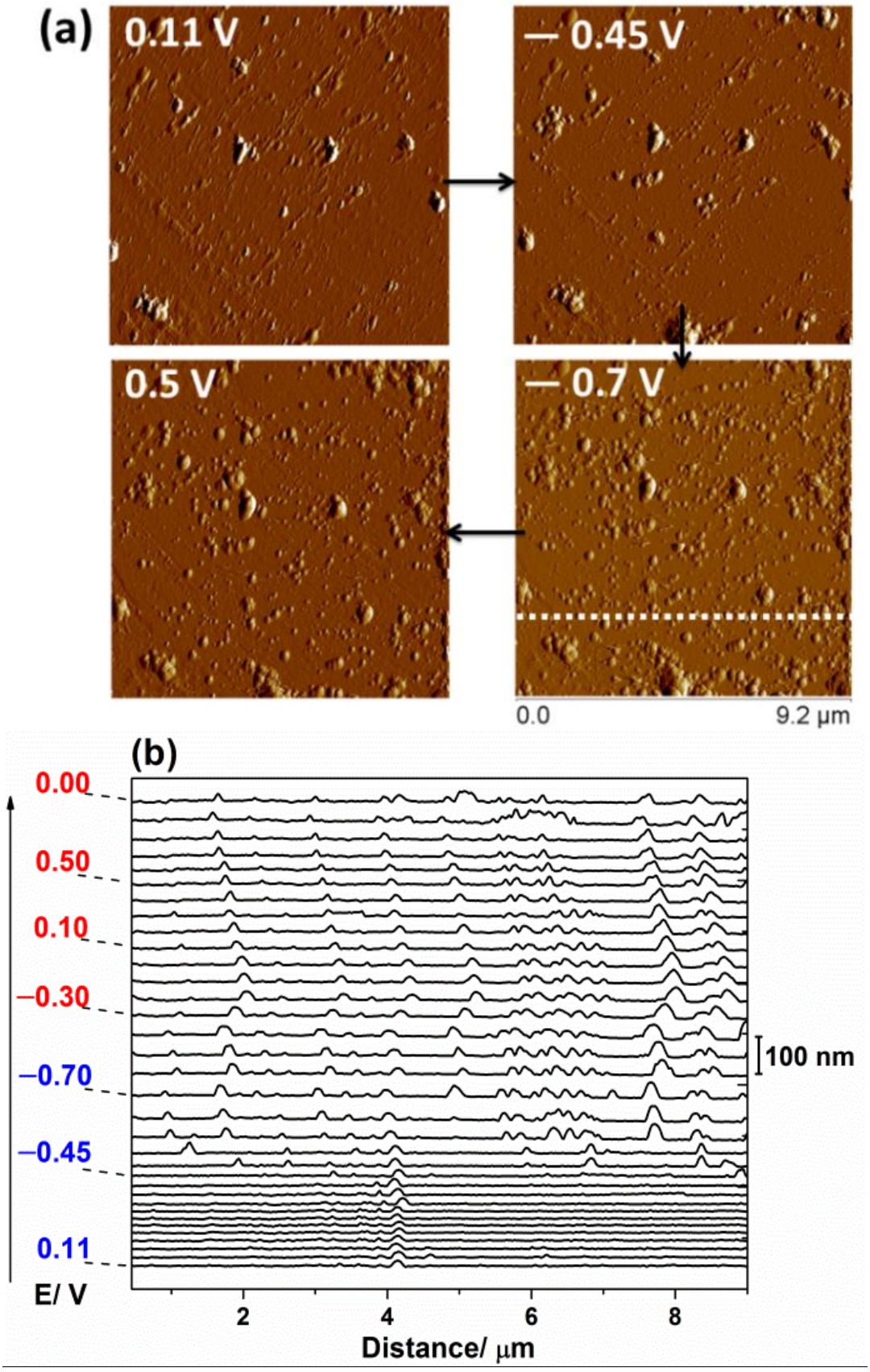
(a)
0.11 V
— 0.45 V
0.5 V
— 0.7 V
0.0
9.2 µm
(b)
0.00
0.50
0.10
–0.30
–0.70
–0.45
0.11
E/ V
100 nm
2
4
6
8
Distance/ µm

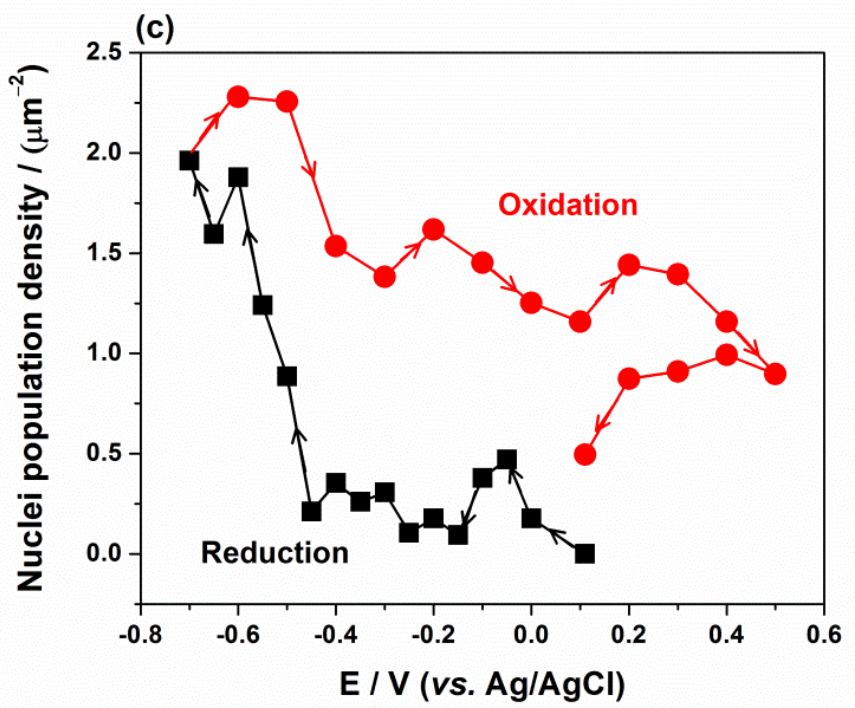

Figure 3.2. (a) Peak force error images (9.2 μm × 9.2 μm) of the surfaces of the magnetite electrode at 0.11 V, -0.45 V, -0.7 V, and 0.5 V in 0.5 mM UO_2^{2+} with 0.1 M NaCl as the background electrolyte at pH = 3.4. (b) Depth profiles across the white dotted line in Figure 2a at all potentials. (c) Nuclei population density of the uranium precipitates as a function of voltage. The arrows indicate the scan direction. The nuclei population density at the initial equilibrium potential (0.11 V) was used as the zero baseline.

U 4f XPS spectra

XPS is a standard method to characterize the oxidation states of uranium[34-37]. The position of the satellite peaks on the high binding-energy side of the U 4f primary peaks is the key criterion to distinguish the oxidation states of uranium from 6+, 5+, and 4+[38]. The peak separation is ≈ 6-7 eV between the U^{4+} primary peak and its associated satellite peaks, and is ≈7.8-8.5 eV for U^{5+}. For U^{6+}, there are two associated satellite peaks of 4 eV and 10 eV away from the primary peaks[38]. As the deposition voltage decreases from -0.1 V to -0.9 V, both the U $4f_{5/2}$ and U $4f_{7/2}$ peaks broaden (Figure 3.3a). The increasing intensity of a shoulder on the lower binding energy side of the primary peaks suggests increasing amounts of reduced uranium. The spectra show two sets of satellite peaks corresponding to U^{6+} and U^{5+} but no evidence for U^{4+} (Figure 3.3b and

SI, Figure S3.6, Table S3.2), which confirms the interpretation of the cyclic voltammogram experiments (Figure 3.1a, b). Fitting the U 4f region yields the proportion of U^{5+} and U^{6+} (Figures 3.3b and Figure S3.7), increasing from 0.2 to 1 as a function of the voltage up to -0.7 V and then decreasing to 0.8 from -0.7 to -0.9 V. The decreased U^{5+}/U^{6+} ratio at -0.9 V is still not fully understood, but it is possible that hydrogen evolution at -0.9 V could cause a high local pH close to the electrode surface (increase in $[OH]^-$), leading to the precipitation of U(VI) phases. Still, even at -0.7 V (U^{5+}/U^{6+} = 1) the average oxidation sate of U is the equivalent of $UO_{2.75}$, which is more oxidized than U_3O_8 or $UO_{2.67}$. In addition, the changes of Fe $2p_{1/2}$ and Fe $2p_{3/2}$ primary and satellite peaks indicate the reduction of surface Fe with decreasing voltage (SI, Figure S3.8).

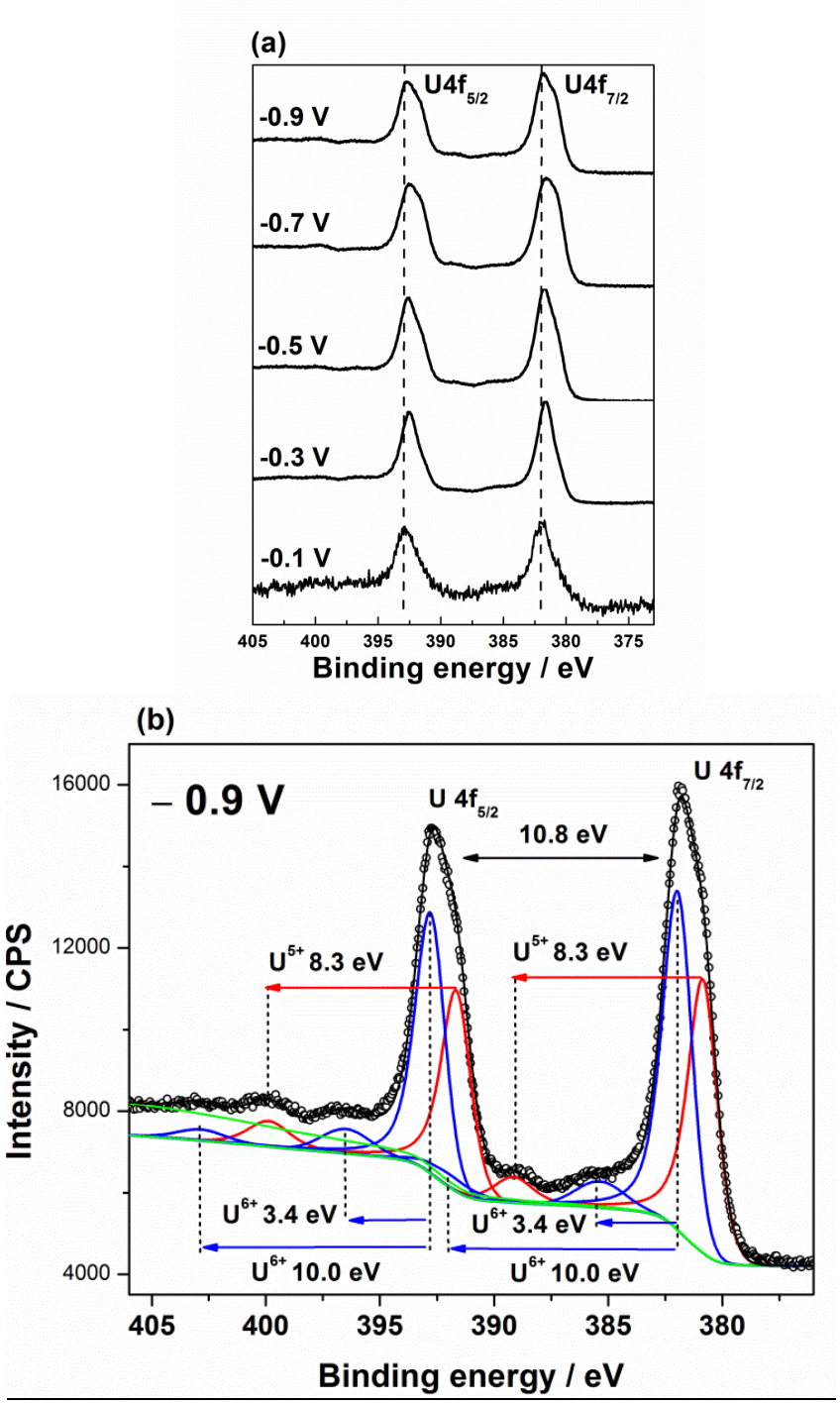

Figure 3.3. (a) XPS spectra of U 4f as a function of voltage. The dashed line marks the peak position of the U $4f_{5/2}$ and U $4f_{7/2}$ on the spectrum at -0.1 V. (b) Fitting results of the U^{5+} and U^{6+} components in the sample prepared at -0.9 V. Data are in open circles; the fitted spectrum is in solid black line; U^{6+} related peaks (primary and satellite) are in blue and U^{5+} are in red lines. The arrows indicate the separation between the U $4f_{5/2}$ and U $4f_{7/2}$ primary peaks (10.8 eV) and the distances between the U^{6+} (3.4 eV and 10.0 eV) and U^{5+} (8.3 eV) primary peaks to the corresponding satellite peaks.

AES

The zoomed-in area (60~120 eV, Figure 3.4b) of the AES spectra (Figure 3.4a) show peaks corresponding to different uranium Auger transitions which have also been identified on uranium metal, UO_2, UF_4, and U_3O_8[39-43]. The U (O_5P_3V) Auger transitions of the samples prepared at different voltages exhibit a constant peak position of ≈77.8 eV (Figure 3.4b, SI, Table S3.3). The U (O_3O_4V) and U (O_5VV) peaks shift slightly (within 1 eV) to high kinetic energies with decreasing potentials. In contrast, the U (O_3O_5V) and U ($O_3P_1P_1$) transitions observed at 101.3 eV and 112.3 eV in the -0.1 V sample shift to low kinetic energies (98.8 eV and 110.6 eV, respectively) at -0.9 V (Figure 3.4b, Table S3.3). The Auger process involves three electrons, and the relaxation of the core holes, core electrons, and the valence electrons can alter the energy levels that are involved in the Auger transitions, resulting in the observed dependence of the peak shifts on the type of Auger transition[44]. In addition, the peaks belonging to the U (O_5VV) transition decrease in intensity with decreasing voltage (Figure 3.4b); two types of AES transitions of U (NOO) at ~189 eV and U (NOV) at ~283 eV have relatively weak intensities and peak overlap issues with the carbon peak (SI, Figure S3.9). The atomic U:O ratio of 1:8.67 was calculated from the AES spectrum of the -0.9 V sample, in which no evidence of Fe Auger peaks was found (See SI for the calculation method). The high oxygen ratio indicates that hydroxyl groups and structural water are likely to be present in the uranium precipitates as found in the EC-AFM. The observed peak shifts along with the above XPS data suggest a series of systematic changes in the uranium Auger peaks upon reduction. However the AES spectra alone cannot provide independent information on the oxidation states of uranium.

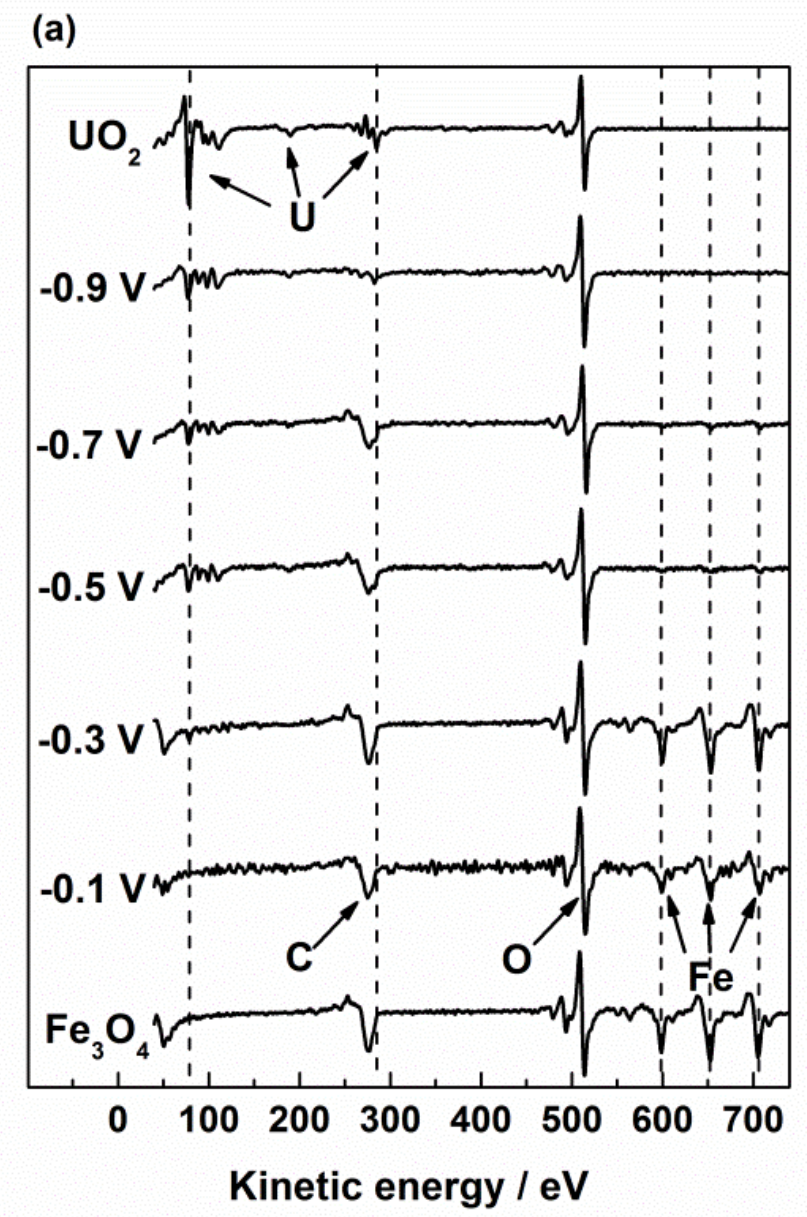
(a)
UO2
U
-0.9 V
-0.7 V
-0.5 V
-0.3 V
-0.1 V
C
O
Fe
Fe3O4
0
100
200
300
400
500
600
700
Kinetic energy / eV

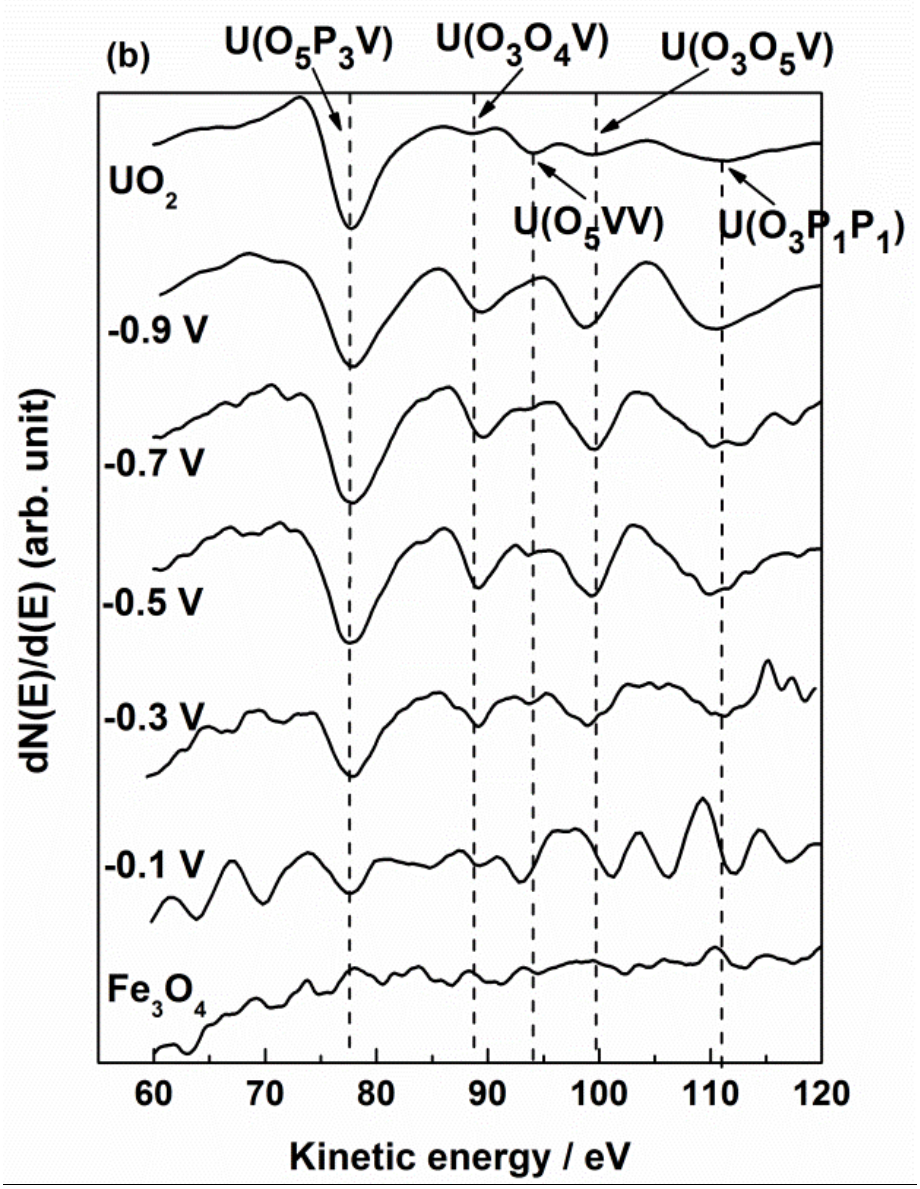

Figure 3.4. (a) Derivative AES spectra of the uranium deposited magnetite electrodes prepared at different voltages in comparison with Fe_3O_4 and UO_2 standards. (b) Zoomed-in area of (a) from 60~120 eV show the assignments of the Auger peaks related to five types of uranium Auger transitions. The three letters represent energy levels of the three electrons involved in the Auger transition.

U L_3 edge XANES and EXAFS

XANES and EXAFS can provide information on the oxidation states and local structures of actinyl ions[45-53]. The edge positions (the inflection points) were taken as the photon energies at the highest peak values of the first derivative of the primary XANES spectra. The U L_3 edges shift to low energy with the decreasing voltage (Figure 3.5; SI, Figure S3.10 and S3.11). An energy difference of 0.8 eV is found between the edge positions of the samples prepared at -0.1 V (17171.8 eV) and -0.9 V (17171.0 eV), suggesting the reduction of U(VI). The 0.8 eV shift is consistent with the small edge-energy differences (0~1 eV) found between U(V) and U(VI) bearing compounds[54, 55] and complexes[51]. XANES fitting results indicate that the sample prepared at -0.7 V, which has the highest concentration of U^{5+} determined by XPS, has the largest shifts to low energies of the fitted peak positions (SI, Figure S3.12 and Table S3.4). In the absence of appropriate U(V) standards for XANES, linear combination fits using the XANES of schoepite and UO_2 were used as the oxidation state end members of U(VI) and U(IV), respectively. No combination fits provide adequate modeling of the experimental data. This indirectly supports the XPS and electrochemical evidence that the reduced species is U(V). Furthermore, because the resonance feature ~15 eV above the white line (SI, Figure S3.10), that is typical of uranyl coordination[56], persists for all the samples, it is likely that both U(V) and U(VI) are present as uranyl moieties in the precipitates.

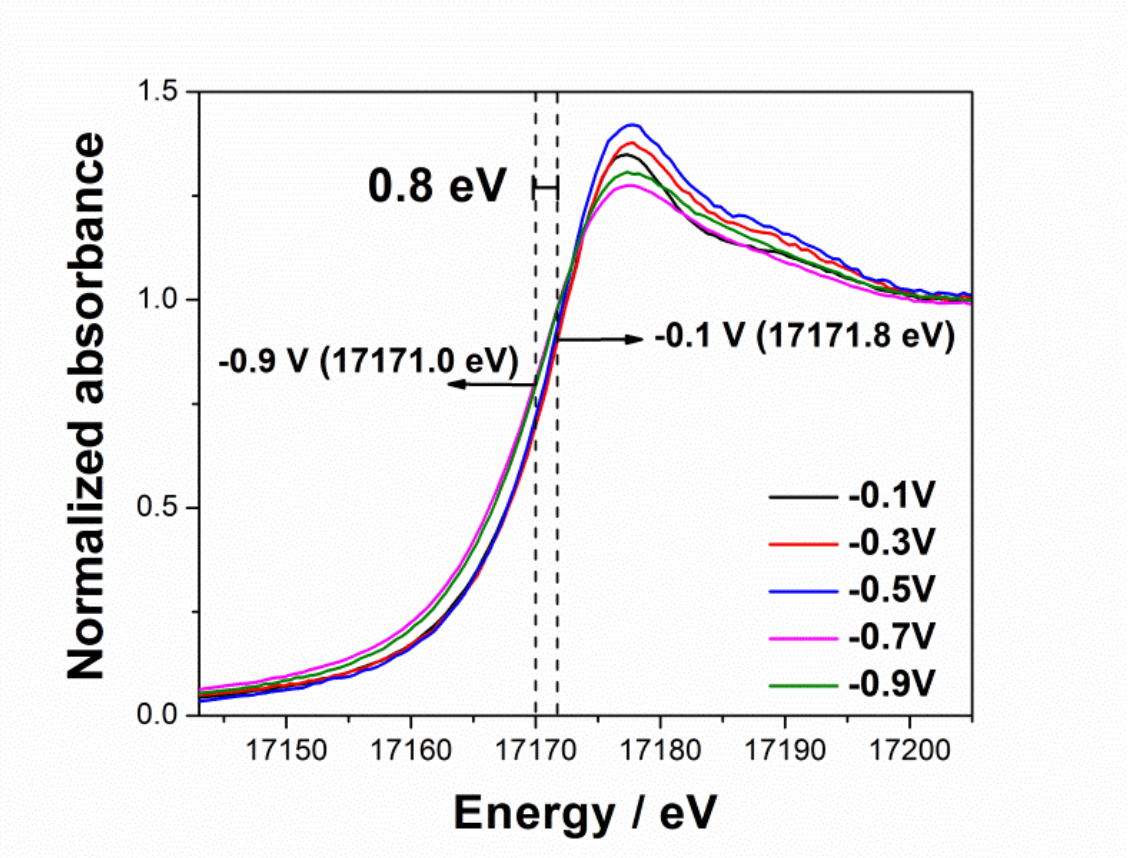

Figure 3.5. U L_3-edge XANES of the uranium deposited magnetite electrodes prepared in 1mM UO_2^{2+} solutions at decreasing potentials from -0.1 V to -0.9 V. The dashed lines mark the edge positions of the sample prepared at -0.1 V (17171.8 eV) and -0.9 V (17171.0 eV).

The U $k^2\chi(k)$ EXAFS data and the magnitudes of the Fourier transform (FT) data are shown in Figs. 3.6a and b, respectively. For the sample prepared at -0.1 V, two characteristic peaks at 1.84 Å and 2.55 Å (phase-shift corrected) correspond to the axial and equatorial U-O bonds (Figure 3.6b) as identified in numerous UO_2^{2+} absorbed mineral samples[12, 57-59]. The spectra fitting results indicate two types of U-O_{eq} bonds in the -0.1 V sample (Table 3.1). U coordinates with five equatorial O atoms, in which two U-$O_{eq}1$ bond lengths are shorter than the other three U-O_{eq2} bonds. This model (including axial O and two types of U-O_{eq}) is applicable to the samples prepared at all potentials (Table 3.1, See SI for fitting details). Due to the increasing noise at high

k-values, features beyond ~3.5 Å in the FT plots are of little significance and were not considered in the fitting. In addition, the -0.7 V sample can also be fitted using one type of U-O_{eq} distance (SI, Table S 3.5). Higher quality data may be needed to accurately fit the equatorial oxygen shells in this sample. The positions and shapes of the peaks in the FT plots exhibit variations with decreasing voltage, indicating changes in the U coordination environments upon reduction (Figure 3.6b). The longest average U-O_{ax} bond length was found to be 2.05 ± 0.01 Å in the sample prepared at -0.7 V, which also has the highest ratio of U^{5+}/U^{6+} determined from the XPS analysis. For comparison, the axial U(V)-O distance for an aqueous $[UO_2(CO_3)_3]^{5-}$ species was determined by EXAFS to be 1.9 ± 0.02 Å [60]. Similarly, the largest bond lengths for U-O_{eq1} and U-O_{eq2} were also found in the -0.7 V sample (Table 3.1). The large Debye-Waller factors associated with the -0.7 V sample indicate a high degree of disorder of the uranium precipitates, which is likely caused by the high amount of structural water suggested by the AES analysis. These poorly-crystallized strongly-hydrated precipitates also explain the absence of the U–U pair correlations in the FT data. The U-O bond length information was plotted against the potential (Figure S3.13). Comparing Figure S3.13 (bond lengths) with Figure S3.7 (XPS results), reveals similar trends. Namely, the distances of U to its neighboring O atoms increase with the corresponding increase of the U^{5+} concentration. Most importantly, both indicators (bond lengths and U^{5+}/U^{6+} ratios) exhibit a peak at the same potential of -0.7 V. This trend indicates that the results acquired from EXAFS and XPS are consistent.

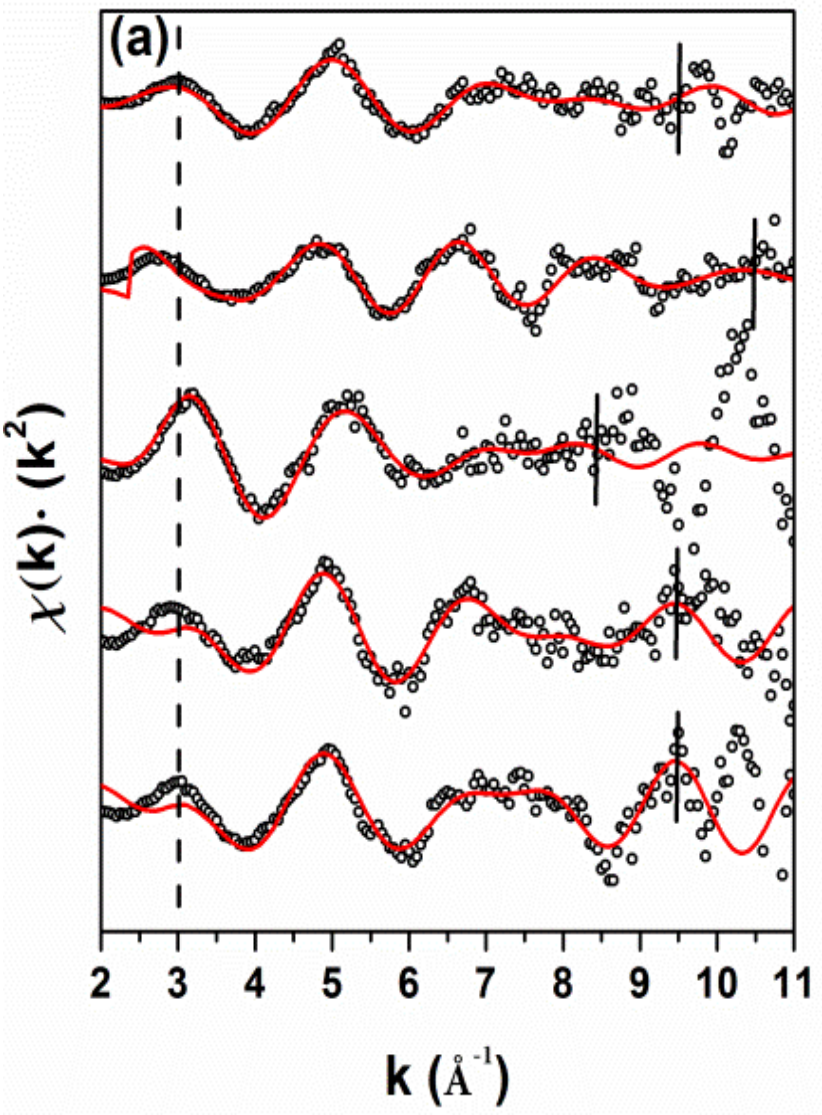
(a)
χ(k)· (k²)
2
3
4
5
6
7
8
9
10
11
k (Å⁻¹)

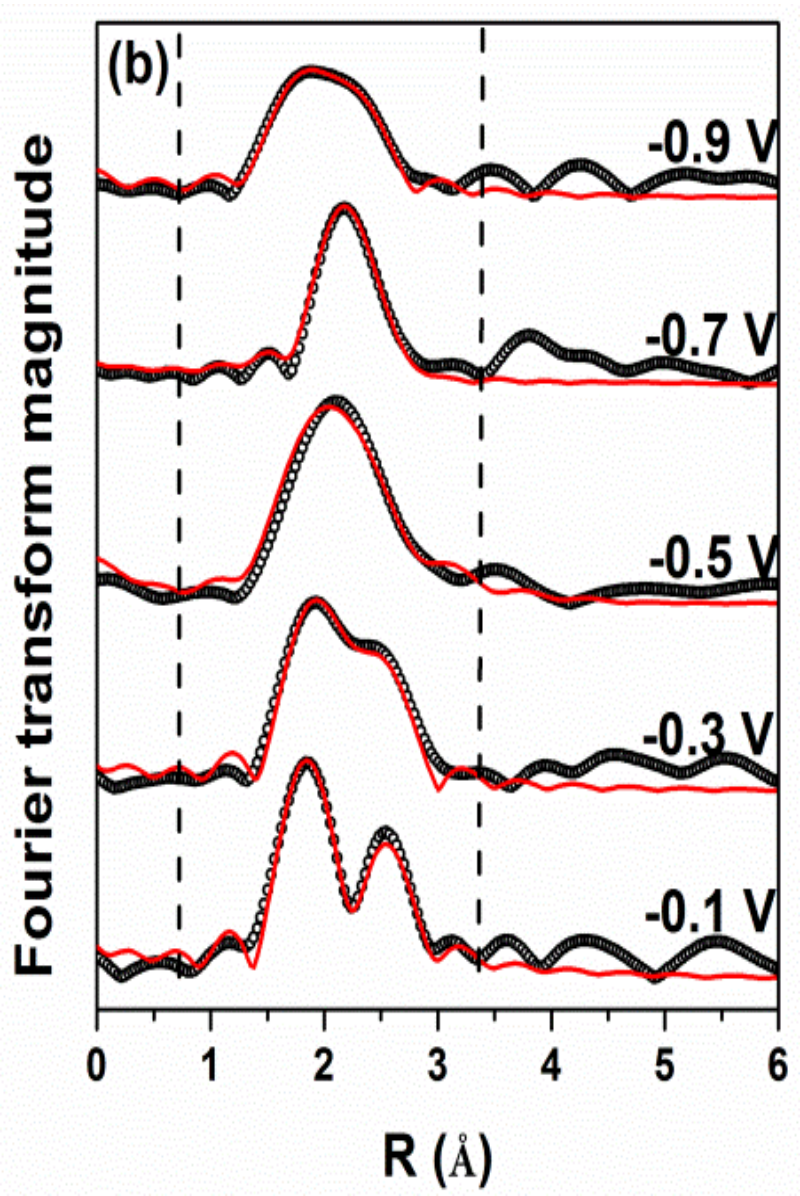

Figure 3.6. (a) U L_3 edge $k^2\chi(k)$ and (b) their Fourier transformed magnitude (phase corrected) of the uranium samples prepared under different potentials on the magnetite electrodes. Experimental data and theoretical fitting are shown in black circle and solid line. The dashed lines and the short solid lines in (a) indicate the region where the data were truncated to obtain the FT magnitude in (b). The dashed lines in (b) indicate the regions where the data were used for the spectra fitting.

Table 3.1 Best-fit values of the U L_3-edge EXAFS spectra for the uranium deposited magnetite electrodes prepared at different voltages. The U^{5+}/U^{6+} ratios obtained from XPS.

Sample	Path	**CN**	R / Å	σ^2 / $Å^2$	ΔE_0 / eV	S_0^2	χ_v^2	U^{5+}/U^{6+}
-0.1 V	U-Oax	2	1.86 ± 0.02	0.0020	5.6	1.00	32.04	0.22
	U-Oeq1	2.1	2.21 ± 0.02	0.0010				
	U-Oeq2	3.2	2.47 ± 0.01	0.0036				
-0.3 V	U-Oax	2	1.89 ± 0.02	0.0020	8.3	0.95	18.27	0.21
	U-Oeq1	1.9	2.21 ± 0.04	0.0096				
	U-Oeq2	3.3	2.46 ± 0.03	0.0023				
-0.5 V	U-Oax	2	1.80 ± 0.01	0.0103	9.0	0.95	18.33	0.59
	U-Oeq1	2.4	2.47 ± 0.03	0.0101				
	U-Oeq2	3.4	2.75 ± 0.01	0.0086				
-0.7 V	U-Oax	2	2.05 ± 0.01	0.0046	9.8	0.95	14.39	1.0
	U-Oeq1	2.3	2.51 ± 0.01	0.0093				
	U-Oeq2	3.0	2.88 ± 0.08	0.0561				
-0.9 V	U-Oax	2	1.80 ± 0.02	0.0091	6.6	0.95	26.37	0.82
	U-Oeq1	2.0	2.16 ± 0.02	0.0117				
	U-Oeq2	3.0	2.36 ± 0.05	0.0035				

Uranyl(V) precipitates stabilized on magnetite electrodes

Previous computational and experimental studies have shown that the two-electron reduction of UO_2^{2+} to U^{4+} is thermodynamically favorable[7, 10, 15, 61]. Yet, the sample prepared at -0.9 V shows no evidence of U^{4+}, indicating the high kinetic barrier for the two-electron reduction. Thus, any U^{4+} is likely to be eventually generated through the disproportionation of UO_2^{+} rather than through direct reduction from UO_2^{2+} to U^{4+}. In fact, inspection of the Latimer diagram for uranium in acidic electrolytes reveals that the disproportionation of UO_2^{+} is a thermodynamically favorable process[62]. The electrochemically reduced uranium species were formed minutes after the reaction and the short time scale could have preserved the purportedly metastable UO_2^{+}, whereas studies by Scott et al.[7] reduced UO_2^{2+} on magnetite for a longer time scale (12-168 h) in less acidic conditions and did document the formation of U^{4+}. Alternatively, UO_2^{+} might have been stabilized through precipitation of the mixed-valence U(V)/U(VI) solids on magnetite as seen in a previous study by Skomurski et al.[15] under less acidic conditions. Note that the formation of UO_2^{2+}-UO_2^{+} ion pairs in solution has been documented to slow disproportionation of UO_2^{+}[63]. The magnetite electrode surface, similar to a mercury electrode used for uranium electroanalytical chemistry, stabilizes UO_2^{+}, which is otherwise prone to disproportionation—a mechanism which is not fully understood despite decades of research. The results obtained here suggest that precipitation of a mixed U(V)/U(VI) phase at acidic conditions (pH = 3.4) could be the reason that U(V) persists. However, the ultimate stability and structure (likely amorphous or low crystallinity) of the U(V)/U(VI) precipitates prepared in current experiments are still an open question. It may be important to consider the formation of the U(V)-containing phases as a complementary pathway in future immobilization studies. However, the long-term stability of

these phases due to oxidation is likely to be different from the commonly-observed sink phase, UO_2.

Acknowledgements

The bulk of this work is supported by the U.S. Office of Science, Basic Energy Sciences, Grant #DE-FG02-06ER15783 and by Turner Grant and Rackham Graduate Student Research Grant from the University of Michigan. XPS interpretation performed by E.S.I. was supported by the Geosciences Research Program at PNNL sponsored by the U.S. Department of Energy (DOE), Office of Basic Energy Sciences (BES), Division of Chemical Sciences, Geosciences & Biosciences. Pacific Northwest National Laboratory (PNNL) is a multiprogram national laboratory operated for DOE by Battelle. The authors acknowledge the assistance from the beamline scientists Benjamin Reinhart and Sungsik Lee at 12-BM-B, APS. The work at Argonne National Laboratory—including the use of the Advanced Photon Source, an Office of Science User Facility operated for the U.S. Department of Energy (DOE) Office of Science by Argonne National Laboratory—was supported by the U.S. DOE under Contract No. DE-AC02-06CH11357. The authors acknowledge valuable comments made by David Shoesmith (Department of Chemistry, University of Western Ontario) and Mark Meyerhoff (Department of Chemistry, University of Michigan).

References

1. Cui, D. Q.; Spahiu, K. The reduction of U(VI) on corroded iron under anoxic conditions. *Radiochim Acta* **2002,** *90*, 623-628.

2. Dodge, C. J.; Francis, A. J.; Gillow, J. B.; Halada, G. P.; Eng, C.; Clayton, C. R. Association of uranium with iron oxides typically formed on corroding steel surfaces. *Environ. Sci. Technol.* **2002,** *36*, 3504-3511.

3. Gu, B.; Liang, L.; Dickey, M. J.; Yin, X.; Dai, S. Reductive precipitation of uranium(VI) by zero-valent iron. *Environ. Sci. Technol.* **1998,** *32*, 3366-3373.

4. Latta, D. E.; Gorski, C. A.; Boyanov, M. I.; O'Loughlin, E. J.; Kemner, K. M.; Scherer, M. M. Influence of magnetite stoichiometry on U(VI) reduction. *Environ. Sci. Technol.***2012,** *46*, 778-786.

5. Lovley, D. R.; Phillips, E. J. P.; Gorby, Y. A.; Landa, E. R. Microbial reduction of uranium. *Nature* **1991,** *350*, 413-416.

6. Missana, T.; Maffiotte, U.; Garcia-Gutierrez, M. Surface reactions kinetics between nanocrystalline magnetite and uranyl. *J. Colloid Interface Sci.* **2003,** *261*, 154-160.

7. Scott, T. B.; Allen, G. C.; Heard, P. J.; Randell, M. G. Reduction of U(VI) to U(IV) on the surface of magnetite. *Geochim. Cosmochim. Acta* **2005,** *69*, 5639-5646.

8. Latta, D. E.; Mishra, B.; Cook, R. E.; Kemner, K. M.; Boyanov, M. I. Stable U(IV) complexes form at high-affinity mineral surface sites. *Environ. Sci. Technol.* **2014,** *48*, 1683-1691.

9. Liger, E.; Charlet, L.; Van Cappellen, P. Surface catalysis of uranium(VI) reduction by iron(II). *Geochim. Cosmochim. Acta* **1999,** *63*, 2939-2955.

10. Singer, D. M.; Chatman, S. M.; Ilton, E. S.; Rosso, K. M.; Banfield, J. F.; Waychunas, G. A. Identification of simultaneous U(VI) sorption complexes and U(IV) nanoprecipitates on the magnetite (111) surface. *Environ. Sci. Technol.* **2012,** *46*, 3811-3820.

11. Boland, D. D.; Collins, R. N.; Glover, C. J.; Payne, T. E.; Waite, T. D. Reduction of U(VI) by Fe(II) during the Fe(II)-accelerated transformation of ferrihydrite. *Environ. Sci. Technol.* **2014,** *48*, 9086-9093.

12. Ilton, E. S.; Boily, J. F.; Buck, E. C.; Skomurski, F. N.; Rosso, K. M.; Cahill, C. L.; Bargar, J. R.; Felmy, A. R. Influence of dynamical conditions on the reduction of U(VI) at the magnetite-solution interface. *Environ. Sci. Technol* .**2010,** *44*, 170-176.

13. Ilton, E. S.; Pacheco, J. S. L.; Bargar, J. R.; Shi, Z.; Liu, J.; Kovarik, L.; Engelhard, M. H.; Felmy, A. R. Reduction of U(VI) Incorporated in the Structure of Hematite. *Environ. Sci. Technol.* **2012,** *46*, 9428-9436.

14. Massey, M. S.; Lezama-Pacheco, J. S.; Jones, M. E.; Ilton, E. S.; Cerrato, J. M.; Bargar, J. R.; Fendorf, S. Competing retention pathways of uranium upon reaction with Fe(II). *Geochim. Cosmochim. Acta* **2014,** *142*, 166-185.

15. Skomurski, F. N.; Ilton, E. S.; Engelhard, M. H.; Arey, B. W.; Rosso, K. M. Heterogeneous reduction of U^{6+} by structural Fe^{2+} from theory and experiment. *Geochim. Cosmochim. Acta* **2011,** *75*, 7277-7290.

16. Ilton, E. S.; Haiduc, A.; Cahill, C. L.; Felmy, A. R. Mica surfaces stabilize pentavalent uranium. *Inorg. Chem.* **2005,** *44*, 2986-2988.

17. Renshaw, J. C.; Butchins, L. J. C.; Livens, F. R.; May, I.; Charnock, J. M.; Lloyd, J. R. Bioreduction of uranium: Environmental implications of a pentavalent intermediate. *Environ. Sci. Technol.***2005,** *39*, 5657-5660.

18. Herasymenko, P. Electroreduction of uranyl salts by means of the mercury dropping cathode. *T. Faraday. Soc.* **1928,** *24*, 0272-0278.

19. Harris, W. E.; Kolthoff, I. M. The polarography of uranium.1. Reduction in moderately acid solutions-polarographic determination of uranium *J. Am. Chem. Soc.* **1945,** *67*, 1484-1490.

20. Harris, W. E.; Kolthoff, I. M. The polarography of uranium. 3. Polargoraphy in very weakly acid, neutral or basic solution. *J. Am. Chem. Soc.* **1947,** *69*, 446-451.

21. Kern, D. M. H.; Orlemann, E. F. The potential of the uranium(V), uranium(VI) couple and the kinetics of uranium(V) disproportionation in perchlorate media. *J. Am. Chem. Soc.* **1949,** *71*, 2102-2106.

22. Kolthoff, I. M.; Harris, W. E. The polarography of uranium. 2. Polarography in strongly acid solution. *J. Am. Chem. Soc.* **1946,** *68*, 1175-1179.

23. Morris, D. E. Redox energetics and kinetics of uranyl coordination complexes in aqueous solution. *Inorg. Chem.* **2002,** *41*, 3542-3547.

24. Renock, D.; Mueller, M.; Yuan, K.; Ewing, R. C.; Becker, U. The energetics and kinetics of uranyl reduction on pyrite, hematite, and magnetite surfaces: A powder microelectrode study. *Geochim. Cosmochim. Acta.* **2013,** *118*, 56-71.

25. Yuan, K., Renock, D., Ewing, R. C., Becker, U. Uranium reduction on magnetite: Probing for pentavalent uranium using electrochemical methods. *Geochim. Cosmochim. Acta.* **2015,** 156: 194-206

26. Smart, N. R.; Rance, A. P. *Effect of radiation on anaerobic corrosion of iron*; Svensk kärnbränslehantering AB, Swedish Nuclear Fuel and Waste Management Co.,: Stockholm, Sweden, 2005; pp 3-30.

27. EI Aamrani, F.; Casas, I.; de Pablo, J.; Duro, L.; Grivè, M.; J., B. *Experimental and modeling study of the interaction between Uranium (VI) and magnetite*; Svensk kärnbränslehantering AB, Swedish Nuclear Fuel and Waste Management Co.,: Stockholm, Sweden, 1999; pp 4-27.

28. Singer, D. M.; Chatman, S. M.; Ilton, E. S.; Rosso, K. M.; Banfield, J. F.; Waychunas, G. A. U(VI) sorption and reduction kinetics on the magnetite (111) surface. *Environ. Sci. Technol.***2012,** *46*, 3821-3830.

29. Ravel, B.; Newville, M. ATHENA, ARTEMIS, HEPHAESTUS: data analysis for X-ray absorption spectroscopy using IFEFFIT. *J. Synchrotron. Radiat.* **2005,** *12*, 537-541.

30. Rehr, J. J.; Albers, R. C. Theoretical approaches to X-ray absorption fine structure. *Rev. Mod. Phys.* **2000,** *72*, 621-654.

31. Wang, S. Y.; Ho, K. C.; Kuo, S. L.; Wu, N. L. Investigation on capacitance mechanisms of Fe_3O_4 electrochemical capacitors. *J. Electrochem. Soc.* **2006,** *153*, A75-A80.

32. Wu, N. L.; Wang, S. Y.; Han, C. Y.; Wu, D. S.; Shiue, L. R. Electrochemical capacitor of magnetite in aqueous electrolytes. *J. Power Sources* **2003,** *113*, 173-178.

33. Bard, A. J.; Faulkner, L. R., *Electrochemical methods: fundamentals and applications*. Second edition ed.; John Wiley & Sons, Inc.: Hoboken, 2001.

34. Razdan, M.; Hall, D. S.; Keech, P. G.; Shoesmith, D. W. Electrochemical reduction of hydrogen peroxide on SIMFUEL (UO_2) in acidic pH conditions. *Electrochim. Acta* **2012,** *83*, 410-419.

35. Sunder, S.; Shoesmith, D. W.; Bailey, M. G.; Stanchell, F. W.; McIntyre, N. S. Anodic oxidation of UO_2. 1. Electrochemical and X-ray photoelectron spectroscopic studies in neutral solutions. *J. Electroanal. Chem.* **1981,** *130*, 163-179.

36. Bi, Y.; Hayes, K. F.; Surface Passivation Limited UO_2 Oxidative Dissolution in the Presence of FeS. *Environ. Sci. Technol.* **2014**, 48, 13402-13411.

37. Schindler, M.; Hawthorne, F. C.; Freund, M. S.; Burns, P. C.; XPS spectra of uranyl minerals and synthetic uranyl compounds. I: The U 4f spectrum. *Geochim. Cosmochim. Acta*. **2009**, 73, 2471-2487.

38. Ilton, E. S.; Bagus, P. S. XPS determination of uranium oxidation states. *Surf. Interface Anal.* **2011,** *43*, 1549-1560.

39. Allen, G. C.; Wild, R. K. Chemical shifts in uranium Auger transitions. *Chem. Phys. Lett.* **1972,** *15*, 279-281.

40. Allen, G. C.; Wild, R. K. Auger spectroscopy of uranium. *J.Chem.Soc.Dalton.***1974**, 493-498.

41. Ellis, W. P. Auger/loss studies of uranium, uranium oxidation, UO_2, U_3O_8 and UF_4 *Surf. Sci.* **1976,** *61*, 37-59.

42. Holliday, K. S.; Siekhaus, W.; Nelson, A. J. Measurement of the Auger parameter and Wagner plot for uranium compounds. *J. Vac. Sci. Technol. A* **2013,** *31*.

43. Younes, C. M.; Allen, G. C.; Embong, Z. Auger electron spectroscopic study of the surface oxidation of uranium-niobium alloy {U-6 wt.% Nb} in a UHV environment containing primarily H_2, H_2O and CO. *Surf. Sci.* **2007,** *601*, 3207-3214.

44. Allen, G. C.; Wild, R. K. Chemical shifts in uranium Auger transitions. *Chem. Phys. Lett.* **1972,** *15*, 279-281.

45. Antonio, M. R.; Chiang, M. H.; Williams, C. W.; Soderholm, L., In situ actinide X-ray absorption spectroelectrochemistry. In *Actinides-Basic Science, Applications and Technology*, Soderholm, L.; Joyce, J. J.; Nicol, M. F.; Shuh, D. K.; Tobin, J. G., Eds. 2004; Vol. 802, pp 157-168.

46. Antonio, M. R.; Soderholm, L., X-ray absorption spectroscopy of the actinides. In *The chemistry of the actinide and transactinide elements* Morss, L. R., Edelstein, N.M., Fuger, J., Ed. Springer: Netherlands, 2006; pp 3086-3198.

47. Antonio, M. R.; Williams, C. W.; Sullivan, J. A.; Skanthakumar, S.; Hu, Y. J.; Soderholm, L. Preparation, stability, and structural characterization of Plutonium(VII) in alkaline aqueous solution. *Inorg. Chem.* **2012,** *51*, 5274-5281.

48. Marshall, T. A.; Morris, K.; Law, G. T. W.; Livens, F. R.; Mosselmans, J. F. W.; Bots, P.; Shaw, S. Incorporation of Uranium into Hematite during Crystallization from Ferrihydrite. *Environ. Sci. Technol.***2014,** *48*, 3724-3731.

49. Singh, A.; Catalano, J. G.; Ulrich, K. U.; Giammar, D. E. Molecular-Scale Structure of Uranium(VI) Immobilized with Goethite and Phosphate. *Environ. Sci. Technol.***2012,** *46*, 6594-6603.

50. Soderholm, L.; Antonio, M. R.; Williams, C.; Wasserman, S. R. XANES spectroelectrochemistry: a new method for determining formal potentials. *Anal. Chem.* **1999,** *71*, 4622-4628.

51. Ikeda, A.; Hennig, C.; Tsushima, S.; Takao, K.; Ikeda, Y.; Scheinost, A. C.; Bernhard, G.; Comparative study of uranyl(VI) and -(V) carbonato complexes in an aqueous solution. *Inorg. Chem*. **2007**, 46, 4212-4219.

52. Wang, Z. M.; Lee, S. W.; Catalano, J. G.; Lezama-Pacheco, J. S.; Bargar, J. R.; Tebo, B. M.; Giammar, D. E. Adsorption of uranium(VI) to manganese oxides: X-ray absorption spectroscopy and surface complexation modeling. *Environ. Sci. Technol.***2013,** *47*, 850-858.

53. Williams, C. W.; Blaudeau, J. P.; Sullivan, J. C.; Antonio, M. R.; Bursten, B.; Soderholm, L. The coordination geometry of Np(VII) in alkaline solution. *J. Am. Chem. Soc.* **2001,** *123*, 4346-4347.

54. Soldatov, A. V.; Lamoen, D.; Konstantinovic, M. J.; Van den Berghe, S.; Scheinost, A. C.; Verwerft, M. Local structure and oxidation state of uranium in some ternary oxides: X-ray absorption analysis. *J. Solid State Chem*. **2007**, 180, 54-61.

55. Farges, F.; Ponader, C. W.; Calas, G.; Brown, G. E.; Structual environments of incompatible elements in silicate glass melt systems 2. U(IV), U(V), and U(VI). *Geochim. Cosmochim. Acta*. **1992**, 56, 4205-4220.

56. Kelly, S. D.; Kemner, K. M.; Fein, J. B.; Fowle, D. A.; Boyanov, M. I.; Bunker, B. A.; Yee, N. X-ray absorption fine structure determination of pH-dependent U-bacterial cell wall interactions. *Geochim. Cosmochim. Acta* **2002,** *66*, 3855-3871.

57. Bargar, J. R.; Reitmeyer, R.; Davis, J. A. Spectroscopic confirmation of uranium(VI) carbonato adsorption complexes on hematite. *Environ. Sci. Technol.***1999,** *33*, 2481-2484.

58. Chisholm-Brause, C.; Conradson, S. D.; Buscher, C. T.; Eller, P. G.; Morris, D. E. Speciation of uranyl sorbed at multiple binding sites on montmorillonite. *Geochim. Cosmochim. Acta* **1994,** *58*, 3625-3631.

59. Moyes, L. N.; Parkman, R. H.; Charnock, J. M.; Vaughan, D. J.; Livens, F. R.; Hughes, C. R.; Braithwaite, A. Uranium uptake from aqueous solution by interaction with goethite, lepidocrocite, muscovite, and mackinawite: An X-ray absorption spectroscopy study. *Environ. Sci. Technol.***2000,** *34*, 1062-1068.

60. Docrat, T. I.; Mosselmans, J. F. W.; Charnock, J. M.; Whiteley, M. W.; Collison, D.; Livens, F. R.; Jones, C.; Edmiston, M. J. X-ray absorption spectroscopy of tricarbonatodioxouranate(V), $UO_2(CO_3)_3^{5-}$, in aqueous solution. *Inorg. Chem.* **1999,** *38*, 1879-1882.

61. O'Loughlin, E. J.; Kelly, S. D.; Cook, R. E.; Csencsits, R.; Kemner, K. M. Reduction of uranium(VI) by mixed iron(II)/iron(III) hydroxide (green rust): Formation of UO_2 nanoparticies. *Environ. Sci. Technol.***2003,** *37*, 721-727.

62. A.J. Bard, R. P., and J. Jordan, *Standard Potentials in Aqueous Solutions*. Marcel Dekker: New York, 1985, PP 650.

63. Newton, T. W.; Baker, F. B. A. Uranium(V)-uranium(VI) complex and its effect on the uranium (V) disproportionation rate. *Inorg. Chem.* **1965,** *4*, 1166-1170.

Appendix B

Supporting Information

Electrochemistry and electrochemical AFM

Fabrication of the magnetite electrode

The magnetite samples from Mineville N.Y. have octahedral parting from which the (111) surface can be obtained. The SEM images on the edges of the Mineville magnetite showed the layered structure with triangular step edges which is a direct indication of the layered growth mechanism of the (111) surface (Figure S3.1). The magnetite electrode used for the cyclic voltammetry were polished down to the thickness of 1.5 mm using 6 μm, 3 μm and 1 μm diamond sand papers, successively. The polishing work was under atmospheric conditions on dry diamond sand papers. The polished magnetite sample was sonicated in deionized water, acetone and ethanol. Cu wire was then connected to one side of the magnetite crystal using silver paste and sealed in epoxy, such that only one side of the polished surface was exposed to the solution for reaction. The same magnetite electrode was used for all the cyclic voltammetry experiments. A fresh surface was obtained each time through polishing and cleaning methods described above immediately before the experiment. The geometric area of the magnetite electrode was 0.13 cm^2.

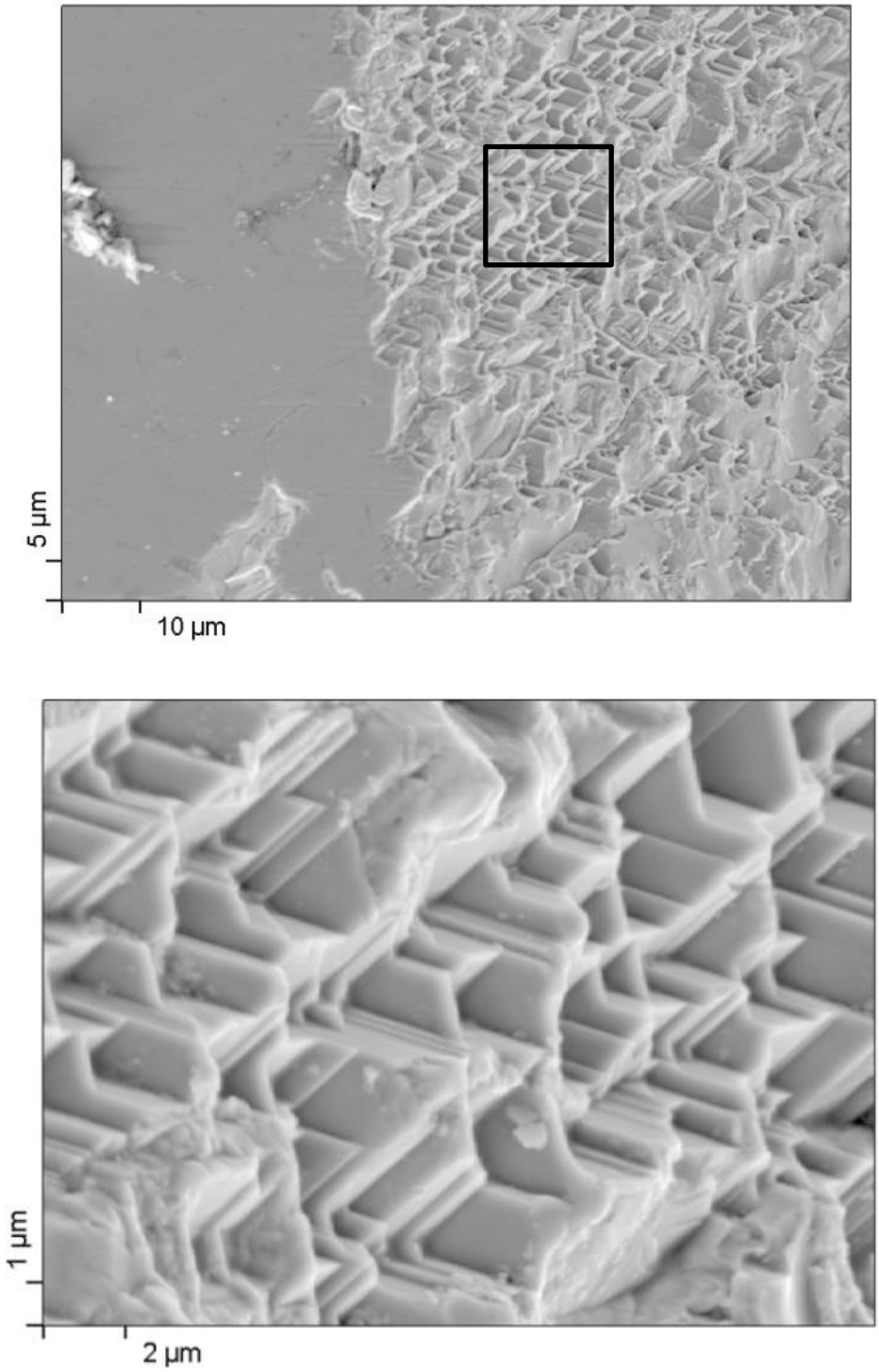

Figure S 3.1 SEM images on the edge of the Mineville, N.Y. magnetite sample used for the fabrication of the magnetite working electrode. The bottom picture shows the zoomed-in area of the square feature of the image on the top.

EC-AFM setup

The magnetite electrode used for the electrochemical-AFM was prepared by the similar method described above, except only one-side of the magnetite surfaces was polished for connection with the metal wire, where the natural parting surface side was preserved and exposed to the uranium solution for reaction. The EC-AFM utilized the electrochemical setup accompanied with the Bruker ScanAsyst AFM. The electrochemical cell is made of a plastic petri dish of the diameter of 50 mm. The magnetite working electrode was mounted in the middle of the cell by epoxy and the reference electrode was inserted from the side and the Pt wire was used as the counter electrode (Figure S3.2). The three electrodes were then connected to the wire connector which was connected to the CHI potentiostat accompanied with the AFM.

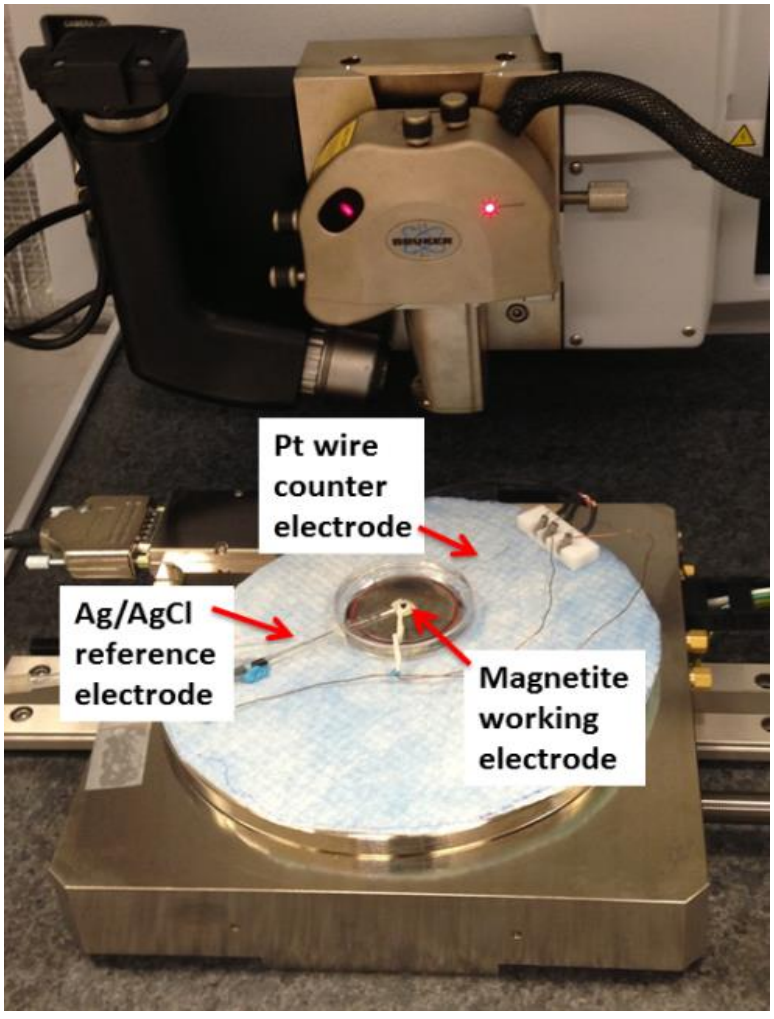

Figure S 3.2 Experimental setup for the electrochemical-AFM experiments.

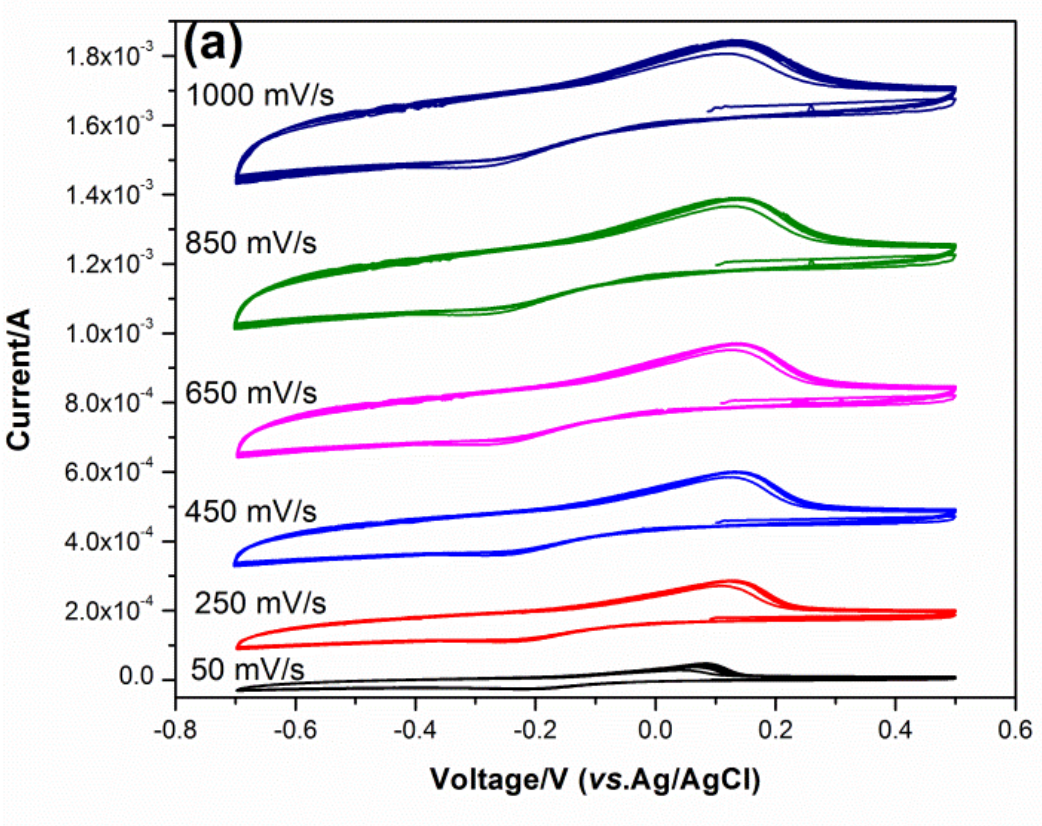
(a)
1000 mV/s
850 mV/s
650 mV/s
450 mV/s
250 mV/s
50 mV/s
Current/A
Voltage/V (vs.Ag/AgCl)

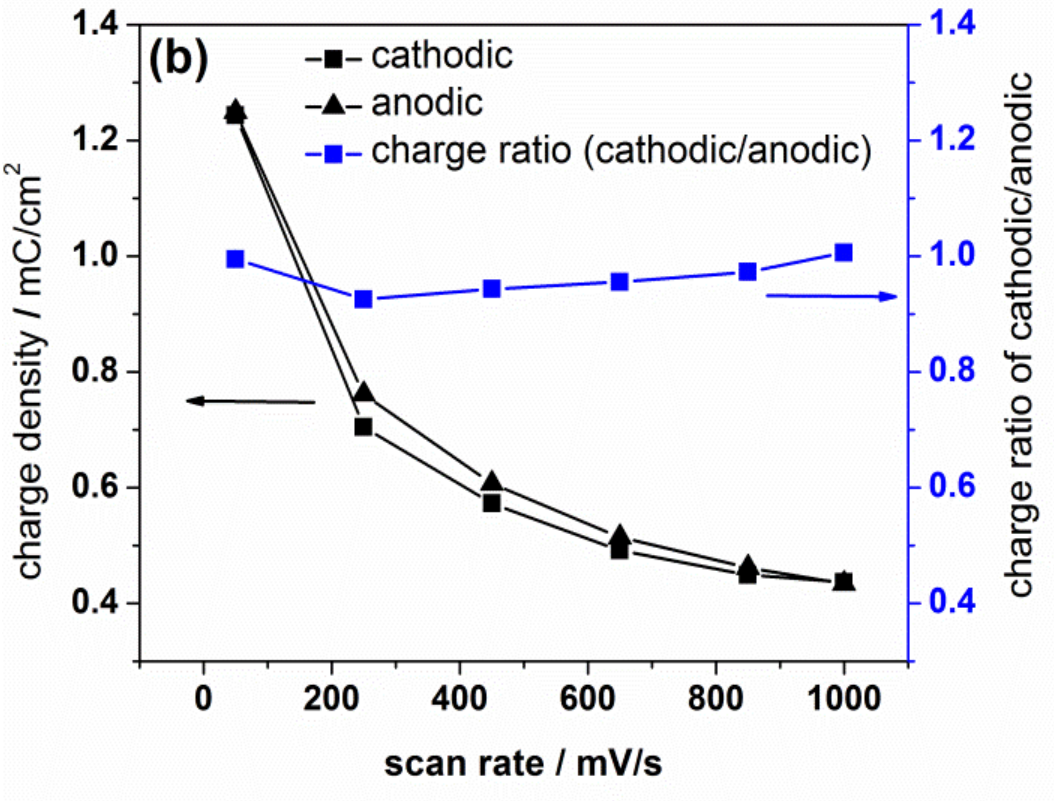
(b)
cathodic
anodic
charge ratio (cathodic/anodic)
charge density / mC/cm2
charge ratio of cathodic/anodic
scan rate / mV/s

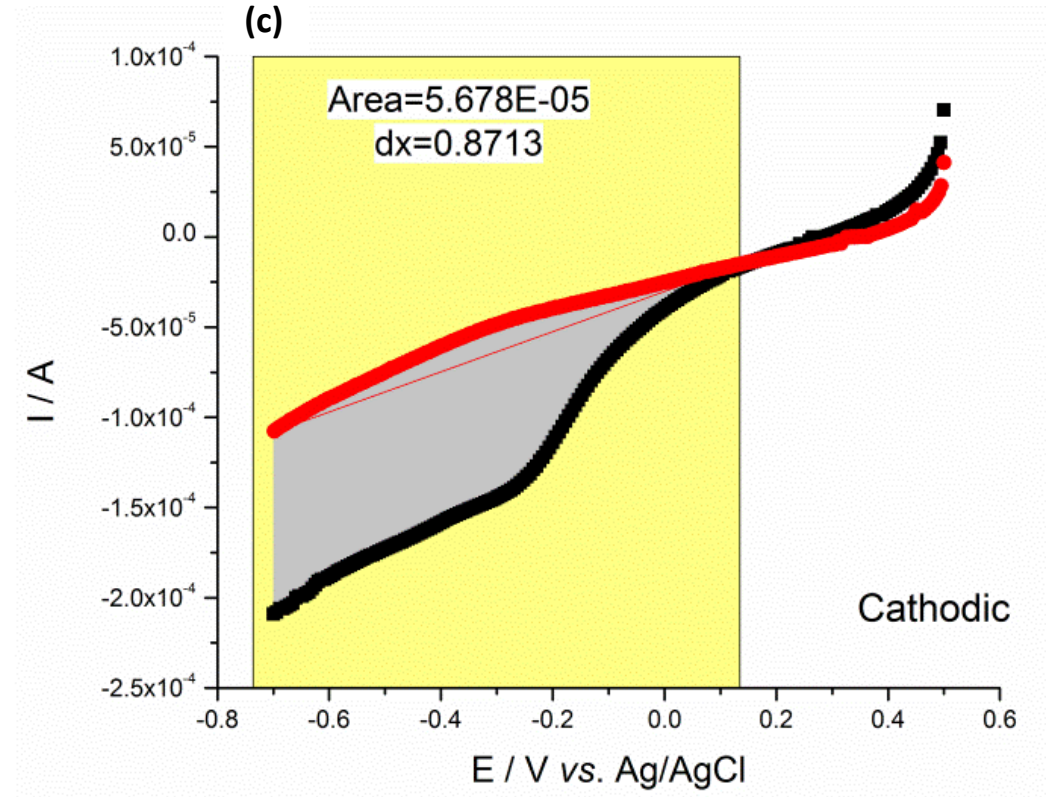
(c)
Area=5.678E-05
dx=0.8713
Cathodic
I / A
E / V vs. Ag/AgCl
1.0x10-4
5.0x10-5
0.0
-5.0x10-5
-1.0x10-4
-1.5x10-4
-2.0x10-4
-2.5x10-4
-0.8
-0.6
-0.4
-0.2
0.0
0.2
0.4
0.6

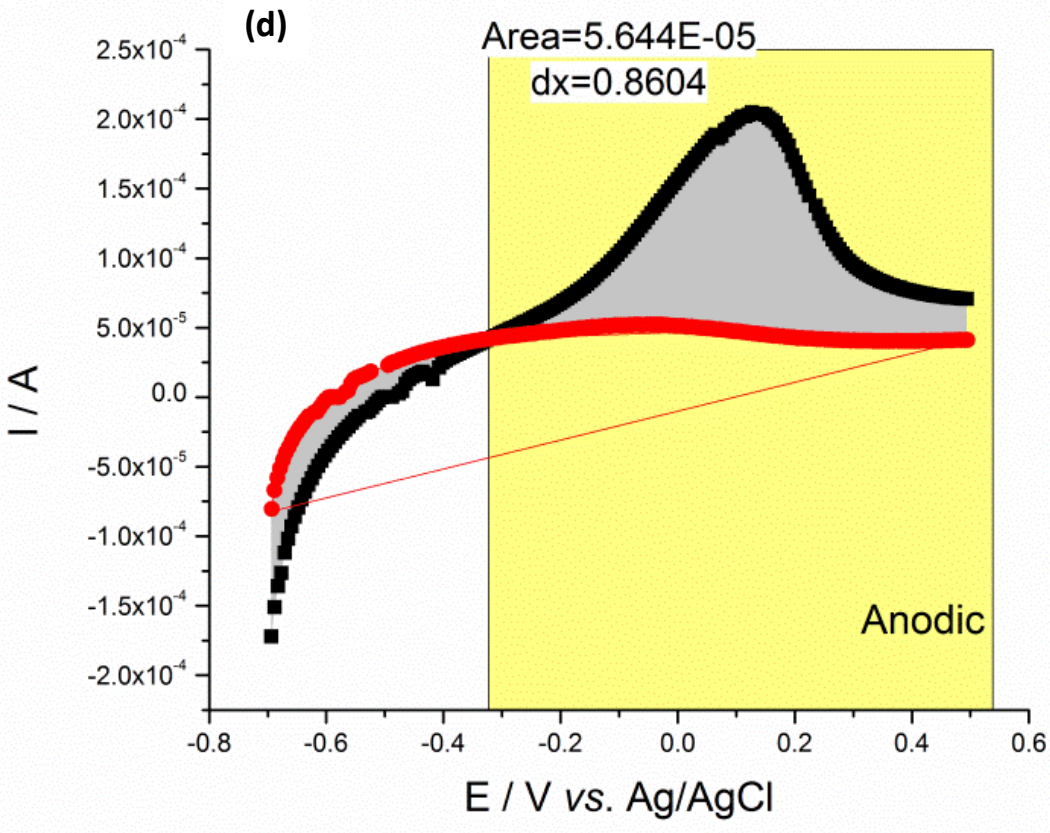
(d)
Area=5.644E-05
dx=0.8604
Anodic
I / A
E / V vs. Ag/AgCl
2.5x10-4
2.0x10-4
1.5x10-4
1.0x10-4
5.0x10-5
0.0
-5.0x10-5
-1.0x10-4
-1.5x10-4
-2.0x10-4
-0.8
-0.6
-0.4
-0.2
0.0
0.2
0.4
0.6

Figure S 3.3 (a) Cyclic voltammograms of magnetite electrode scanned from 50 mV/s to 1000 mV/s in the background electrolyte containing 0.1 M NaCl. All 15 cycles with the OCPs are showed. (b) The charge density of the cathodic and anodic scans and the ratio of the cathodic to anodic charge *vs.* the scan rates calculated from Figure 3.1a, b. Charge integrations for the cathodic (c) and anodic (d) scans at 1 V/s. The red current curves represent the background (current measured in electrolyte without uranium) and the black curves are the current measured in the 1 mM UO_2^{2+} solution with the same background electrolyte. Note that the red background current is not always wrapped inside the black analyte current. Here, only the areas in grey inside the yellow boxes, which are the current above the background, are integrated to calculate the charges.

Table S 3.1 OCPs of the voltamogramms in Figure S 3.3a.

scan rate	50 mV/s	250 mV/s	450 mV/s	650 mV/s	850 mV/s	1000 mV/s
OCP/V	0.091	0.091	0.101	0.109	0.101	0.087

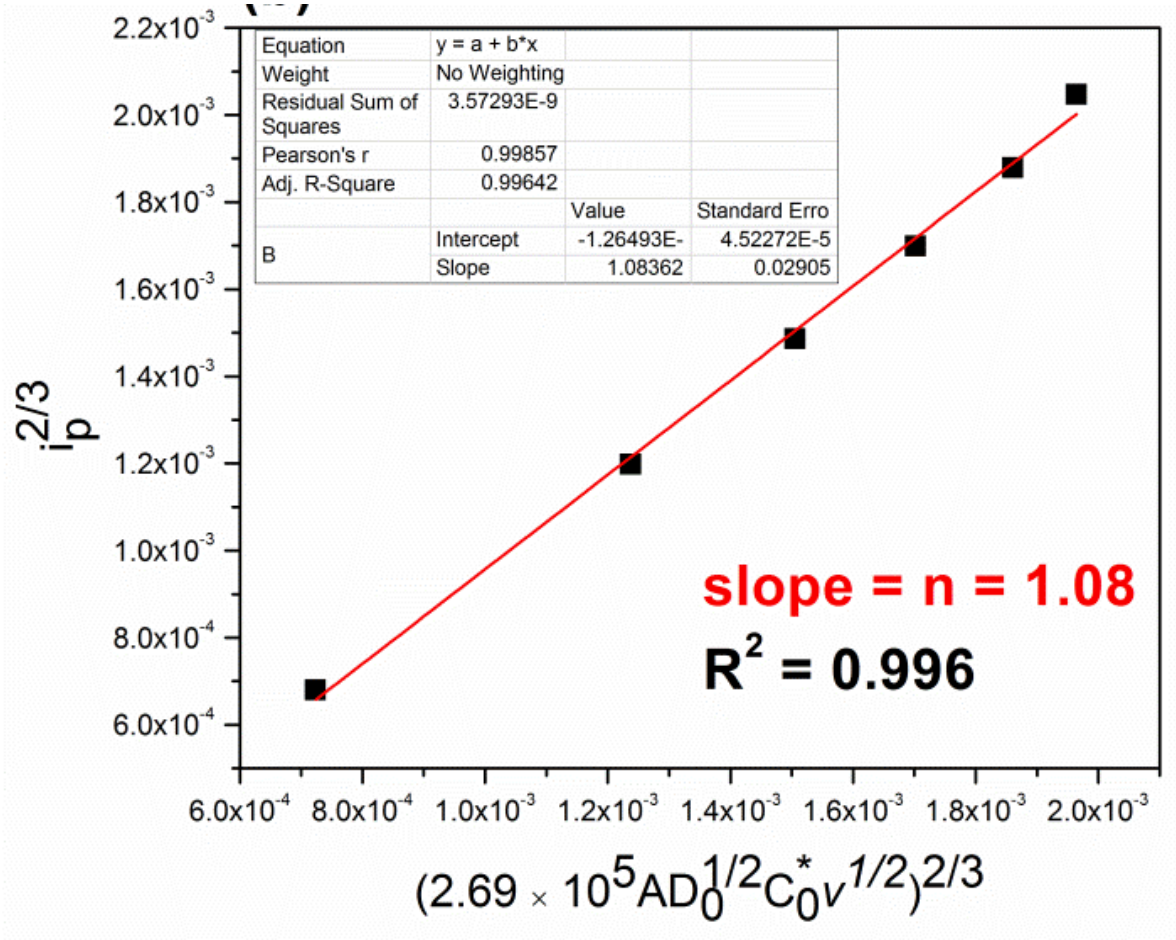

Figure S 3.4 Fitting the number of electrons transferred per redox step through the Randles-Sevcik equation.

Electrochemical-AFM

Movie link: AFM movie can be found online in the supporting information package at ASC: http://pubs.acs.org/doi/suppl/10.1021/acs.est.5b00025

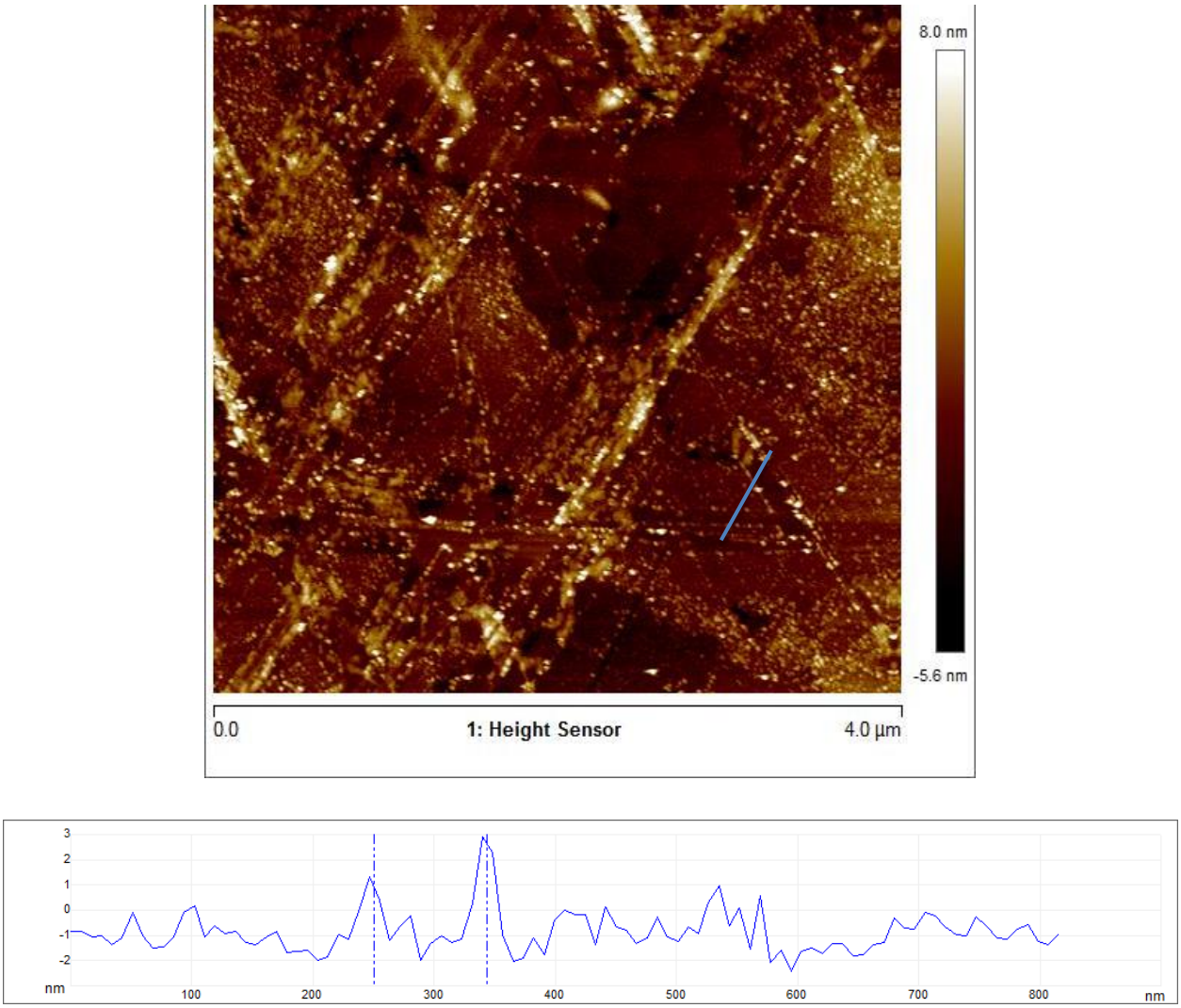

Figure S 3.5 Height sensor image of the (111) parting surface of magnetite in air. The depth profile showed nm roughness of the blue line region marked in the AFM image. The scale of the color bar next to the AFM image is from -5.6 nm to 8 nm.

XPS peak fitting methods

Previous studies (references 16, 37 and 38 in the manuscript) showed that the fitted peak positions of the U^{6+}, U^{5+}, U^{4+} peaks within the U $4f_{7/2}$ primary peak are between 382.5 eV to 379.8 eV. Each fitted peak has a separation of 0.5~1 eV apart from the neighboring peaks. Also, distances of the primary U $4f_{7/2}$ to the primary U $4f_{5/2}$ peaks were fixed at 10.8 eV during the fitting. The FWHM of the primary peaks were constrained to adopt the same value during the fitting, as well. Distances between the primary and satellite peaks were also constrained during the fitting and the fitted results are listed in Table S3.2. As can be seen from the Table S3.2, the fitted U^{6+} (382.0 eV to 381.7 eV) and U^{5+} (380.3 eV to 380.9 eV) peak positions are consistent with the published range. In addition, when modelling the system using all three oxidation states with satellites included, the U(IV) component drops to near 0%, which indicates that the main contributions inside the primary peaks are from U^{6+} and U^{5+}.

The Shirley type background with a start offset of 10 and end offset of 0 was used in all spectra fitting except the spectrum of the sample prepared at -0.1 V, where a start offset of 2 was used to acquire a better fit to the background.

Table S 3.2 Peak positions, FWHM and line shapes used for the fitting of the U^{6+} and U^{5+} components in U $4f_{7/2}$ primary and associated satellite peaks. A() GL() parameters indicate the asymmetry and Gaussian-Lorentzian mix line shape used in the software CasaXPS.

sample	parameters	primary peak U $4f_{7/2}$		satellite peak U $4f_{7/2}$		
		U^{6+}	U^{5+}	U^{6+}_4eV	U^{6+}_10eV	U^{5+}_8eV
	Line shape	A(0.35,0.2)GL(30)	A(0.35,0.2)GL(45)	GL(0)	GL(30)	GL(60)
-0.1V	position/eV	382.0	380.3	3.4	10	8.3
	FWHM	1.80	1.80	1.94	2.65	2.60
-0.3V	position/eV	381.8	380.7	3.4	10	8.3
	FWHM	1.44	1.44	2.50	2.65	2.26
-0.5V	position/eV	381.7	380.5	3.4	10	8.3
	FWHM	1.54	1.54	2.50	2.65	2.54
-0.7V	position/eV	381.7	380.7	3.4	10	8.3
	FWHM	1.54	1.54	2.5	2.66	2.00
-0.9V	position/eV	382.0	380.9	3.4	10	8.3
	FWHM	1.48	1.48	2.50	2.65	2.00

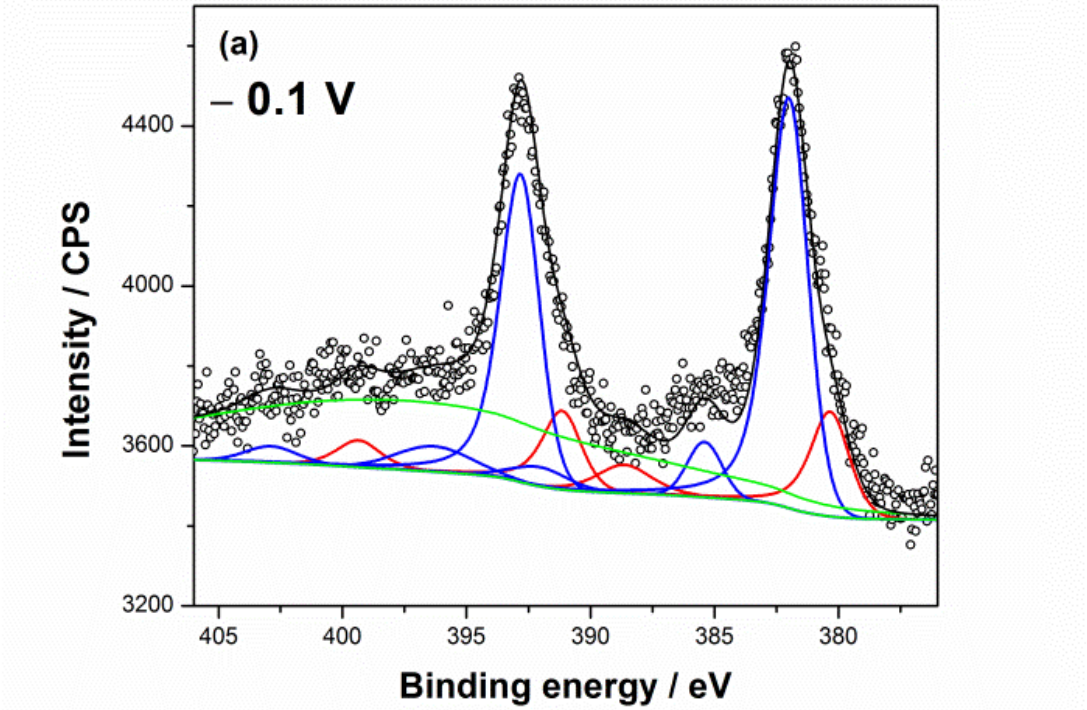
(a)
– 0.1 V
Intensity / CPS
4400
4000
3600
3200
405
400
395
390
385
380
Binding energy / eV

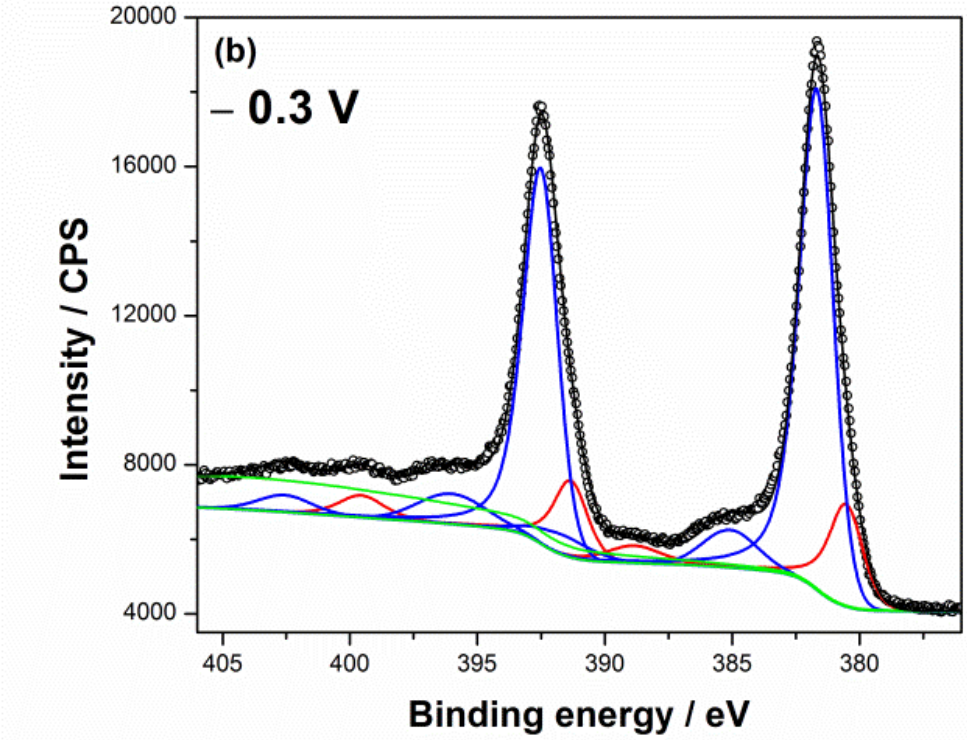
(b)
– 0.3 V
Intensity / CPS
20000
16000
12000
8000
4000
405
400
395
390
385
380
Binding energy / eV

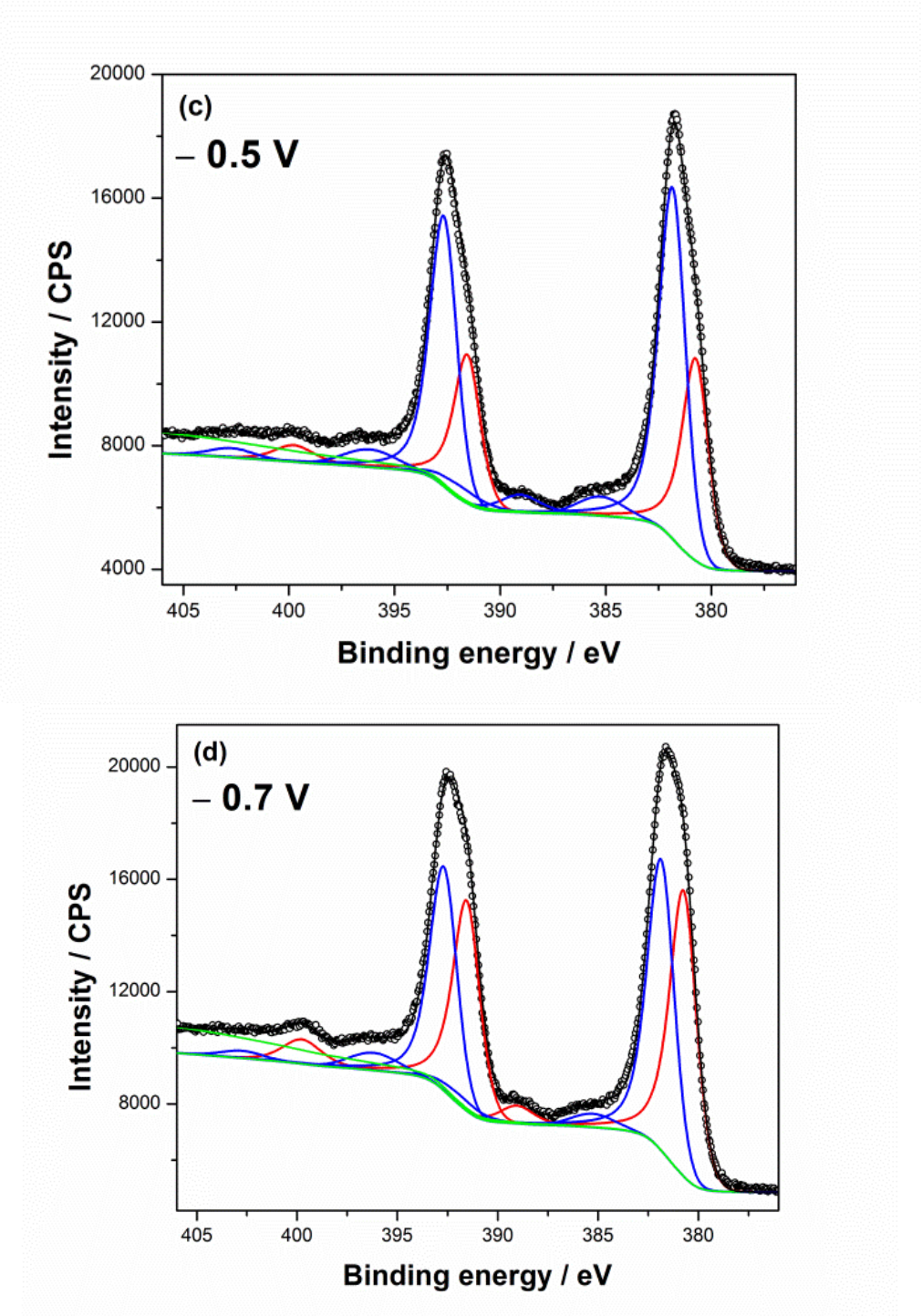

Figure S 3.6 Fitting results of the U 4f XPS spectra of the uranium deposited magnetite electrodes prepared at -0.1 V, -0.3 V, -0.5 V and -0.7 V. Constant voltages were applied on the magnetite electrode for 3 min in 1 mM UO_2^{2+} solution with the background solution of 0.1 M NaCl at pH = 3.4.

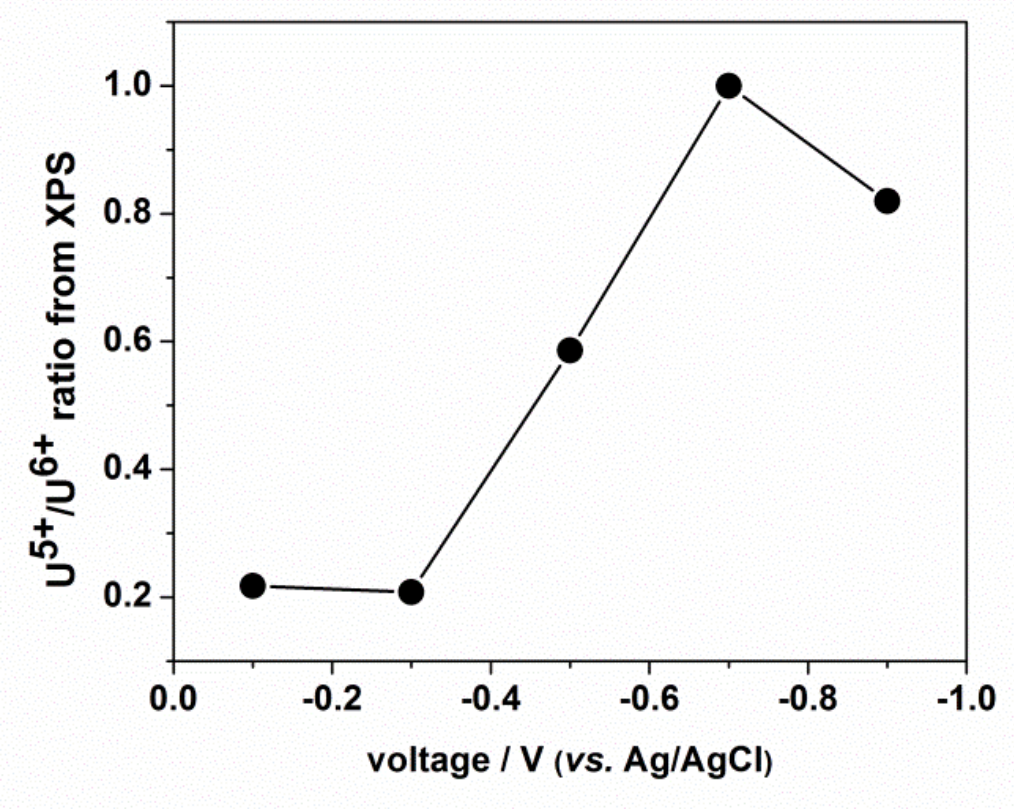

Figure S 3.7 U^{5+}/U^{6+} ratio calculated from the U 4f XPS spectra as a function of voltage.

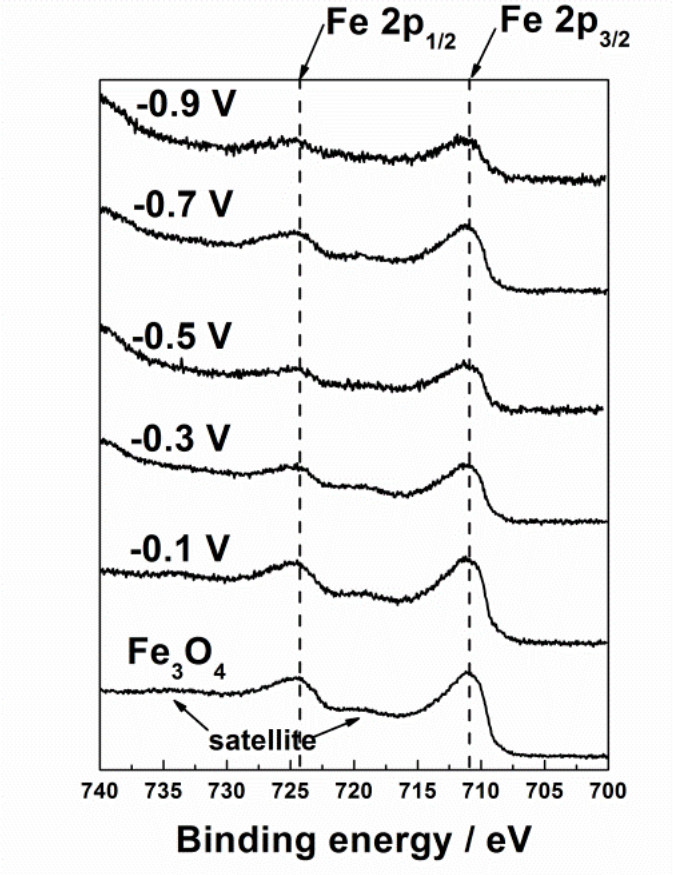

Figure S 3.8 The Fe 2p XPS spectra of the magnetite electrodes as a function of voltage. The intensity of the peaks decreased with the decrease of the voltage, which is caused by the increased thickness of the uranium layer on top of the magnetite substrate. The diminishing satellite peaks indicate the initial partially oxidized magnetite surface was reduced with the decrease of the voltage.

AES

The atomic ratio of U to O in the sample prepared at -0.9 V was calculated using the software MultiPak based on the following equation:

$$C_i = \alpha_i I_i / \sum_j \alpha_j I_j$$

Here, C_i is the atomic concentration of the element i to be calculated in the sample, α_i/α_j are the inverse relative sensitivity factors of the identified elements and I_i/I_j are the peak heights of selected Auger transition on the derivative Auger spectrum. The relative sensitivity factors (10 kV) used for U and O are 1.6839 and 0.7878. The Auger transition peaks used for U and O are at 77.8 eV and 514.2 eV.

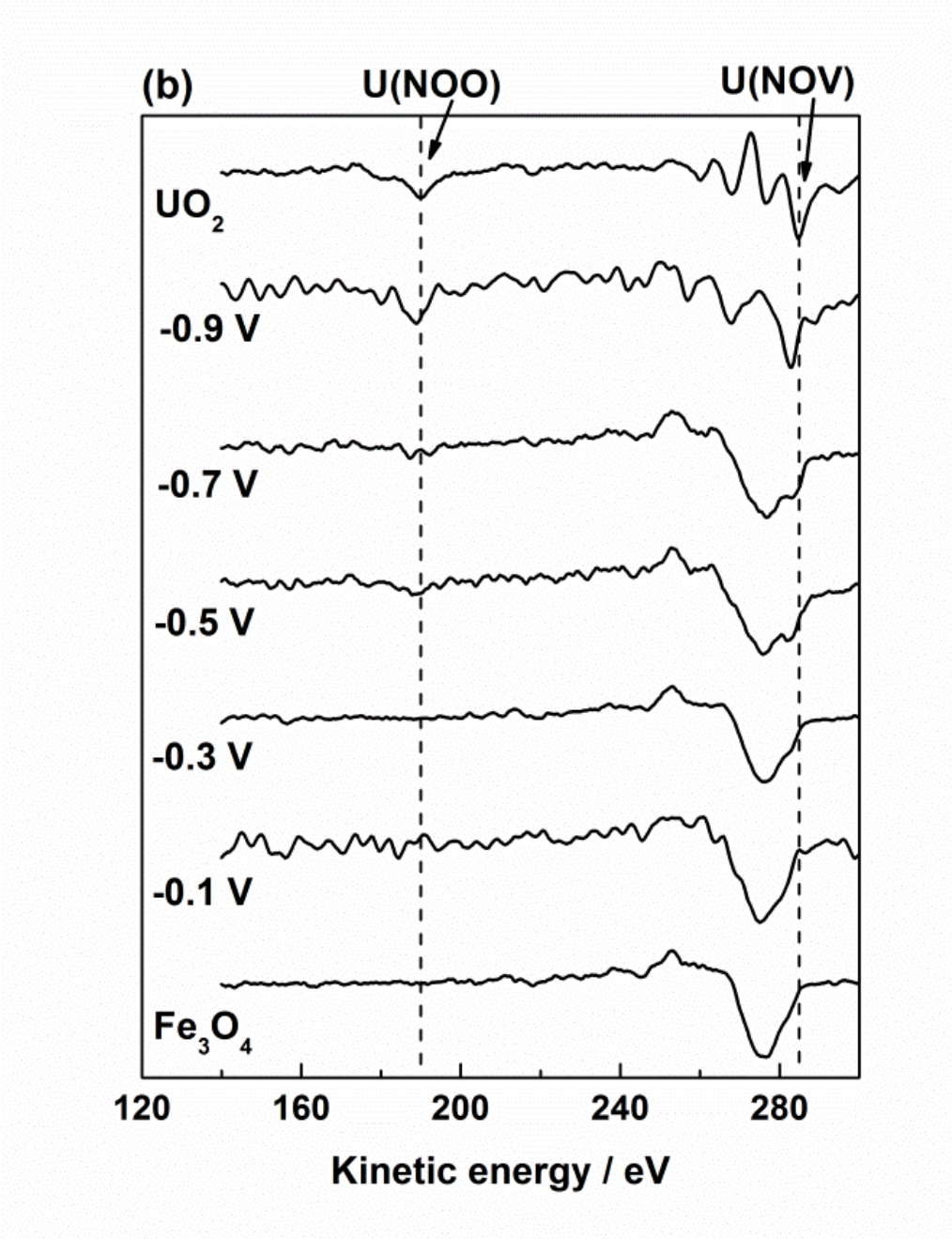

Figure S 3.9 Zoomed-in area of Figure 4(a) from 120~285 eV showed the AES transition of U (NOO) and U (NOV). U (NOO) peaks are only evident in the sample prepared at -0.9 V (189.0 eV) and the UO_2 standard (190.2 eV). The U(NOV) peaks exhibit growing intensities with decreasing voltages, the peak positions have a constant value of 283.0 eV for samples prepared at different voltages, except for the UO_2 sample where the peak position is at 284.8 eV. The three letters represent energy levels of the three electrons involved in the Auger transition.

Table S 3.3 Comparison of theoretical peak positions of the uranium AES transitions to the observed values in this study.

	AES transitions, kinetic energy/ Ev				
sample	U (O_5P_3V)	U (O_3O_4V)	U (O_5VV)	U (O_3O_5V)	U ($O_3P_1P_1$)
calculated[1]	76.7	91.5	93.1	99.3	106.0
UO_2, exp[1]	75.5	--	93.7	101.0	104.0
UO_2, this study	77.8	88.6	94.2	99.4	111.4
-0.9 V	77.6	89.6	--	98.8	110.6
-0.7 V	77.8	89.6	93.8	99.6	110.2, 112.6
-0.5 V	77.6	89.2	93.6	99.4	110.0, 111.6
-0.3 V	77.8	89.2	93.8	99.0	111.4
-0.1 V	77.8	89.3	92.8	101.3	112.3

XANES

The U L_3-edge XANES spectra were fitted to three components. The arctangent function was used to fit the rising edge and two Gaussian functions were used to fit the edge peak and the post-edge shoulder. The sample prepared at -0.7 V has the largest negative shifts of the peak positions as compared to that of the sample prepared at -0.1V sample (Fig S3.11, Table S3.4).

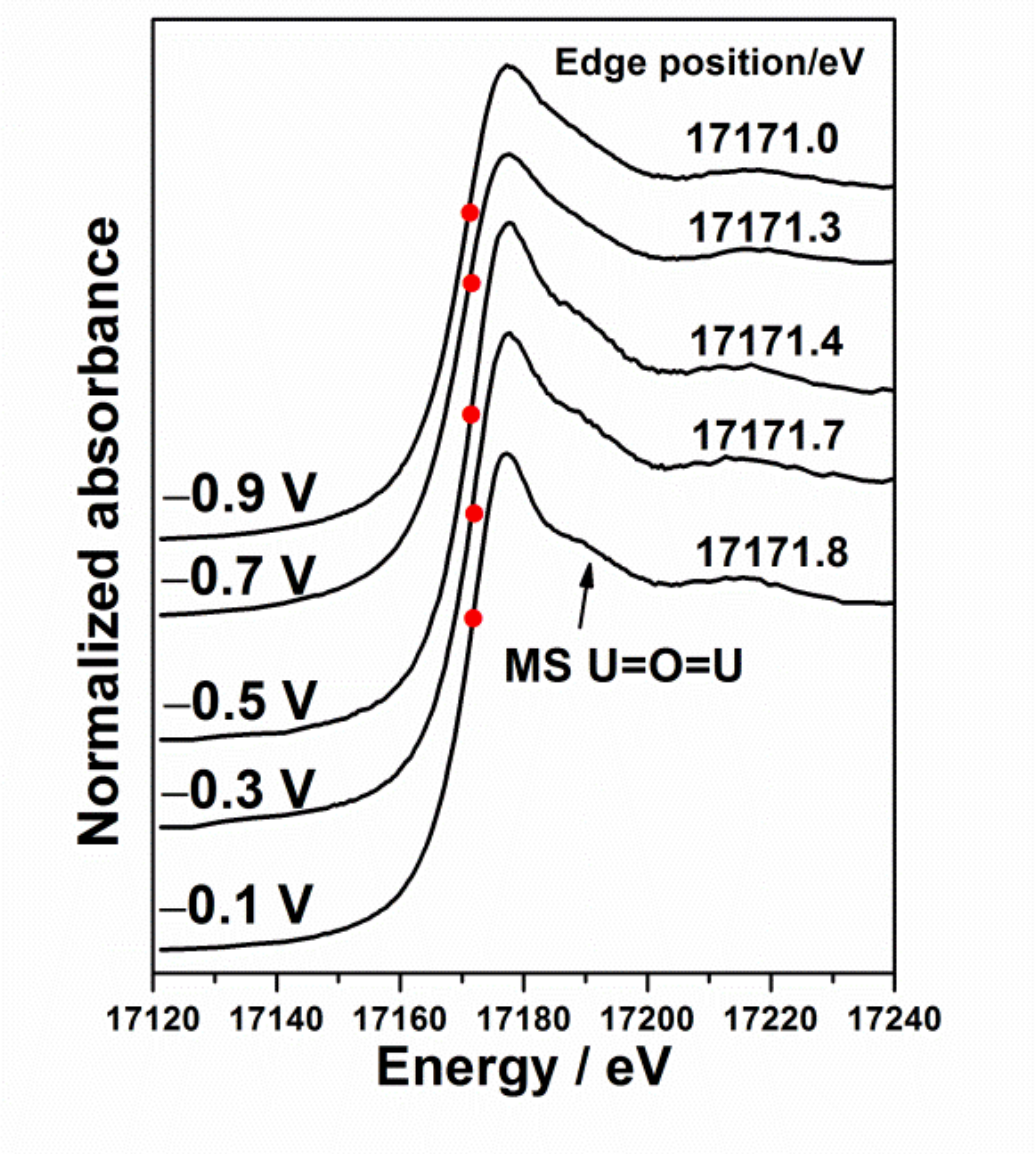

Figure S 3.10 XANES of U L_3-edge spectra as a function of deposition potentials. The red dots indicate the inflection positions. The arrow indicates the post-edge peak which is about 15 eV above the edge-peak. The post-edge feature is caused by multiple scattering of photoelectrons in the linear uranyl (UO_2^{2+}) moiety.

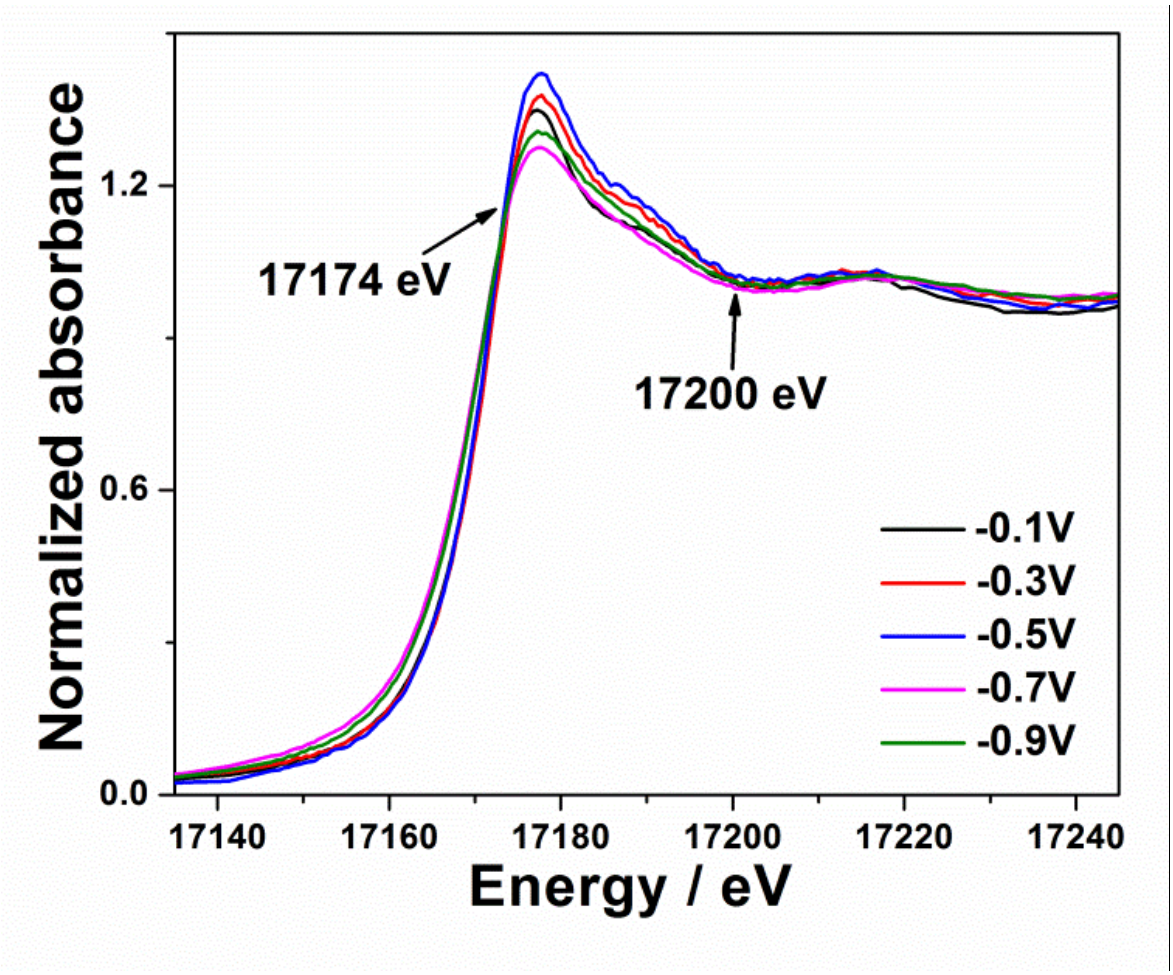

Figure S 3.11 XANES spectra as shown in the manuscript (FIGURE 5) but with a larger X-axis range. The two arrows indicate the energies of two features that are consistent with isosbestic points.

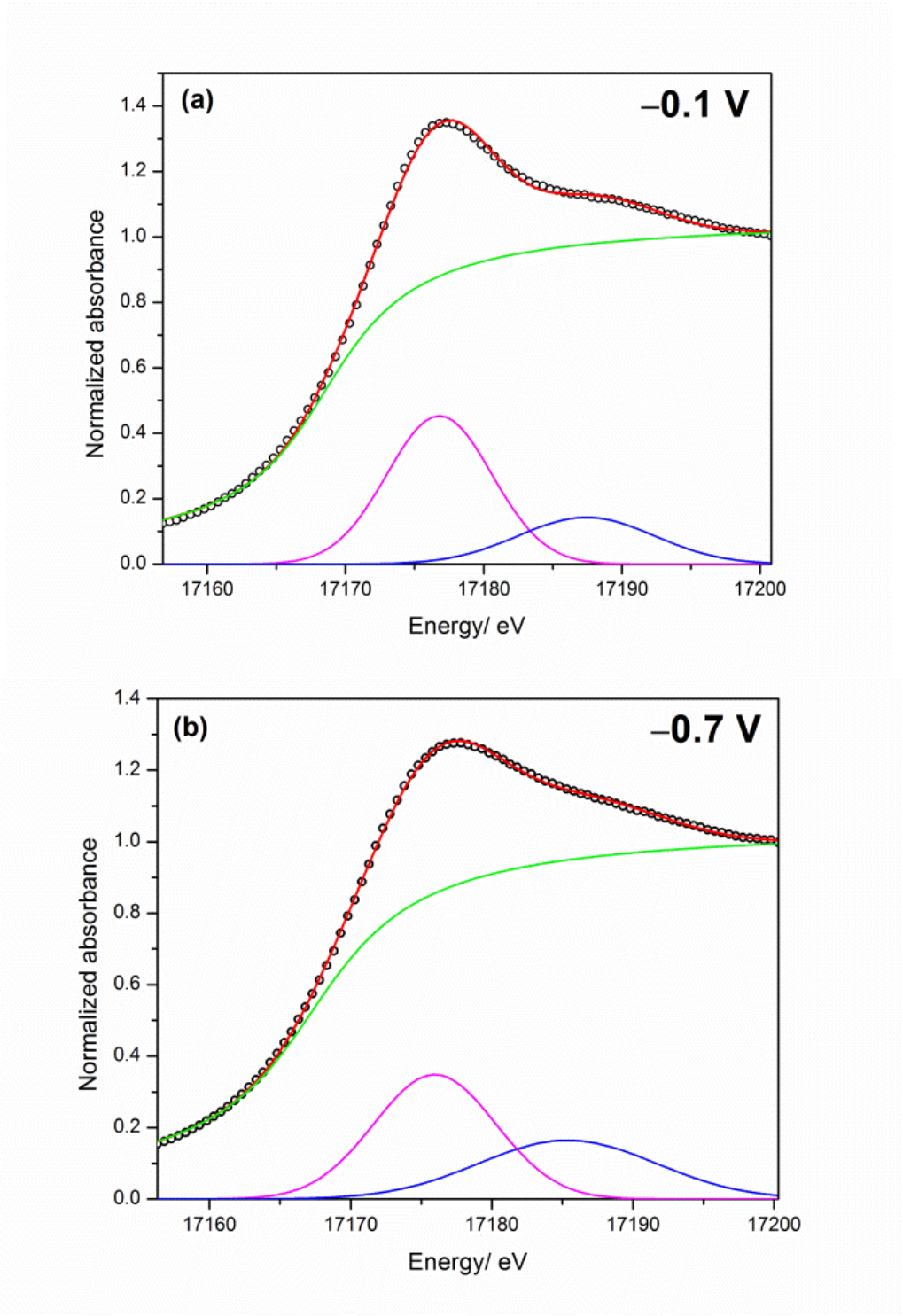

Figure S 3.12 U L_3-edge XANES fitting results of the sample prepared at (a) -0.1 V and (b) -0.9 V. The open circles represent the data and the red lines are the fitted curves. The arctangent and two Gaussian components are shown in green, pink, and blue lines.

Table S 3.4 XANES fitting results of the U L_3-edge XANES spectra in Figure 5 using arctangent and two different Gaussian functions.

Functions	Parameters	-0.1 V	-0.3 V	-0.5 V	-0.7 V	-0.9 V
Arctangent	center	17168.6	17168.9	17168.8	17167.3	17167.5
	step	1.06	1.07	1.08	1.05	1.06
	width	5.0	5.0	4.8	5.8	5.3
Gaussian 1	E_0	17176.8	17177.2	17177.0	17175.9	17176.1
	height	4.35	4.81	5.12	3.58	3.55
	FWHM	8.97	9.59	9.51	9.98	9.58
	area	4.35	4.81	5.12	3.58	3.55
Gaussian 2	E_0	17187.5	17188.0	17187.7	17184.9	17185.1
	height	1.77	2.01	2.29	2.79	2.89
	FWHM	11.56	11.23	11.65	15.31	14.94
	area	1.77	2.01	2.30	2.79	2.89

EXAFS

Fitting methods

Because of the increasing noise in the EXAFS data at high *k*-values, most of the $k^2\chi(k)$ from 3-9.5 $Å^{-1}$ was used to obtain the Fourier transforms of the $k^2\chi(k)$ EXAFS. Minor adjustments of the data range were made depending upon the quality of the response.

The model used for the first shell contains the uranium coordinated with 2 axial oxygen atoms (Oax). The second shell was modeled with 5 equatorial oxygen atoms (Oeq). Fitting tests revealed that the model using 5 equatorial O with the same bond length is unsatisfactory. Instead, fittings using 2 short U-Oeq bonds and 3 long U-Oeq improved the fitting quality in a statistically significant fashion. Including multiple scattering paths between the U and Oax had only a minor influence on the fitting results, so they were not included in the model. The distant U-Fe interactions at 3.6-3.8 Å were used to fit the fourth shell of scatters about U. Other pathways using U-U and U-Na did not provide fits that were as good as the U-Fe model. However, in the sample prepared at -0.3 V, adding the U-Fe scattering into the model did not improve the fitting at all, so it was not included in the fitting for this sample.

The S_0^2 was fixed at 0.95, and the coordination numbers are fixed too. The coordination numbers were allowed to float if the fitting quality was insufficient with fixed coordination numbers.

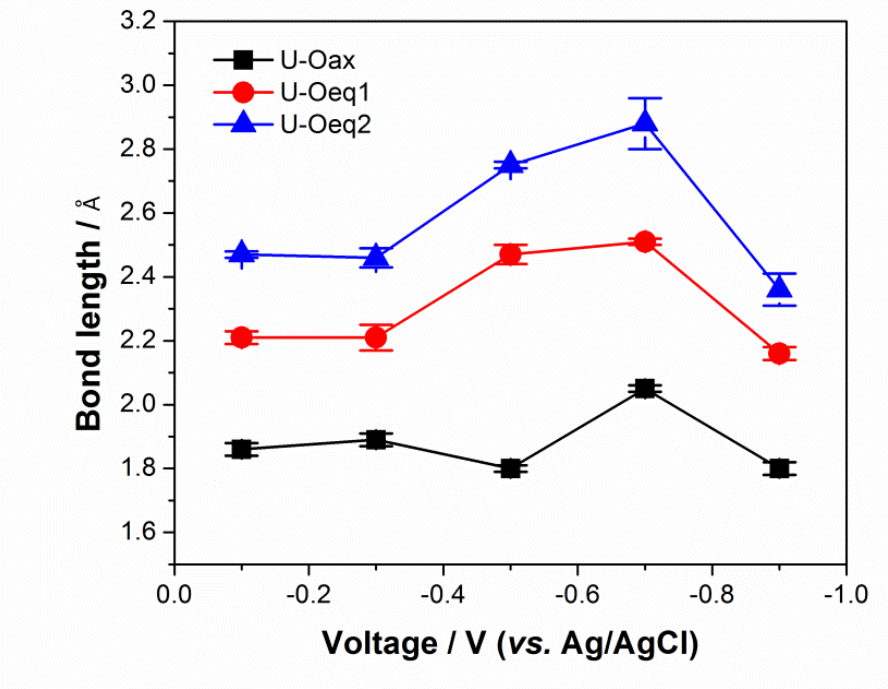

Figure S 3.13 Bond lengths obtained from the fitting results of U L_3 EXAFS in Table 3.1 *vs.* the potential.

The sample prepared at -0.7 V showed a relative narrow peak on its Fourier transform (FT) magnitude data (Figure 3. 6) and a large σ^2 value (Table 3.1) using the model containing two types of U-Oeq distances. Therefore, it is possible that this sample may contain only one type of U-Oeq coordination environment as the fitting results shown below. Higher quality data may be needed to accurately fit the equatorial oxygen shells for this sample.

Table S 3.5. Best-fit values of the U L_3-edge EXAFS spectra of the sample prepared at -0.7 V using one type of U-Oeq distance.

Sample	Path	**CN**	R / Å	σ^2 / Å^2	ΔE_0 / eV	S_0^2	χ_ν^2
-0.7 V	U-Oax	2	2.04 ± 0.01	0.0034	10	0.99	39.63
	U-Oeq	5	2.51 ± 0.02	0.0244			

Reference

1. Allen, G. C.; Wild, R. K.; Auger spectroscopy of uranium. *Journal of the Chemical Society-Dalton Transactions* **1974**, 493-498.

Chapter 4 Thermodynamic mixing properties of the UO_2-HfO_2 solid solution: Density functional theory and Monte Carlo simulations

Abstract

HfO_2 is a neutron absorber and has been mechanically mixed with UO_2 in nuclear fuel in order to control the core power distribution. During nuclear fission, the temperature at the center of the fuel pellet can reach above 1300 K, where hafnium may substitute uranium and form the binary solid solution of UO_2-HfO_2. UO_2 adopts the cubic fluorite structure, but HfO_2 can occur in monoclinic, tetragonal, and cubic structures. The distribution of Hf and U ions in the UO_2-HfO_2 binary and its atomic structure influence the thermal conductivity and melting point of the fuel. However, experimental data on the UO_2-HfO_2 binary are limited. Therefore, the enthalpies of mixing of the UO_2-HfO_2 binary with three different structures were calculated in this study using density functional theory and subsequent Monte Carlo simulations. The free energy of mixing was obtained from thermodynamic integration of the enthalpy of mixing over temperature. From the ΔG of mixing, a phase diagram of the binary was obtained. The calculated UO_2-HfO_2 binary forms extensive solid solution across the entire compositional range, but there are a variety of possible exsolution phenomena associated with the different HfO_2 polymorphs. As the structure of the HfO_2 end member adopts lower symmetry and becomes less similar to cubic UO_2, the miscibility gap of the phase diagram expands, accompanied by an increase in cell volume by 7-10% as the structure transforms from cubic to monoclinic. Close to the UO_2 end member, which is relevant to the nuclear fuel, the isometric uranium-rich solid solutions exsolve as the fuel cools, and there is a tendency to form the monoclinic hafnium-rich phase in the matrix of the isometric, uranium-rich solid solution phase.

Introduction

Neutron absorbers may be used in fuel rods in order to depress the power level of freshly loaded nuclear fuel UO_2 and to permit higher loading of fuel to achieve longer core life [1]. Neutron absorbing materials can be coated surrounding fuel pellets, doped into the cladding materials or mechanically mixed with UO_2 [2]. Incorporation of burnable neutron absorbing materials into the fuel can level the power distribution, such that power is generated across the core region rather than produced only close to the small area where control rods have been removed. Hafnium is a neutron absorber which has five stable isotopes, ^{176}Hf (natural isotopic abundance 5.2%, thermal capture cross section 23 barns), ^{177}Hf (18.6%, 373 barns), ^{178}Hf (27.1%, 84 barns), ^{179}Hf (13.7%, 41 barns), and ^{180}Hf (35.2%, 13 barns). The removal of one isotope of hafnium by absorption of neutrons leads to the production of another neutron absorber, and this continues through a chain of five absorbers. Among all five Hf isotopes, ^{177}Hf has the highest cross section, and further transmutation to other isotopes will decrease the neutron cross sections. Therefore, enriching hafnium in ^{177}Hf leads to a lower residual reactivity burden than that of hafnium with natural isotopic ratio, and experimental research has been conducted in order to investigate the potential benefits of using ^{177}Hf as the burnable neutron poison where $^{177}HfO_2$ was mixed with UO_2 to make homogenously distributed ^{177}Hf fuel pellets [1].

During the fission of the fuel, the temperature at the center of the fuel pellets can reach above 1300 K [3], where Hf may diffuse into the atomic structure of UO_2 to form a solid solution, and the UO_2-HfO_2 binary with different structures may form. UO_2 has the cubic fluorite structure, but HfO_2 exists in three different structures at ambient pressure. At room temperature, HfO_2 exists in the baddeleyite monoclinic structure, which is the most stable phase. At about 2000 K, HfO_2 undergoes a phase transition to the tetragonal phase, and at around 2900 K, tetragonal hafnia transforms to the high-temperature cubic fluorite structure [4-10]. As a result, the influence of the UO_2-HfO_2 binary solid solution on the thermal conductivity and melting temperature of the fuel depends both on the atomic structure and composition of the fuel on the UO_2-HfO_2 binary. The thermodynamic mixing properties of the UO_2-HfO_2 solid solution were calculated, and the phase diagram of the UO_2-HfO_2 binary was derived. In addition, exsolution phenomena, the energetics of cation ordering, and the similarity to the UO_2-ZrO_2 binary were investigated.

Methods

Calculations of the total energy

Energy calculations are based on density functional theory (DFT) using the Cambridge serial total energy package (CASTEP) [11]. The generalized gradient approximation (GGA) with Perdew and Wang's 1991 (PW91) was used for the electron exchange-correlation energy. The DFT+U methods were first tested for the modeling of the UO_2-HfO_2 solid solution. In order to test the influence of localized orbitals on the excess energies of mixing, we have tested the DFT+U method for the UO_2-HfO_2 solid solution modeling, and in some cases, the system did not converge to the ground state (thus producing unreliable excess energies of mixing). For a small number of configurations, we compared the excess energies of mixing of ramped DFT+U with the classical DFT approach and found that the differences in the excess enthalpy of mixing changed by only a small fraction of a kJ/(mol exchangeable cations) (even though the total energy of a configuration may change by a few kJ/mol). This means that the changes due to a DFT+U approach largely cancel out across the solid solution series. However, due to the number of configurations that we calculated, a ramped DFT+U approach for each configuration would have been computationally too expensive. In addition, the excess energies (Eq. (1)) obtained using GGA-PW91 with ultrasoft pseudopotentials for core electrons of U, Hf, and O, which are the parameters used for current calculations, were compared with results using GGA-PBE, on the fly pseudopotentials, and less than 7% difference of the total energy was found. Since HfO_2 occurs, dependent on the temperature regime, in the monoclinic, tetragonal, and cubic structures, the total energies of different (about 25 for each structure type) Hf-O configurations with different Hf-U ratios were calculated within all three different structures. All geometry optimizations were performed without symmetry constraints, i.e., the unit cell parameters as well as the atomic positions within the unit cell were optimized using P1 symmetry. A 2×1×1 supercell was used for all structures, each containing 8 exchangeable cations for U-Hf substitution (Fig. 4.1). Spin polarization was included in the calculation for the configurations containing U^{4+} cations. All the spins of U^{4+} cations (each having two unpaired spins) have the same orientation in order to avoid any additional energy variability from possible spin ordering. This is justified because the gain in energy from antiferromagnetic spin ordering in pure UO_2 is already weak; antiferromagnetic interactions in Hf-UO_2 solid solutions would contribute even

less. However, the fit of cation-cation interaction parameters would be a lot more complex and unreliable for relatively little gain in accuracy. The planewave cut-off energy was 500 eV and 9 k-points were used for all calculations.

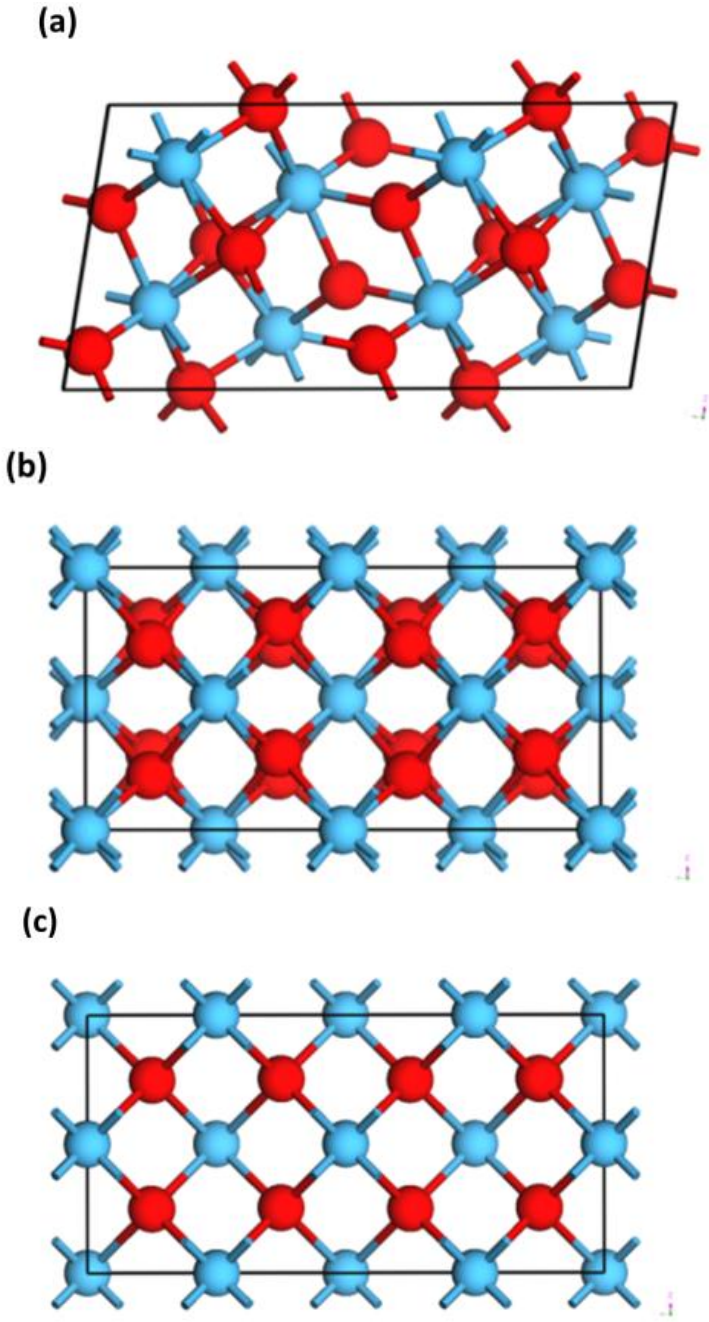

Figure 4.1. 2×1×1 supercell of (a) monoclinic (*P2₁/C*), (b) tetragonal (*P4₂/nmc*), and (c) cubic (*Fm3m*) HfO_2, projections along [010]. Red balls and blue balls denote O and Hf atoms, respectively.

Fitting of the cation exchange parameters

After geometry optimization of a number of different configurations, a series of ground-state energies at 0 K were obtained from the CASTEP calculations. The excess energy of mixing of the different UO_2-HfO_2 solid solutions was determined by using Eq. (1).

$$E_{excess} = E(U_xHf_{1-x}O_2) - xE(UO_2) - (1-x)E(HfO_2) \quad (1)$$

The excess energy term is defined as the difference between the energies of a certain cation configuration (CASTEP energy) from the mechanical mixture of the end members with the same concentration. The energy related to the cation exchange can be extracted from the total lattice energy calculated for many different configurations. The J formalism replaces the energies of mixing obtained from geometry optimizations using quantum-mechanical calculations by defining a set of effective pair energies, the J. It permits the expression of the excess energy of a solid solution as a combination of the excess energy terms related to pairs of interacting atoms [12-16]. In general, the excess total energy of mixing can be expressed as shown in Eq. (2), taking into account separate pairs of interactions for two cations, U and Hf respectively.

$$E_{excess} = E_0 + \sum_i (n^i_{U-Hf}E^i_{U-Hf} + n^i_{U-U}E^i_{U-U} + n^i_{Hf-Hf}E^i_{Hf-Hf}) \quad (2)$$

Where *i* indicates the type of neighboring interaction between pairs of cations (e.g., first, second, and third nearest-neighbor interactions in cubic structures), n represents the number of cation-cation interactions for each type, and E is the interaction energy between U-Hf, U-U, and Hf-Hf. The individual cation interaction energies E can be combined into a single term J called the cation exchange potential in Eq. (3).

$$J^i_{U-Hf} = E^i_{U-Hf} - \frac{1}{2}(E^i_{U-U} + E^i_{Hf-Hf}) \quad (3)$$

For simulating solid solutions using the cation interaction model, cation interaction energies ($E_{U\text{-}U}, E_{Hf\text{-}Hf}, E_{U\text{-}Hf}$) are not independent of the chemical composition. Therefore, E_0 in Eq. (2) is a concentration-dependent, but not configuration-dependent term that is used to capture the asymmetry (with respect to x=0.5) of the excess energy curves. E_0 is approximated by a Margules function in Eq. (4).

$$E_0 = x(1-x)[m_1x + m_2(1-x)] \quad (4)$$

The energy of mixing can be fit by the following Eq. (5):

$$E_{excess} = E_0 + \sum_i n^i_{U-Hf} J_{U-Hf} \quad (5)$$

The calculated excess energy of mixing were fit by both Margules terms and cation exchange potential *J* (U-Hf) in Table 1 [13, 14].

Table 4.1 Margules terms (m_1, m_2) and cation exchange parameters J_i (kJ/mol) in cubic, tetragonal and monoclinic structures of the UO_2-HfO_2 solid solution. J_1, J_2 and J_3 represent the first, second and third nearest neighbor interaction, respectively.

Structure	m_1	m_2	J_1	J_2	J_3	R^2
cubic	8.736	1.784	0.0078	-0.0249	-0.0023	0.975
tetragonal	7.229	2.922	-0.0007	0.0154	-0.0006	0.945
monoclinic	8.021	6.462	0.0075	-0.0236	0.0047	0.974

Monte Carlo simulation and thermodynamic integration

In the Monte Carlo simulation, the Markov chain was generated as follows. For each swapping attempt, two cations in the 8×4×4 supercell are randomly switched. The cation exchange parameters J_i obtained from fitting are used to calculate the excess energy of mixing of different configurations. The probability of whether to accept the new configuration can be determined by either of the two criteria. (1) If the new energy is lower than the previous one, the new configuration is accepted. (2) If the energy is higher than the previous one, Eq. (6) is used to calculate the probability, and if the probability is greater than a random number between 0 and 1, then the new configuration is accepted for the next swap.

$$P = e^{\frac{-\Delta E_{swap}}{k_B T}} \quad (6)$$

In Eq. (6), k_B is the Boltzmann factor and T is the temperature in Kelvin. The calculations follow an annealing process from 3000K to 298K.

Thermodynamic integration computes the difference of the free energy of the system between the reference state (T=∞) and the state of interest, *i.e.*, at a given temperature. The energy expression in Eq. (7), in which the energy of interest F can be calculated by integration from the reference states (completely disordered structure) with free energy F_0 to state of interest at a certain temperature and composition by continuously change the parameter λ (which can be equated to $1/T$, or an integration from $T=\infty$ ($\lambda=0$) to $1/T_{actual}$) from 0 to 1. The role of the Monte Carlo procedure is to provide a sufficient number of enthalpies of mixing (H) over which integration can take place to calculate the average free energy of mixing $<H>$ at each step of λ with reasonable accuracy but without sampling the complete set of configurations [17].

$$F = F_0 + \int_0^1 < H >_\lambda d\lambda \tag{7}$$

Calculation of the excess entropy of mixing can be derived directly from standard thermodynamics by using Eq. (8).

$$\Delta S_{mixing} = \frac{\Delta H_{mixing} - \Delta G_{mixing}}{T} \tag{8}$$

Note that the entropy contribution in Eq. (8) only describes the configurational entropy of the solid solution. While there is a vibrational entropy contribution to each structure and also a contribution from the zero-point energy, these contributions were estimated in the cubic structure using the following procedure.

Calculation of the vibrational entropy and zero-point energy

The vibrational entropies of the solid solution were calculated by using the General Utility Lattice Program (GULP) in the well-established cubic structure of UO_2 and HfO_2 [18]. The force potentials used for UO_2 and HfO_2 and were developed based on studies of Broglia et al [19]. This potential is a partial ionic potential based on the Morse functions. The parameters of the potentials used in the calculations and the calculated cell parameters and elastic constants can be found in the tables in the appendix. A total number of 2989 random configurations were generated and geometry optimized. Subsequently, the zero-point energies were calculated as a function of composition and the excess vibrational entropies were calculated as a function of

composition and temperature. The temperature was sampled from 298 K to 3000 K with a step of 200 K.

Results

Comparison of experimental and calculated cell parameters

The calculated unit cell parameters of the end members all have larger values than the experimental results. The calculated cell parameters have a small deviation of 0.7% for cubic UO_2. For HfO_2, which has three different structures, the deviations of cell parameters vary from 1.9% to 4.5%. This may be because some of the hafnia structures are high-temperature phases, whereas, the calculations were conducted at 0 K. The calculated unit cell parameters decrease approximately linearly with the increase in Hf concentration in all structures (Fig. 4.2a, b, and c). The cell volume increases by 7-10% as the structure transforms from cubic to monoclinic (Fig. 4.2d).

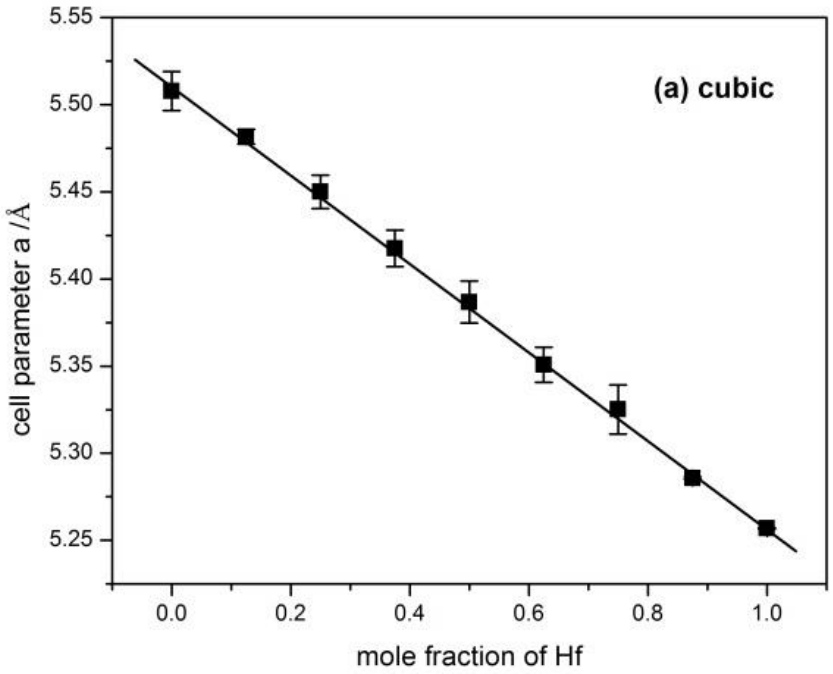

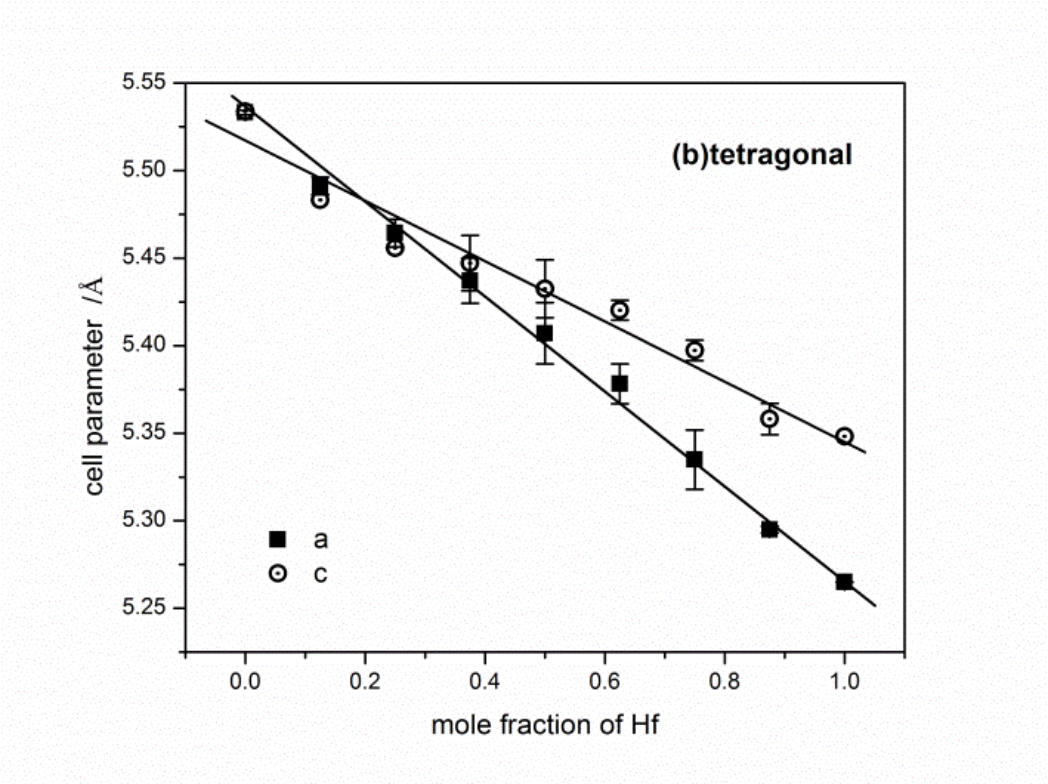
(b)tetragonal
cell parameter /Å
mole fraction of Hf
a
c
5.55
5.50
5.45
5.40
5.35
5.30
5.25
0.0
0.2
0.4
0.6
0.8
1.0

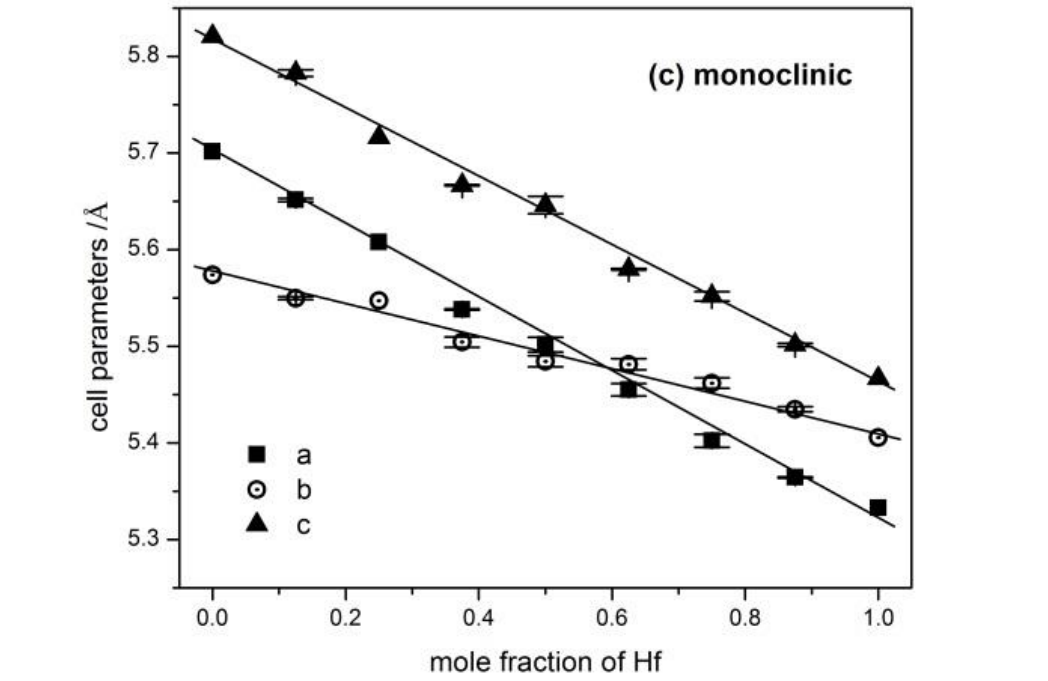
(c) monoclinic
cell parameters /Å
mole fraction of Hf
a
b
c
5.8
5.7
5.6
5.5
5.4
5.3
0.0
0.2
0.4
0.6
0.8
1.0

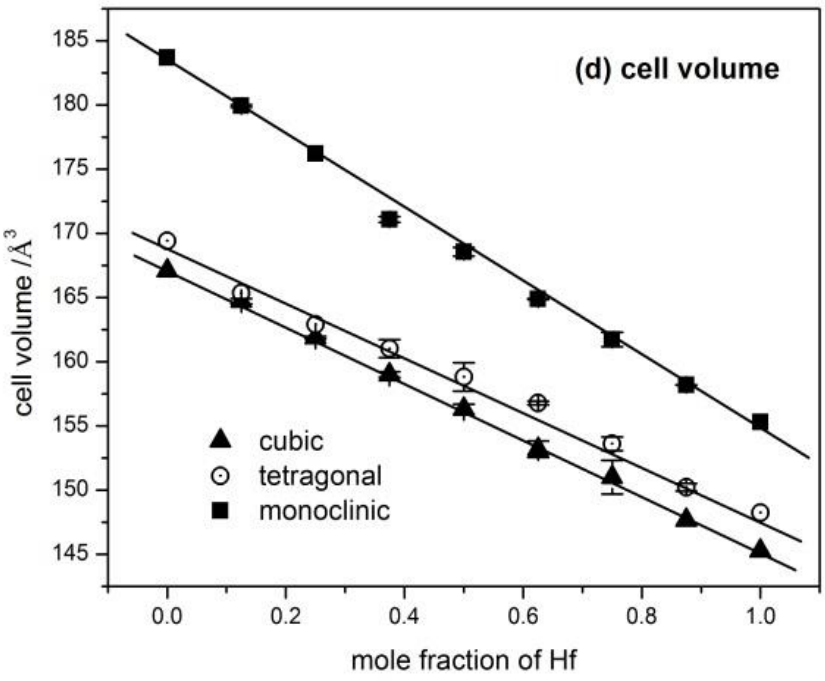

Figure 4.2. Calculated cell parameters as a function of the Hf mole fraction of the UO_2-HfO_2 solid solution in (a) cubic, (b) tetragonal, (c) monoclinic structures and (d) cell volume change. Each point is the average value of configuration with the same composition, and the error bars represent the standard deviation over different configurations (not from different computational parameters)

Table 4.2 Comparison between calculated and measured unit cell parameters of UO_2 (cubic) [20, 21] and HfO_2 (cubic, tetragonal and monoclinic) [22-24].

lattice parameters	*a* (Å)	*b* (Å)	*c* (Å)	*β* (˚)
cubic UO_2				
measured	5.4682			
calculated	5.508			
deviation (%)	0.73			
cubic HfO_2				
measured	5.115			
calculated	5.257			
deviation (%)	2.77			
tetragonal HfO_2				
measured	5.14		5.25	
calculated	5.265		5.348	
deviation (%)	2.43		1.87	
monoclinic HfO_2				
measured	5.1156	5.1722	5.2948	99.18
calculated	5.333	5.406	5.467	99.78
deviation (%)	4.25	4.52	3.25	0.60

Enthalpy of mixing

The enthalpy of mixing curves become less symmetric with respect to x(Hf)=0.5 as the structures adopt higher symmetry (monoclinic, tetragonal, cubic in Fig. 4.3). For the cubic series, the peak value of the enthalpy of mixing is at the Hf mole fraction of around 0.67, which shifts

towards 0.5 for tetragonal and monoclinic structures. Since the cation exchange parameters listed in Table 4.1 are small, there is hardly any temperature dependence of the enthalpy of mixing.

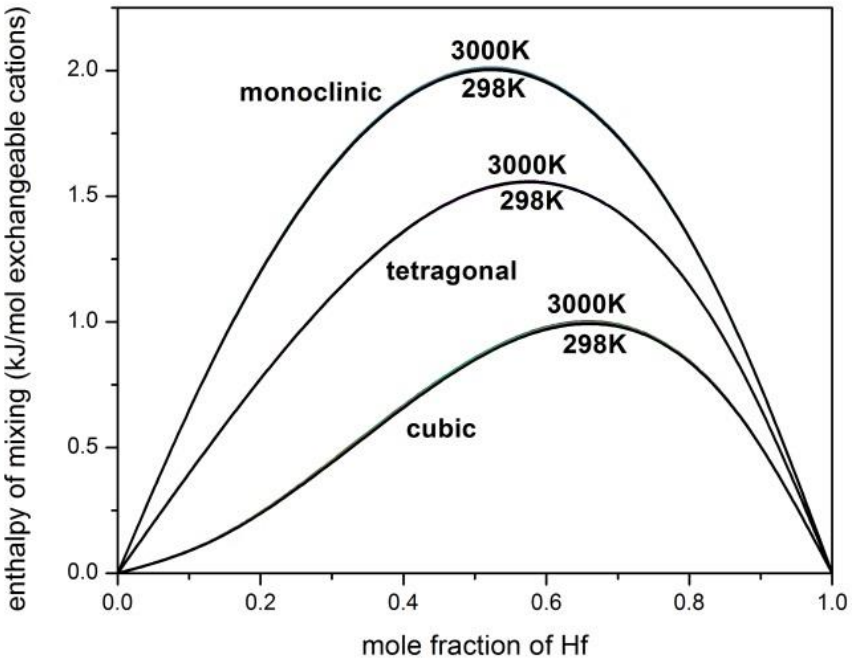

Figure 4.3. Enthalpy of mixing of the UO_2-HfO_2 solid solution calculated in cubic, tetragonal, and monoclinic structures with respect to end members adopted the corresponding structures as 0 enthalpy of mixing.

Entropy of mixing

Due to the minute temperature dependence of the configurational enthalpies of mixing, configurational entropies of mixing obtained were within ± 0.2 J/K·mol exchangeable cations difference of the point entropy of mixing (which would indicate no ordering preference) and were nearly independent of temperature in all three structures (Fig. 4.4a). The calculated vibrational entropies of mixing in the cubic structure are about 20 % of the configurational entropies of mixing at the Hf fraction of 0.5 (Fig. 4.4b).

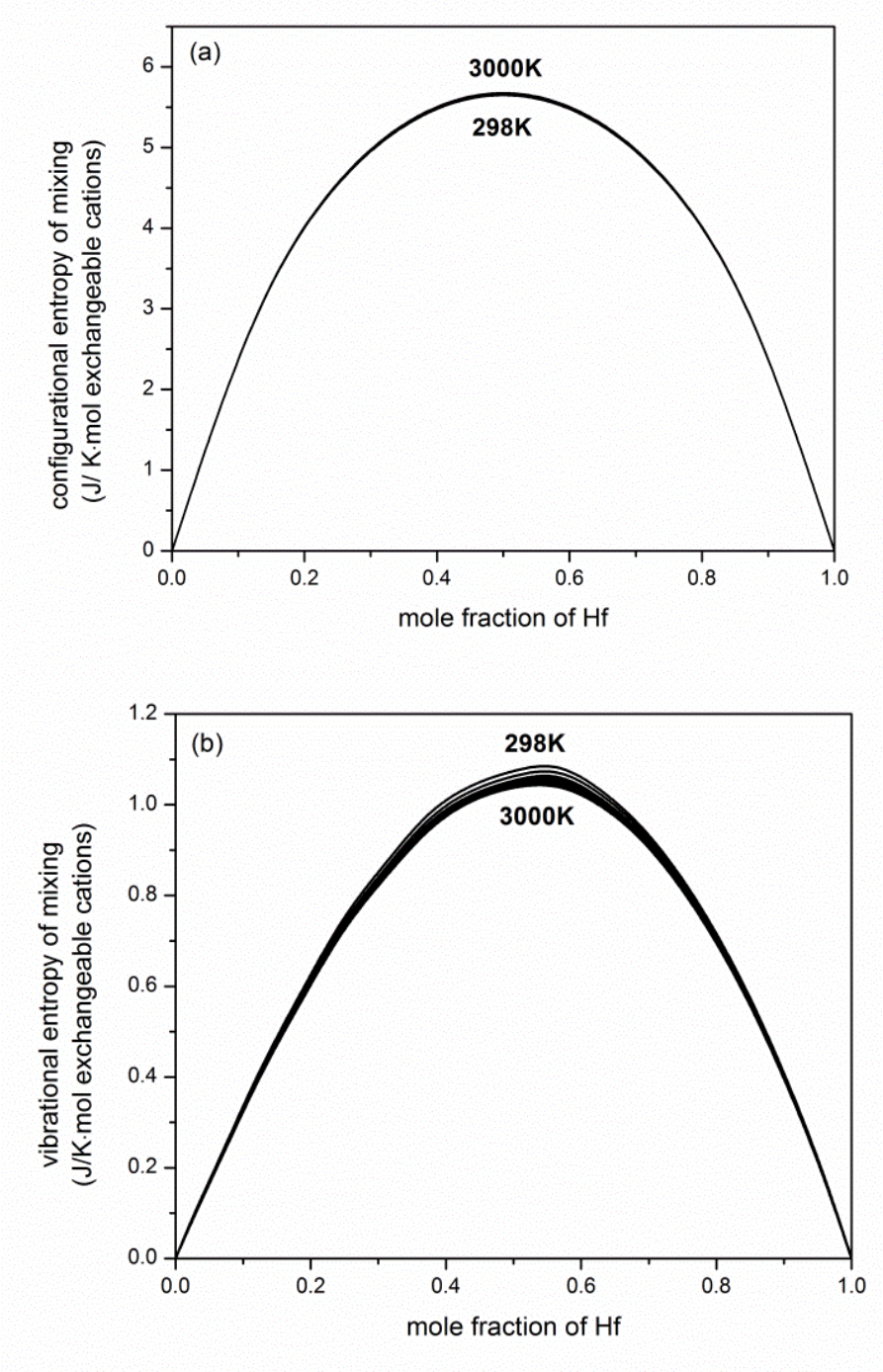

Figure 4.4. (a) Configurational entropy of mixing (for all three structures, the unit is in J/K·mol exchangeable cations) and (b) vibrational entropy of mixing (cubic structure only) of the UO_2-HfO_2 solid solution showing that the excess vibrational entropy of mixing is on the order of 20 % of the excess configurational entropy of mixing.

Gibbs free energy of mixing

When both end members UO_2 and HfO_2 are calculated in the cubic structure, the Gibbs free energies of mixing were negative across the whole temperature range, indicating mixing is energetically favored (Fig. 4.5a). When the Gibbs free energies of mixing are calculated in the cubic and tetragonal structures, two sets of free energies of mixing curves intersect with each other. In order to derive the phase diagram, tangent lines are constructed that connect the two minima of the free energies of mixing curves of the same temperature. Between the two connection points, exsolution is thermodynamically stable, outside the points, the respective thermodynamically stable phases are the end member phases with some admixture of the other element. For medium and low temperature regimes, the tangent lines connect the cubic, UO_2-dominated phase on the left-hand side with the tetragonal (Fig. 4.5b) or monoclinic (Fig. 4.5c) on the right-hand side. In the cubic and monoclinic case, large energy differences was found for both end members (Fig. 4.5c). The zero-point energy – $T \cdot \Delta S_{vib}$ term calculated in cubic structure are showed in Fig. 4.5d. This zero-point energy – $T \cdot \Delta S_{vib}$ term is about 20 % of the free energy of mixing calculated from the enthalpy and the configurational entropy part showed in Fig. 4.5a.

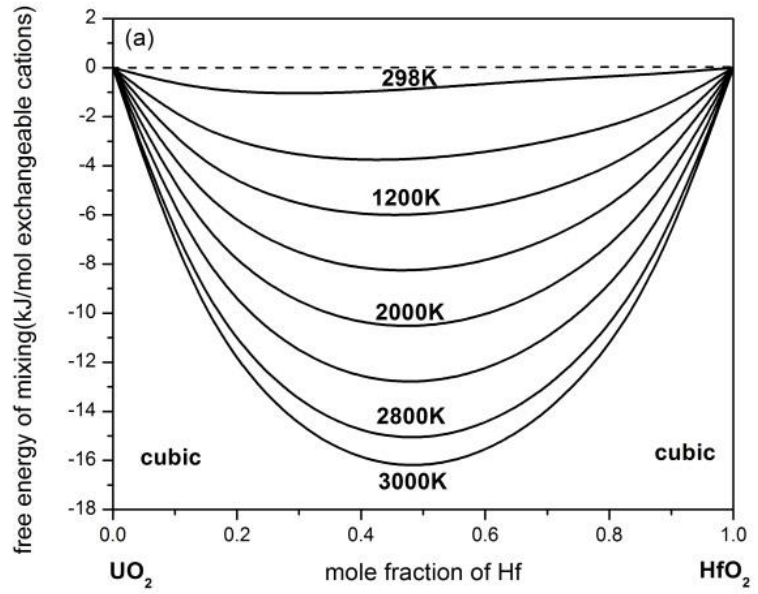
(a)
298K
1200K
2000K
2800K
3000K
cubic
cubic
free energy of mixing(kJ/mol exchangeable cations)
mole fraction of Hf
UO2
HfO2

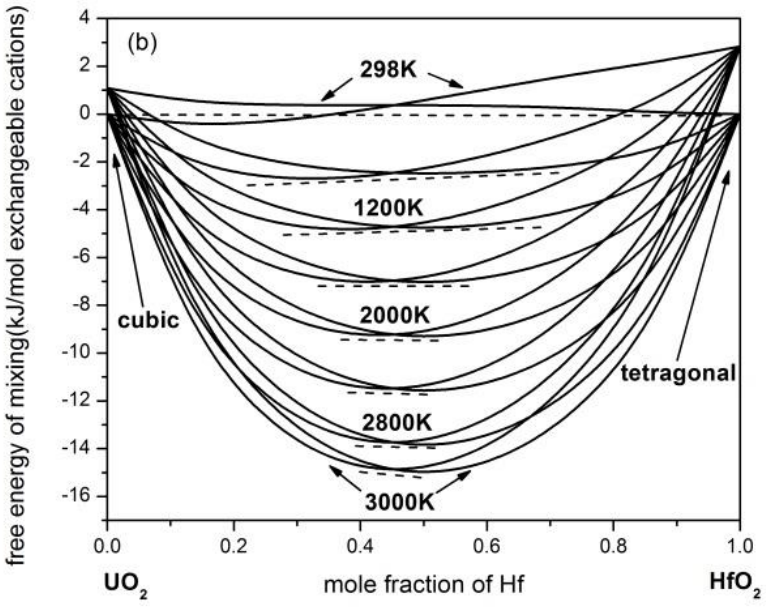
(b)
298K
1200K
2000K
2800K
3000K
cubic
tetragonal
free energy of mixing(kJ/mol exchangeable cations)
mole fraction of Hf
UO2
HfO2

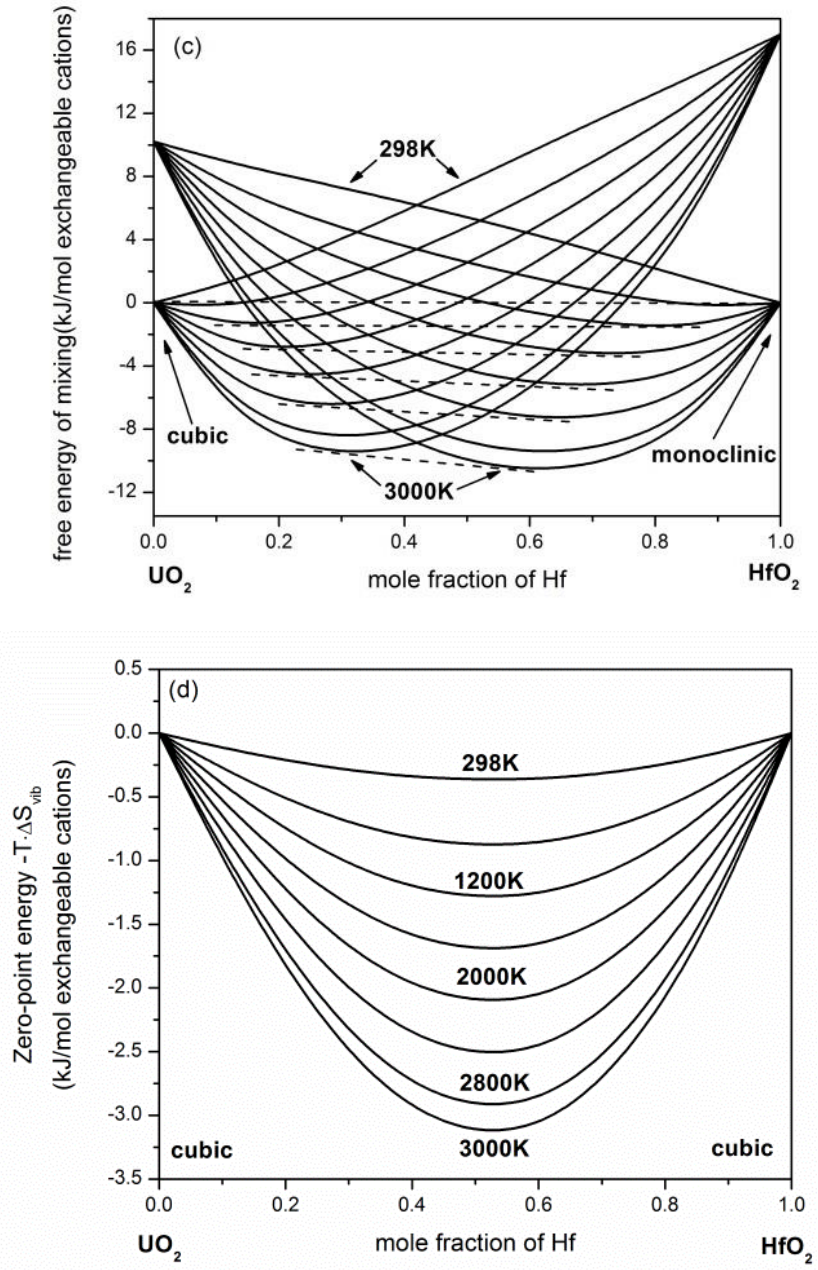

Figure 4.5. Free energy of mixing curves calculated for (a) the cubic system and for combinations of the (b) cubic-tetragonal and (c) cubic-monoclinic structures. Dashed lines are the common tangent line of the free energy of mixing curves of the same temperature for two structures, and only the contributions from the configurational entropies of mixing were considered in the free energies of mixing calculations (the unit for free energy of mixing is in kJ/mol exchangeable cations). The zero-point energy $-\ T{\cdot}\Delta S_{vib}$ terms calculated in cubic structure are showed in (d).

Discussion

Cation exchange parameters and ordering

The cation exchange parameters J_2 of the three structures have larger absolute values than J_1 and J_3 (Table 1), which indicates the second nearest neighbor interaction between U and Hf is the dominant interaction. Previously reported cation exchange parameters for similar cation interactions such as U and Zr are J_1 = 0.484 kJ/mol, J_2 = –0.061 kJ/mol and J_3 = –0.166 kJ/mol in the zircon structure [25]. Positive values of J mean U-Hf avoidance is preferred (Eq. (3)). Thus, U-Hf interactions raise the total energy. As U-Hf interactions are not energetically favored, clustering of similar cations will increase the number of U-U and Hf-Hf interactions [26]. In contrast, when J is negative, U-Hf interaction are favored. However, the structure may form ordered layers of U and Hf cations, which tend to maximize the number of U-Hf interactions, thus leading to a decrease in the total energy. Since first, second and third nearest neighbor cation interactions are included in the fitting, combined effects from three types of interactions are considered. Although some of the J values are negative, entropy of mixing results did not show any tendency to order over a range of temperatures (Fig. 4.4). Clustering of the same cations was visually evident in the cubic structure in the lowest-energy configuration (Fig. 4.6). The nano-clusters in the UO_2-ThO_2 binary in a previous study [25] indicated that nano-exsolution is more energetically favored or kinetically more likely than an exsolved lamellar structure. The latter would require long-distance diffusion, which is an inefficient process in the temperature regime where exsolution is thermodynamically favored [25, 27, 28].

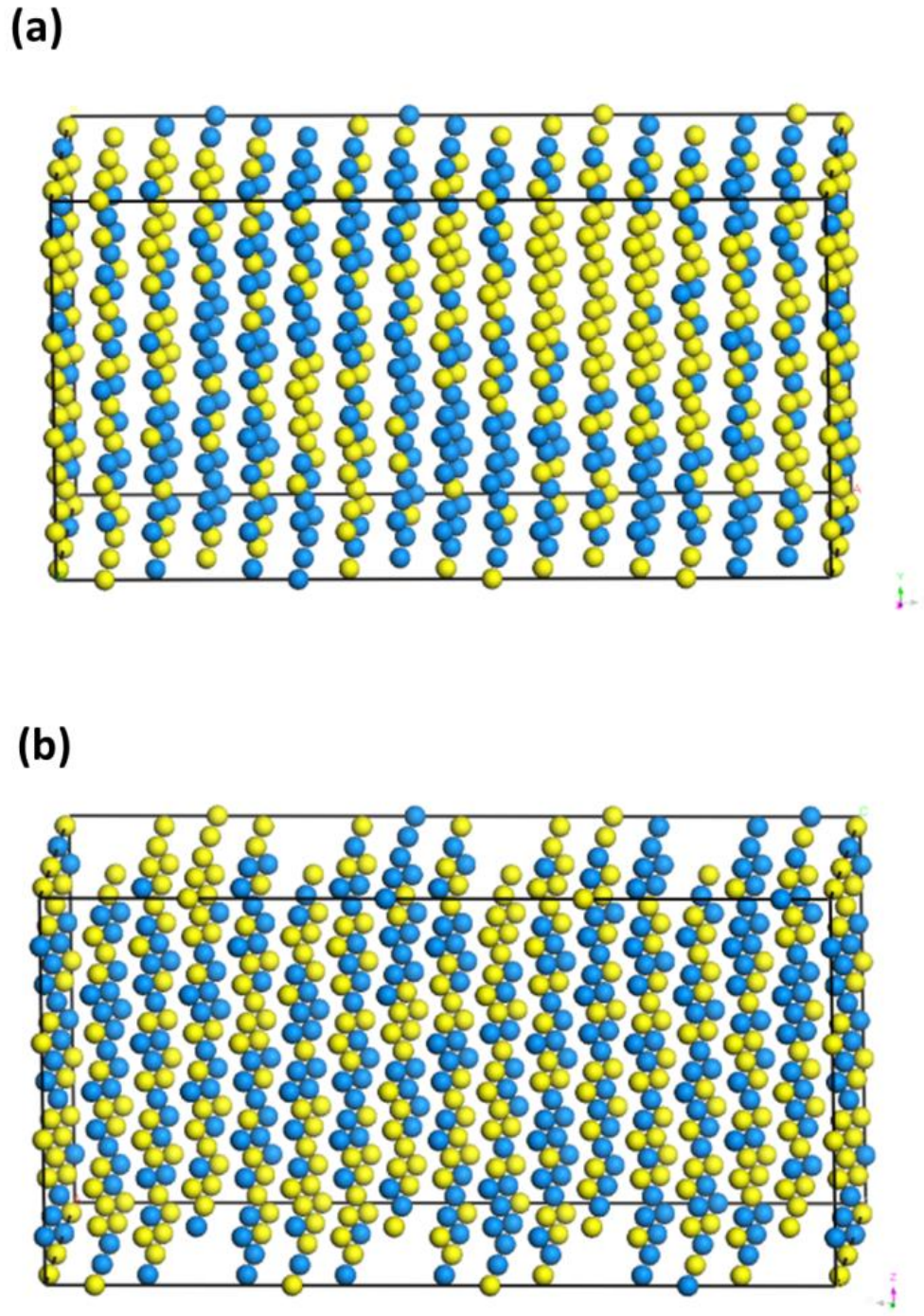

Figure 4.6. Snapshots of cation configurations during Monte Carlo simulations of the UO_2-HfO_2 binary in the cubic structure (Hf cation mole fraction = 0.5) in a 8×4×4 supercell of the most energetically favored configurations at 100 K (a) and 3000 K (b). While the low-temperature configuration (a) shows partial exsolution, the high-temperature conditions in (b) result in random mixing. Only the exchangeable cations U (blue balls) and Hf (yellow balls) but no O atoms are shown in the figure.

Enthalpy and free energy of mixing

The maximum enthalpies of mixing calculated are about 2.0 kJ/(mol exchangeable cations) in the cubic structure (Fig. 4.3). Previously reported maximum values of enthalpies of mixing calculated by a similar method were 2.7 kJ/mol exchangeable cations (UO_2-ThO_2), 10 kJ/mol exchangeable cations ($USiO_4$-$ThSiO_4$), and 30 kJ/mol exchangeable cations ($ZrSiO_4$-$ThSiO_4$) [25, 27]. Small mixing enthalpy values are more likely to lead to small or negative values of the Gibbs free energy of mixing due to the $-T\Delta S$ term (Eq. (8)). For the cubic-tetragonal series, the energy of the cubic UO_2 end member is very close to the supposed tetragonal UO_2, which can be explained by the similarity between their cell parameters (Fig. 4.2a, b). For the other end members of HfO_2, however, large differences in the free energy of mixing are found, which is caused by the large differences in the cell parameters. For the cubic-monoclinic series, as the difference of the structure for the two end members become even larger than the cubic-tetragonal case, energy differences of the two end members is as large as 16 kJ/(mol exchangeable cations). In general, the energy differences of the end members increase as their structures become less similar (e.g., cubic *vs*. monoclinic), which lead to the intersections of the free energy of mixing curves of two different structures.

Phase diagram of UO_2-HfO_2

The free energy of mixing curves (considering only the configurational entropy) can be used to derive the phase diagram of the solid solution. The miscibility gap is the region in the phase diagram where two stable phases will form instead of one. On the free energy of mixing curves, the tangent lines that connect two local ΔG minima for a given temperature can be used to determine, e.g., the maximum amount of Hf that can incorporated into UO_2 at equilibrium. In the cubic structure where there is only one minimum in the ΔG curves for the entire temperature scale above room temperature (Fig. 4a), the UO_2-HfO_2 binary forms a complete solid solution. However, the UO_2-HfO_2 binary has a wide miscibility gap on the phase diagram if solid solutions of two different structure types are considered. In the cubic-tetragonal series, the miscibility gap is centered at an Hf mole fraction of 0.45, and the gap becomes narrower with increasing temperature (Fig. 4.7a). In the cubic-monoclinic series (Fig. 4.7b), the miscibility gap is wider than that of the cubic-tetragonal series. The expected situation is a wider miscibility gap

of cubic-monoclinic phase at low temperature, a narrow miscibility gap of cubic-tetragonal phases at medium temperature and complete mixing of the cubic phase at high temperature. In order to estimate the temperature range for a stable phase in the phase diagram of UO_2-HfO_2 binary, the calculated UO_2-HfO_2 phase diagram was compared with the experimentally determined UO_2-ZrO_2 phase diagram.

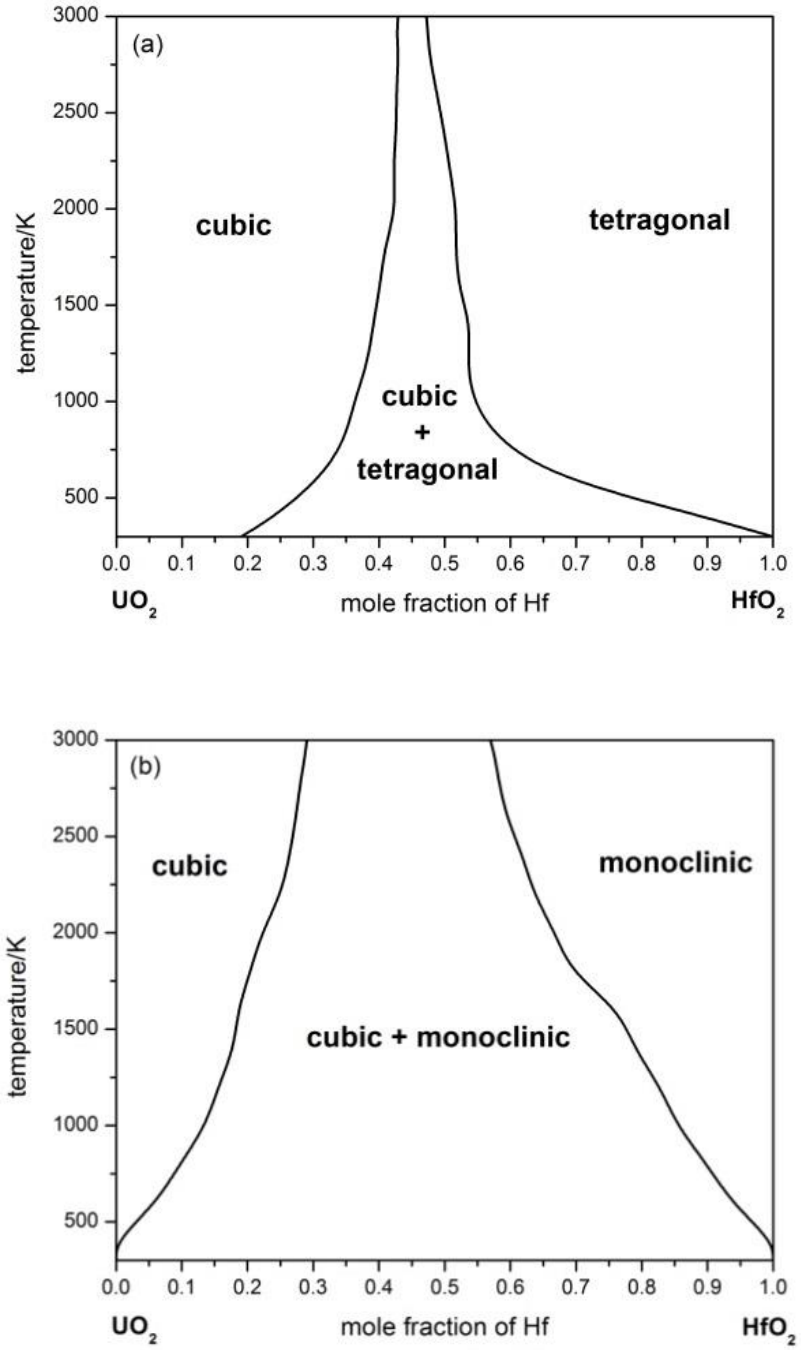

Figure 4.7. Calculated phase diagrams of UO_2-HfO_2 solid solutions with respect to two types of combinations of the end members (cubic-tetragonal (a) and cubic-monoclinic (b)).

Comparison to the UO_2-ZrO_2 binary solid solution

Hafnium and zirconium belong to the same group in the periodic table, and the ionic radii and charges of both cations are nearly the same leading to similar chemical behavior [22, 29]. This can be verified by the occurrence of hafnium in nature where the major source of hafnium is zircon ($ZrSiO_4$), in which hafnium occupies the same site as zirconium [30]. High-hafnium zircon with a Hf/Zr ratio of about 0.6 has been found in zircon [31]. The oxides of hafnium and zirconium, hafnia and zirconia are considered similar oxides due to their similar structure, thus they are expected to form an ideal solid solution [32]. The UO_2-ZrO_2 binary forms complete solid solution but the details of the phase diagram vary considerably [33]. Within the complete solid solution of UO_2-ZrO_2, there are several areas where different phases are present. The dominant miscibility gap contains cubic and tetragonal phases, and the mixed phase area varies from Zr mole fraction of 0.4~0.8 to as wide as 0.1~0.9 at temperature below 2273 K [34-38]. On the ZrO_2 side, a small miscibility gap containing monoclinic and tetragonal phases is reported. Yashima et al., [33] compared the calculated and experimental phase diagrams of UO_2-ZrO_2 binary and obtained the optimized equilibrium phase boundaries, which shows the coexistence of both monoclinic and cubic phases at temperatures below 1400K across the whole composition, an immiscible region of tetragonal and cubic phases between 1400~2000K and a complete solid solution of cubic phase with a small miscibility gap close to ZrO_2 side at temperature above 2000K. The ionic radius of U^{4+}, Zr^{4+} and Hf^{4+} are 0.97 Å, 0.79 Å, and 0.78 Å, respectively [35]. The substitution of smaller cations for larger cations is generally favored. Therefore, the substitution of Hf for U will be energetically favored over Zr substituting for U due to Hf's smaller ionic radius, which could explain the smaller miscibility gap in UO_2-HfO_2 system. Moreover, the formation of solid solution decreases the phase transformation temperatures from monoclinic to tetragonal and from tetragonal to cubic. Based on the comparison with UO_2-ZrO_2 solid solution, the estimated phase diagrams of UO_2-HfO_2 binary are obtained (Fig. 4.8).

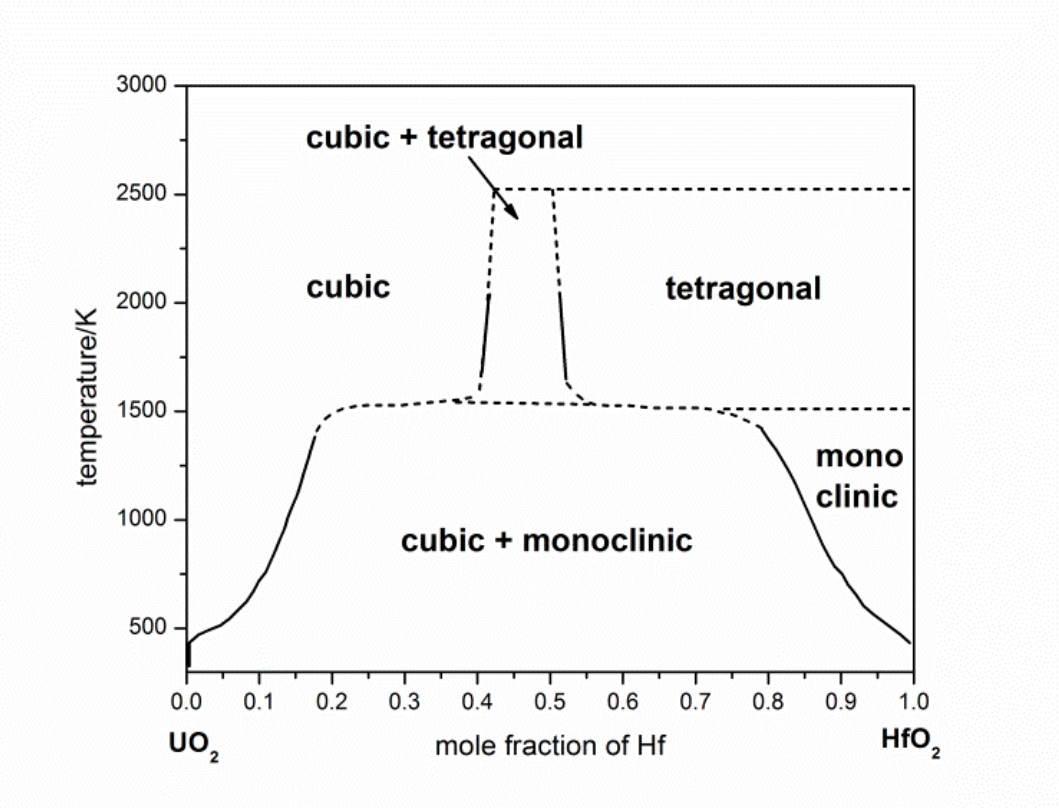

Figure 4.8. Phase diagram of UO_2-HfO_2 solid solution with consideration of phase transition. The dash lines indicate the estimated phase boundary through comparison with the phase diagram of the UO_2-ZrO_2 binary solid solution.

Solid solutions close to the HfO_2 side undergo three stages of phase transitions. At temperatures below 1400 K, the wide miscibility gap region of UO_2-HfO_2 binary with cubic and monoclinic structures was found (Fig. 4.8), which is narrower than the situation of the UO_2-ZrO_2 binary. When the temperature is above 1500 K, a small miscibility gap between Hf mole fractions of 0.40~0.52 exist, followed by the complete solid solution with the cubic structure at temperature above 2600 K. In this strongly non-ideal UO_2-HfO_2 binary solid solution, the phase transition regions between monoclinic to cubic and tetragonal to cubic are obscured by the miscibility gap. The reported phase diagram of the UO_2-ZrO_2 binary has a wider miscibility gap, reflecting the more covalent bonding of <Zr-O> as compared with that of <Hf-O>.

Conclusions

The thermodynamic mixing properties, including enthalpy, free energy, and entropy of mixing were calculated in the UO_2-HfO_2 binary within cubic, tetragonal, and monoclinic structures, respectively. The estimated phase diagrams of the UO_2-HfO_2 binary with consideration of phase transition were obtained by comparison with the phase diagram of the UO_2-ZrO_2. The calculated phase diagram of the UO_2-HfO_2 binary indicates complete solid solution with the cubic structure at high temperature. Close to the compositional range of the UO_2 end member, uranium-rich solid solutions exsolve as the temperature moves the system into the region of the miscibility gap. The calculated phase diagram suggests a tendency to form the monoclinic hafnium-rich phase in a matrix of the isometric, uranium-rich solid-solution. This may occur in Hf-doped nuclear fuels as they cool. The cubic to monoclinic phase transition in the UO_2-HfO_2 binary results in a 7 to 10% increase in the cell volume. The smaller miscibility gap of the UO_2-HfO_2 binary, as compared with that of the UO_2-ZrO_2 solid solution, reflects the fact that the <Hf-O> is less covalent than the <Zr-O> bond.

Acknowledgements

This work is supported by the U.S. Office of Science, Basic Energy Sciences, Grant #DE-FG02-06ER15783.

References

[1] M.L. Grossbeck, J.P.A. Renier, T. Bigelow, Development of improved burnable poisons for commercial nuclear power reactors, NERI final report No. 99-0074, University of Tennessee, Knoxville, 2003. pp. 4-11, 69-72.

[2] C. Collette, G. Francillon, G. Obadia, A. Darraud, Operating experience of the Fragema Gadolinia Bearing Fuel Assembly, In: IAEA (Ed.), Improvements in water reactor fuel technology and utilization, IAEA, Vienna, 1987, pp. 255.

[3] R. Nijsing, Nucl. Eng. Des. 4 (1966) 11-17.

[4] X.H. Luo, W. Zhou, S.V. Ushakov, A. Navrotsky, A.A. Demkov, Phys. Rev. B 80 (2009).

[5] R. Terki, G. Bertrand, H. Aourag, C. Coddet, Mater. Lett. 62 (2008) 1484-1486.

[6] R. Ruh, H.J. Garrett, R.F. Domagala, N.M. Tallan, J. Am. Ceram. Soc. 51 (1968) 23-27.

[7] R. Ruh, P.W. Corfield, J. Am. Ceram. Soc. 53 (1970) 127-129.

[8] G.M. Wolten, J. Am. Ceram. Soc. 46 (1963) 418-422.

[9] M.F. Trubelja, Ionic conductivity in the hafnia-rare earth systems and phase equilibria in the system Hafnia-Zirconia-Yttria, PhD thesis, Materials science and engineering, Pennsylvania state university, 1987.

[10] G.S. Cerefice, Environmental behavior of hafnium: The impact on the disposition of weapons-grade plutonium, PhD thesis, Nuclear Engineering, Massachusetts Institute of Technology, Massachusetts, 2001.

[11] S.J. Clark, M.D. Segall, C.J. Pickard, P.J. Hasnip, M.J. Probert, K. Refson, M.C. Payne, Z Kristallogr 220 (2005) 567-570.

[12] V.L. Vinograd, M.H.F. Sluiter, B. Winkler, A. Putnis, U. Halenius, J.D. Gale, U. Becker, Mineral. Mag. 68 (2004) 101-121.

[13] U. Becker, A. Fernandez-Gonzalez, M. Prieto, R. Harrison, A. Putnis, Phys. Chem. Miner. 27 (2000) 291-300.

[14] U. Becker, K. Pollok, Phys. Chem. Miner. 29 (2002) 52-64.

[15] A. Bosenick, M.T. Dove, E.R. Myers, E.J. Palin, C.I. Sainz-Diaz, B.S. Guiton, M.C. Warren, M.S. Craig, S.A.T. Redfern, Mineral. Mag. 65 (2001) 193-219.

[16] M.T. Dove, Computer simulations of solid solutions, in: A.G. Charles (Ed.), Solid solutions in silicate and oxide systems, Eotvos University Press, Budapest, 2001, pp. 225-249.

[17] M.C. Warren, M.T. Dove, E.R. Myers, A. Bosenick, E.J. Palin, C.I. Sainz Diaz, B.S. Guiton, S.A.T. Redfern, Mineral. Mag. 65 (2001) 221-248.

[18] J.D. Gale, A.L. Rohl, Mol. Simul. 29 (2003) 291-341.

[19] G. Broglia, G. Ori, L. Larcher, M. Montorsi, Modell. Simul. Mater. Sci. Eng. 22 (2014).1-14.

[20] J.W. Anthony, R.A. Bideaux, K.W. Bladh, M.C. Nichols, Uraninite, in: Handbook of mineralogy, Mineralogical Society of America, Chantilly, VA, 2001.

[21] J. Janeczek, R.C. Ewing, J. Nucl. Mater. 190 (1992) 128-132.

[22] J. Adam, M.D. Rogers, Acta Crystallogr. 12 (1959) 951-951.

[23] C.E. Curtis, L.M. Doney, J.R. Johnson, J. Am. Ceram. Soc. 37 (1954) 458-465.

[24] R.W.G. Wyckoff, Crystal structures 1, second ed., Interscience Publishers, New York, 1963.

[25] E.D.A. Ferriss, R.C. Ewing, U. Becker, Am. Mineral. 95 (2010) 229-241.

[26] M. Reich, U. Becker, Chem. Geol. 225 (2006) 278-290.

[27] L.C. Shuller, R.C. Ewing, U. Becker, J. Nucl. Mater. 412 (2011) 13-21.

[28] L.C. Shuller, R.C. Ewing, U. Becker, J. Solid State Chem. 197 (2013) 550-559.

[29] W.J. Zheng, K.H. Bowen, J. Li, I. Dabkowska, M. Gutowski, J. Phys. Chem. A 109 (2005) 11521-11525.

[30] N. Korte, M. Kollenbach, S. Donivan, Anal. Chim. Acta 146 (1983) 267-270.

[31] A.A. Levinson, R.A. Borup, Am. Mineral. 45 (1960) 562-565.

[32] C. Wang, M. Zinkevich, F. Aldinger, J. Am. Ceram. Soc. 89 (2006) 3751-3758.

[33] M. Yashima, T. Koura, Y. Du, M. Yoshimura, J. Am. Ceram. Soc. 79 (1996) 521-524.
[34] G.M. Wolten, J. Am. Chem. Soc. 80 (1958) 4772-4775.
[35] W.A. Lambertson, M.H. Mueller, J. Am. Ceram. Soc. 36 (1953) 365-368.
[36] G.M. Wolten, J. Am. Ceram. Soc. 44 (1961) 148-148.
[37] P.E. Evans, J. Am. Ceram. Soc. 44 (1961) 631-631.
[38] I. Cohen, B.E. Schaner, J. Nucl. Mater. 9 (1963) 18-52.

Appendix C

Supporting Information

Table S 4.1 Morse potential parameters used for the O-O, Hf-O and U-O.

bond	D/eV	a ($Å^{-2}$)	r_0 (Å)	Cij (eV·Å)
$O^{-0.95}$–$O^{-0.95}$	0.062739	1.25	3.60	12
$Hf^{1.89}$–$O^{-0.95}$	0.318922	2.58	2.31	10
$U^{1.89}$–$O^{-0.95}$	0.046303	3.45	2.59	10

Table S 4.2 Experimental and calculated lattice constants (a in Å) and elastic constants (C_{ij} in GPa) of cubic HfO_2 and UO_2. Elastic constants of cubic HfO_2 are from reference [1], and for cubic UO_2 are from reference [2].

parameters		measured	calculated
cubic HfO_2	a	5.115	5.070
	C11	477	522
	C12	113	114
	C44	100	98
cubic UO_2	a	5.468	5.435
	C11	389.3	375.8

[1] S.L. Dole, O. Hunter, C.J. Wooge, J. Am. Ceram. Soc. 60 (1977) 488-490.

[2] I.J. Fritz, J. Appl. Phys. 47 (1976) 4353-4358.

Chapter 5 Conclusions

Reaction pathways and kinetics of the redox transitions of contaminant species are of significant importance in understanding their mobility in a natural environment. The application of electrochemical techniques with complementary spectroscopic techniques provides a promising approach for characterizing short-lived reaction intermediates. Electrochemical techniques allow sweeping the Eh ranging from -0.8 V to 1.2 V (*vs*. NHE, upper and lower limit of water) for time periods from a few minutes to less than a few seconds. The short experimental time is the key advantage that permits the detection and study of the metastable species. In addition, electrochemical AFM, a technique which is commonly used for the investigations of electrode materials in batteries, is applied here to solve an environmental question related to uranium.

The one-electron reduction from U(VI) to U(V) is identified on the surfaces of both powdered and bulk-crystalline magnetite. The results favor the one-electron reduction mechanism followed by the U(V) disproportionation, instead of the two-electron pathway from U(VI) to U(IV). Distinct characteristics between the surfaces of powdered and bulk-crystalline magnetite are found. The surface of the powered magnetite facilitates the disproportionation of U(V), whereas the bulk surface stabilizes the U(V) by precipitation of a mixed-valence state U(V)/U(VI) phase.

The experiments reported here were done in acidic pH conditions (3.2 ~ 5.2), which is mainly to prevent the precipitation of solid uranium phases at high concentration (0.5 ~ 1 mM). It is of

critical importance to increase the pH to near-neutral conditions in future studies, such that the experimental conditions are close to those found in a natural system. Carbonate ions will need to be introduced into the solution in order to increase the mobility of the uranium. However, complexation of CO_3^{2-} with UO_2^{2+} will increase the difficulties in reducing uranyl(VI) species. The kinetics of U(VI) reduction and U(V) disproportionation are also likely to be very different from that found in the present study.

Computational modelling can provide complementary information on the mixing properties of a binary solid solution, especially when the experiments are difficult to be carried out. For example, Hf and Zr have similar chemical properties and it is difficult to separate Zr from Hf in order to obtain a pure HfO_2 end member. The enthalpy, free energy, and entropy of mixing were calculated in the UO_2-HfO_2 binary within cubic, tetragonal, and monoclinic structures, respectively. The calculated phase diagram of the UO_2-HfO_2 binary indicates complete solid solution with the cubic structure at high temperature. Close to the compositional range of the UO_2 end member, uranium-rich solid solutions exsolve as the temperature moves the system into the region of the miscibility gap. There is a tendency to form the monoclinic hafnium-rich phase in a matrix of the isometric, uranium-rich solid-solution, which may occur in Hf-doped nuclear fuels as they cool. In addition, the cubic to monoclinic phase transition in the UO_2-HfO_2 binary results in a 7 to 10% increase in the cell volume. The smaller miscibility gap of the UO_2-HfO_2 binary, as compared with that of the UO_2-ZrO_2 solid solution, reflects the fact that the <Hf-O> is less covalent than the <Zr-O> bond.